

IN-SITU STUDY OF CRACK PROPAGATION IN
PATTERNED STRUCTURES OF MICROCHIPS USING
X-RAY MICROSCOPY

Von der Fakultät 1 – MINT- Mathematik, Informatik, Physik,
Elektro- und Informationstechnik
der Brandenburgischen Technischen Universität Cottbus–Senftenberg
genehmigte Dissertation
zur Erlangung des akademischen Grades eines
Dr. rer. nat.

vorgelegt von

M.Sc. Kristina Kutukova
geboren am 24.09.1991 in Kökschetau, Kasachstan

Vorsitzender: Prof. Götz Seibold

Gutachter: Prof. Dr. rer. nat. habil. Ehrenfried Zschech

Gutachter: Prof. Dr. rer. nat. habil. Dieter Schmeißer

Gutachter: Prof. Dr. rer. nat. habil. Gerd Schneider

Tag der mündlichen Prüfung: 10.02.2023

Kurzfassung

Die Motivation dieser Arbeit bestand darin, Risse in Bereiche von 3D-Nanostrukturen mit hoher Bruchzähigkeit zu lenken und die lokale kritische Energiefreisetzungsrate für die Rissausbreitung in 3D-Nanostrukturen zu bestimmen. On-chip Kupfer-Leitbahnstrukturen, die durch Organosilikatgläser isoliert sind, wurden als Beispielsystem für die Untersuchung des Bruchverhaltens in kleinen Bereichen ausgewählt, da dies ein gut definiertes 3D-nanostrukturiertes System ist und weil für Mikrochips eine hohe mechanische Robustheit gefordert wird. Ein Experiment für die hochauflösende in-situ 3D-Abbildung von 3D-Nanostrukturen und der Kinetik der Mikrorissausbreitung in Festkörpern wurde entwickelt und angewendet, wobei ein miniaturisierter mikromechanischer Test und hochauflösende Röntgenabbildung kombiniert wurden. Speziell wurde ein miniaturisierter Doppel-Cantilever-Beam-Testaufbau (Mikro-DCB) in ein Labor-Röntgenmikroskop integriert, und Nano-Röntgen-Computertomographie wurde zur hochauflösenden 3D-Abbildung der Mikrorissentwicklung im on-chip Leitbahnsystem von Mikrochips, die im 14 nm-Technologieknoten hergestellt wurden, angewendet. Die für mehrere Belastungsschritte während des Mikro-DCB-Tests gemessene Mikrorissgeometrie und die anschließende Datenanalyse auf Basis der linear-elastischen Bruchmechanik und des Euler-Bernoulli-Balkenmodells waren die Grundlage für die Entwicklung und Anwendung einer neuen Methodik zur quantitativen Ermittlung der kritischen Energiefreisetzungsrate für Rissausbreitung in sub-100-nm-Regionen eines prozessierten Wafers. Experimentell wurde nachgewiesen, dass sogenannte „guard ring“-Strukturen an der Peripherie der Mikrochips Energie so dissipieren, dass die Mikrorissausbreitung wirksam verlangsamt und schließlich gestoppt wird, d.h. sie verhindern eine mechanische Schädigung der Mikrochips. Es wurde gezeigt, dass es möglich ist, den Mikroriss durch Überlagerung der Bruchmoden an der Risspitze kontrolliert zu steuern. Das aufgestellte Konzept zur kontrollierten Rissausbreitung bildet die Basis für weitere grundlegende Studien zum Bruchverhalten nanoskaliger Materialien und Strukturen. Die Ergebnisse tragen zum besseren Verständnis der Bruchmechanik in kleinen Skalen bei, z. B. in Mikrochips, aber auch in anderen nanostrukturierten Materialien, z. B. in bioinspirierten, hierarchisch strukturierten technischen Werkstoffen. Die experimentellen Ergebnisse, die an mikroelektronischen Produkten erhalten wurden, liefern wertvolle Informationen zur Kontrolle der Rissausbreitung in on-chip Leitbahnsystemen zur Herstellung mechanisch robuster Mikrochips in fortgeschrittenen Technologieknoten. Die Experimente zur kontrollierten

Ausbreitung von Mikrorissen in Bereiche mit hoher Bruchzähigkeit liefern Informationen für das Design von „guard ring“-Strukturen in Mikrochips, um die Ausbreitung von Mikrorissen, die z. B. während des Vereinzelns des Wafers erzeugt wurden, zu stoppen.

Abstract

The motivation of this thesis was to control crack steering into regions of engineered 3D-nanopatterned structures with high fracture toughness and to determine the local critical energy release rate for crack propagation in 3D-nanopatterned systems. On-chip copper interconnect structures of advanced microchips, insulated by organosilicate glasses, were chosen as an example system to study fracture on small scale, since this is a well-defined 3D-nanopatterned system and since a high mechanical robustness is requested for microchips. An experiment for in-situ high-resolution 3D imaging of the fracture behavior of 3D-nanopatterned structures and of the kinetics of microcrack propagation in solids was designed and applied, combining a miniaturized micromechanical test and high-resolution X-ray imaging. Particularly, a miniaturized piezo-driven double cantilever beam test set-up (micro-DCB) was integrated in a laboratory X-ray microscope, and nano X-ray computed tomography was applied for high-resolution 3D imaging of the microcrack evolution in the on-chip interconnect stack of microchips manufactured in the 14 nm technology node. The measured geometry of the microcrack at several loading steps during the micro-DCB test and the subsequent data analysis based on linear elastic fracture mechanics and the Euler-Bernoulli beam model were the basis for the development and application of a new methodology to determine the critical energy release rate for crack propagation in sub-100 nm regions of a processed wafer quantitatively. It was experimentally proven that specially designed metallic guard ring structures at the rim of the microchips dissipate energy in such a way that the microcrack propagation is efficiently slowed down and eventually stopped, i.e. they are effective to prevent mechanical damage of microchips. It was demonstrated that it is possible to steer the microcrack in a controlled way by tuning the fracture mode mixity locally at the crack tip. The established concept for a controlled crack propagation provides the basis for further fundamental studies of the fracture behavior of nanoscale materials and structures. The results have significant effects for the understanding of fracture mechanics at small scales, e.g. in microchips, but also in other nanopatterned materials, e.g. in bio-inspired, hierarchically structured engineered materials. The experimental results gathered at realistic microelectronic products provide valuable information to control the crack path in on-chip interconnect stacks for design-for-reliability in semiconductor industry and to manufacture mechanically robust microchips in leading-edge technology nodes. The experimental study of controlled microcrack steering into regions with high fracture toughness provides knowledge for the design of guard ring

structures in microchips to stop the propagation of microcracks, e.g. generated during the wafer dicing process.

Table of Contents

KURZFASSUNG	I
ABSTRACT	III
TABLE OF CONTENTS	V
LIST OF FIGURES	VII
LIST OF TABLES	XI
ACRONYMS AND SYMBOLS	XII
1 INTRODUCTION	1
2 STATE OF THE ART: EXPERIMENTAL STUDIES OF THE MECHANICAL ROBUSTNESS OF MICROCHIPS	4
2.1 Reliability concerns of microelectronic products manufactured in advanced technology nodes	4
2.2 Experimental studies of crack propagation in BEoL stacks	8
2.2.1 <i>Post mortem</i> (2D) studies	8
2.2.2 <i>In-situ</i> kinetic (3D) studies	11
2.3 State of the art study of mechanical properties and 3D imaging of BEoL stacks	13
2.3.1 Conventional DCB test	13
2.3.2 Micromechanical test set-up in X-ray microscope	14
3 ADVANCED MICRO-DCB TEST IN X-RAY MICROSCOPE	17
3.1 Laboratory based X-ray microscopy	17
3.2 Micro-DCB test set-up	18
3.2.1 Experimental setup and operation	18
3.2.2 Determination of energy release rate using micro-DCB test	19
3.3 Micro-DCB test with force sensor - Micro-DCB 2.0	25
3.3.1 Performance of the micro-DCB 2.0 test system and its integration into the TXM	27
3.3.2 Quantification of the energy release rate using force measurement	27
3.4 Experimental validation of G_c determination on reference structures at micro-DCB tests	29
4 CRACK PROPAGATION IMAGING IN PATTERNED STRUCTURES OF MICROCHIPS	34
4.1 Micro-DCB sample description	34
4.2 Static loading – driving the crack to tough regions	38
4.2.1 <i>In-situ</i> radiography	38
4.2.2 Tomography	40
4.2.3 3D data analysis	42
4.3 High resolution imaging at nano-XCT	44

5	COMPLIMENTARY STUDY- <i>IN-SITU</i> SYNCHROTRON SOFT X-RAY MICROSCOPY OF THE BEOL STRUCTURE	47
5.1	Micromechanical test at a synchrotron radiation based TXM	47
5.2	High-resolution <i>in-situ</i> soft X-ray microscopy	49
5.3	Nano X-ray tomography	51
6	DISCUSSION OF THE EXPERIMENTAL RESULTS	54
6.1	Determination of local G_c of BEoL stacks	54
6.2	Controlled crack path steering in BEoL stacks	62
7	SUMMARY AND OUTLOOK	67
7.1	Summary	67
7.2	Outlook	69
	REFERENCES	72
	APPENDIX	80
A.	Data analysis and calibration procedures	80
	A1 Image analysis to determine parameter A	80
	A2 Micro-DCB 2.0 calibration	82
	A3 Error estimation of analytical approaches for G_c	85
B.	Tester drawings and interface	89
	B1 Drawings micro-DCB 2.0	89
	B2 Graphical user interface of micro-DCB 2.0	91
C.	Source code	93
	LIST OF PUBLICATIONS	95
	ACKNOWLEDGMENT	99

List of Figures

Figure 1.1: Sample thickness / resolution for transmission X-ray microscopy, visual light microscopy and transmission electron microscopy [Kut+22a].	1
Figure 2.1: Evolution of interlayer dielectric materials [Fan16, Vol+10, Dil2021, Tra2021].	5
Figure 2.2: Mechanical properties of silicon based materials with varying dielectric constant [Xu+02].	5
Figure 2.3: Scheme of decreasing of resistance to dicing flaws with evolution of technology node [Lan+07].	7
Figure 2.4: Schematics of the indentation procedure and SEM image with marked crack length along the etch stop (ES) layer to patterned Cu interfaces at the middle and lower metallization levels. Here the crack propagates across two different interfaces: ES to Cu and ES to ILD [Mol+07].	8
Figure 2.5: Correlation between the energy of adhesion for the interface ES/Cu measured by four-point bending and the crack length along the same interface measured by MCSN for the case of ILD-2 (ES/ILD-2 adhesion energy is about 3 J/m ² in all cases). Error bars represent the standard deviation for the mean value for 5–7 indentations. Typical standard deviation for four-point bending is 10% [Mol+07].	9
Figure 2.6: Load displacement trace from four-point bend (4PB) testing of crack stops in an eight level BEoL structure with 4PB test configuration for testing crack stop structures [Sha+07].	10
Figure 2.7: Overview of the current X-ray imaging set-ups at different energies and resolution.	12
Figure 2.8: Illustration of a partially delaminated standard DCB geometry with freely rotatable beam ends at the force introduction points: F – applied force, h_1 and h_2 – beam heights, $u_{yn}(L)$ – cantilever deflections at the end of the beam in y $n=\{1,2\}$, $Y = u_{y1}(L) + u_{y2}L$ - maximum beam opening, x – coordinate in interface/crack plane direction with origin in the crack tip, y – coordinate perpendicular to the interface/crack plane, L – crack length.	14
Figure 3.1: Scheme of the micro-DCB test inside X-ray microscope.	18
Figure 3.2: (a) Scheme of the micro-DCB test, (b) micro-DCB test setup inside the X-ray microscope: Z axis: X-ray beam direction, Y axis: rotation axis of the sample (sample fixed on sample holder as in (a)), X axis: direction of applied load [Nie15].	18
Figure 3.3: Stitched radiograph of a micro-DCB sample. The stitching array of 3y x 12x radiographs is compressed along the x coordinate for better visualization of the geometric sizes.	20
Figure 3.4: Sketch of the different differential steps of the bending beam solution highlighting the boundary conditions.	21
Figure 3.5: Scheme for two extreme cases, fixed cantilever ends and free cantilever ends.	22
Figure 3.6: Micro-DCB 2.0 test setup inside the X-ray microscope. Z axis: X-ray beam direction, Y axis: rotation axis of the sample X axis: direction of applied load.	26
Figure 3.7: (a) Scanning electron microscopy (SEM) image of the reference structure: assumed a one ILD layer (H3) and two etch stop layers (H2, H4); micro-DCB test at nano-XCT: (b) Radiographs in standard resolution mode, stitched radiographs, (c): Radiograph at high resolution mode.	29
Figure 3.8: Force-crack length diagrams are based on 5 micro-DCB 2.0 experiments on reference samples and the ideal curve in black based on analytical solution (Eq. 3.29) with $G = 4.0 \text{ J/m}^2$, $e = 1$ ($h_1 = h_2$), sample width $b = 50 \text{ }\mu\text{m}$, initial crack length $L = 100 \text{ }\mu\text{m}$, displacement $Y = 0.1 \text{ }\mu\text{m}$.	31

Figure 3.9: Plot of calculated G values over the crack length based on 5 micro-DCB 2.0 experiments on reference samples. The data in circles is described by the correlation of the images with a specific uncertain event in the micro-DCB experiment..... 32

Figure 3.10: Scheme of the reference sample design: a) crack propagates between Si and/or ILD layers; b) crack splits at different interfaces and a crack at silicon beam. (crack propagation from the left to the right)..... 32

Figure 3.11: Plot of calculated G values over the crack length based on 5 micro-DCB 2.0 experiments on reference samples. The linear fit does not include outliers of certain events. The radiograph on the bottom and crack length L (x-axis) are calibrated to visualize the crack length..... 33

Figure 4.1: Scheme of the part of wafer with 4 dices, showing the dicing area, and SEM cross-section images with crack stop structures of leading-edge microprocessor with 12 layers of Cu interconnects manufactured in 14 nm CMOS technology node..... 34

Figure 4.2: TEM image of a part of a GR structure with 12 metallization and a post passivation layer, consisting of two sub-layers with different composition of the dielectrics. Scale bar is 1 micron. Image rotated by 90° in respect to Figure 4.1..... 35

Figure 4.3: Scheme of the sample preparation procedure: (a) Top view of a centered dummy with a scribe line and two guard rings of patterned wafer ;(b) Side view of achieved after curing a sandwich structure and its top view after first step of grinding process with the sawing lines in size of 1mm length, 50 μm width and ca. 80 μm depth; (c) single sample after final step of grinding and acetone bath. 36

Figure 4.4: Sample and test design (a) sample geometry, (b) pre-crack description. 37

Figure 4.5: Photograph of the initial cracking procedure at the PAM: a) Image of PAM set-up with aligned razor blade to fixed sample in the tweezers ; b) the beam is aligned with the razor blade (black dot) at the 50X objective magnification; c) crack initiation at the BEoL stack..... 37

Figure 4.6: Photographs of the sample mounting to the micro-DCB tester at the PAM: a) sample alignment to brackets of the tester, brackets are open, b) fixed sample with the glue, brackets are closed. 38

Figure 4.7: (a) SEM cross-section image of a GR structure with 12 metallization (M1 - M12) layers and a passivation layer on top, and two schemes for potential crack paths (red lines). The microcrack propagates from right to left. Mn refers to the n-th metallization layer, P to the post passivation layer; (b) Scheme of the micro-DCB test using a sandwich sample with the region of interest (ROI): Copper guard ring (GR) structure in the BEoL stack of a microchip; c) Stitched radiograph (8x, 3y) of the micro-DCB sample inside TXM. 39

Figure 4.8: Radiographs of the micro-DCB sample with acquisition time per each of 15 seconds (Dummy, Chip, GR2 - guard ring 2, SL - scribe line, Adhesive): crack tip towards the GR2 (middle) and after passing the GR2 (bottom). The middle and bottom radiographs taken at the same displacement position. 40

Figure 4.9: XY Virtual cross-sections through the Cu/low-k BEoL stack at several stages of the micro-DCB test, based on nano-XCT data [Kut+17]. The virtual cross-sections are based on four tomography datasets at several states of the crack propagation from the right to the left. Crack openings at the end of the beams and the crack lengths in μm are : a)11.3/410, b)11.8/ 425, c)15.85/432, and d)16.0/442. The values of crack opening are different from the displacement values from the actuator (max. 13.7 μm) because of the initial crack opening of several micrometers. 41

Figure 4.10: (a) and (b) XZ Virtual cross-sections through the Cu/low-k BEoL stack to corresponding loading position in Figure 4.9 (b) and (d), respectively. Two respective XY cross-section at the red lines position in (b), showing multiple cracking at GR2 (c). 42

- Figure 4.11: Representation of the crack path (from right to left) between metallization layers: a) Result of the image analysis script to detect the location of the crack. Shown is the XZ scan with the height (in μm) above the silicon substrate indicated as color b) Virtual plane view (above metallization layer 8, M8) showing the crack propagation in the Cu/low-k BEOI interconnect stack, based on the reconstructed nano-XCT data. c) Post-mortem SEM image of the fracture surface. Upper image: SEM image of a FIB cross-section with a red line indicating the crack position. 43
- Figure 4.12: Example of the data analysis: a) Height map based on the tomography data 16-bit image; b) Zoom in of the GR region 32-bit; c) thresholding of the image (b) for single layer investigation according to height map: Red color indicate M5 (50%) and Red color indicate M4 (30%). 44
- Figure 4.13: Stitched radiograph of the GR structure at HR with FOV of $16\ \mu\text{m}$ (1x,3y) of unloaded sample. 45
- Figure 4.14: Stitched radiographs at SR mode (a) and HR mode (b) at final experiment state. Scale bar $16\ \mu\text{m}$. Beam ratio of dummy to chip $e = 33\mu\text{m}/28\mu\text{m} = 1.2$ 45
- Figure 4.15: Series of radiographs taken at HR of a micro-DCB sample with a beam ratio $e=1.2$: a) crack toward GR2 at SL at M4, b) crack starts to penetrate GR2, c) crack passed GR2 down to M2. Force-time plot for micro-DCB 2.0 experiment indicates the critical force of 15.5 mN at position (a) and drop down to 14.5 mN at position (c). 46
- Figure 5.1: Optical set-up of the full-field transmission X-ray microscope: Monochromatized synchrotron radiation, condenser with central stop, sample with mechanical test setup, Fresnel zone plate, CCD detector. 48
- Figure 5.2: (a) Mechanical manipulator (Picoindenter PI95, Bruker Corporation); (b) Scheme of the indentation of the BEOI stack using a tungsten wedge 48
- Figure 5.3: The modifications in the set-up of PI95 (a) designed and (b) built. The scheme of the indenter and sample position is shown in (c). 49
- Figure 5.4: (a) SEM image (top view) of the wedge indenter; (b) tip curvature with radius of ca. 220 nm. 49
- Figure 5.5: (a) SEM image of a cross-section with crack stop structures of a microchip with 12 layers of Cu interconnects. (b) SEM image of the initial crack ($12\ \mu\text{m}$ length and 225 nm width) prepared by FIB milling that is positioned between metal layer M8 and metal layer M9. Sample thickness in z direction $2.5\ \mu\text{m}$ 50
- Figure 5.6: (a) The tungsten wedge indenter is initiating the crack from in the scribe line (toward the crack stop). (b) The crack is stopped in front of the crack stop structure, then it propagated down at metal 8. (c) The crack propagates between metal M8 and metal M7 and is then directed to metal M4. 50
- Figure 5.7: (a) The tungsten wedge indenter is initiating the crack from in the scribe line (toward the crack stop). (b) The crack propagates between metal 6 and metal 7 and is then directed above metal 9. The mounting of the sample is flipped vertically for the better visualization. The sample thickness in z direction is $2.2\ \mu\text{m}$. Energy range: 1200 eV, exposure time 2s/image. 51
- Figure 5.8: Synchrotron-based nano-XCT reconstructed data of sample (Figure 5.7) after experiment (a) WBP, (b) WBP+SIRT (10 iterations), (c) Hybrid reconstruction algorithm [Top+20]. 52
- Figure 6.1: (a) Crack opening vs. crack length at several loading steps during the micro-DCB test, (b) calculated G values at several loading steps (and respective crack lengths). 56
- Figure 6.2: (a) Virtual cross-section (XY view) with indicated crack path change from M7 to M5; (b) XZ height map of the crack in the on-chip interconnect stack (SL, GR, Cu/low-k BEOI), heights above the Si substrate indicated by colors; (c) Scheme of the cross-section XY at the indicated z location (red line) with crack pathway, showing crack path change from M7 to M5, heights above the Si substrate in μm . The color scale bar

corresponds to the heights from zero (Si substrate) to about 6 μm (post passivation layer P).....	57
Figure 6.3: Sequence of radiographs during micro-DCB test, beam ratio $e = 0.74$ at the Guard Rings 1 and 2 (GR1 - crack from chip side to scribe line, and GR2 – from scribed line to chip.	58
Figure 6.4: Force-crack length curve of the micro-DCB2.0 experiment with critical force for GR1 and GR2 failures.	59
Figure 6.5:(a)Virtual cross-section (XY view) with indicated crack path change from M5 to M4; (b)XZ height map of the crack in the on-chip interconnect stack (SL, GR2, Cu/low-k BEOl), heights above the Si substrate indicated by colors; (c) Scheme of the cross-section XY at the indicated z location (red line) with crack pathway, showing crack path change from M5 to M4, heights above the Si substrate in μm . The colour scale bar corresponds to the heights from zero (Si substrate) to about 6 μm (post passivation layer P).....	59
Figure 6.6: Plot of calculated G over the crack length of the micro-DCB 2.0 experiment on a BEOl sample from Figure 6-4 and Figure 6-5. Beam ratio $e= 0.74$	60
Figure 6.7. Radiographs of two micro-DCB samples with asymmetric geometry: (a) $e = 0.65$ ($h_1 = 25 \mu\text{m}$, $h_2= 38 \mu\text{m}$) and (b) $e = 2.10$ ($h_1 = 40 \mu\text{m}$, $h_2 =19 \mu\text{m}$).....	63
Figure 6.8: Virtual cross-sections (XY views) with indicated crack path changes (a); XZ height maps of the crack in the on-chip interconnect stack (SL, GR, Cu/low-k BEOl), heights above the Si substrate indicated by colors; Schemes of the cross-section XY at the indicated z location (red line) with crack pathways (c), showing crack path changes from M10 to M12 (sample in Figure 6.7 a) and M6 via M3 to M2 (sample in Figure 6.7 b).	64
Figure 6.9: Dominant metal layers of crack propagation for several beam height ratios e , based on 7 samples for $e \approx 0.5$, 9 samples for ≈ 1 , and 12 samples for $e \approx 2$, error bars from statistical data analysis.....	65

List of Tables

Table 2.1: Typical materials in chip package and it Young's modules and CTE [Gal+12, Yoo+06, Liu+17, CL18].....	4
Table 2.2: Comparison of standard DCB and micro-DCB tests.....	15
Table 3.1 Geometrical parameters from micro-DCB experiments on reference structures.	30
Table 3. 2: Geometrical parameters of tested samples for micro-DCB 2.0.....	30
Table 4.1: Thicknesses of metallization layers based on TEM image.	35
Table 4.2: X-ray attenuation length and transmission thickness at 8.05 keV of several materials [Hen93].....	35
Table 5.1: Table of comparison laboratory based and synchrotron-based set-ups.....	47

Acronyms and Symbols

2D: Two-dimensional

3D: Three-dimensional

4PB: four-point bend

BESSY: Berlin Electron Storage Ring Society for Synchrotron Radiation

CCD: charge coupled device

CMOS: complementary metal oxide semiconductor

CPI: chip-package interaction

CSP: chip-scale-package

CTE: coefficient of thermal expansion

CVD: chemical Vapor Deposition

DCB: double cantilever beam

DLA: deep learning algorithms

ES: etch stop

FIB: focused ion beam

FZP: Fresnel zone plate

GUI: Graphical User Interface

HR: high-resolution

IC: integrated circuit

MBT: Modified Beam Theory

MCSN: modified cross-sectional nanoindentation

MELT: Modified Edge Liftoff Test

MEMS: microelectromechanical system

PAM: pre-alignment microscope

RS232: Recommended Standard 232 serial communication

SEM: scanning electron microscopy

SIP: system-in-package

SIRT: simultaneous iterative reconstruction method

SR: standard resolution

TEM: transmission electron microscopy

TXM: transmission X-ray microscopy

U41-TXM: planar undulator X-ray transmission microscope

WBP: weighted back projection

XCT: X-ray computed tomography

Micro-DCB sample

BEoL: back end of line

GR: guard ring

GR1: guard ring from chip to scribe line

GR2: guard ring from scribe line to chip

H_n : height of n -th ILD layer

ILD: interlayer dielectrics

M_n : n -th metal layer number in BEoL

OSG: organo-silicate glass

P: post passivation layer

ROI: region of interest

SL: scribe line

ULK: ultra low-k

Fracture mechanics

G : energy release rate

G_c : critical energy release rate

G_n : energy release rate for single n -beam system, $n = \{1,2\}$

$u_{y_n}(L)$: cantilever deflections at the end of the beam in y , $n = \{1,2\}$

A : geometrical parameter

a : half crack length

b : beam width

C_n : n -th integration coefficients, $n = \{1,2,3,4\}$

e : ratio of the heights of both beams

E : Young's modulus

F : force

F_n : n -th fitted force for n -beam $n = \{1,2\}$

h_n : n -th height of a n beam $n = \{1,2\}$

I : second moment of area

k : relative permittivity

L : length of a crack

M : bending moment

q : distributed load

Q : shear force

t : thickness of a beam

$u(x)$: bending line

u' : bending slope

U_{el} : elastic energy

x : coordinate in interface/crack plane direction with origin in the crack tip

y : coordinate perpendicular to the interface/crack plane

Y : maximum beam opening

γ : specific surface energy

δ : calibration parameter

π : mathematical constant

σ : stress

1 Introduction

Transmission X-ray microscopy (TXM) is an imaging technique that bridges the resolution gap between visible light microscopy and electron microscopy. Today, synchrotron-based soft X-ray microscopes allow a resolution down to 10 nm, and laboratory X-ray microscopes, usually operating in the multi-keV photon energy range up to 8 keV, enable a resolution of about 50 nm. Since photons in the X-ray energy range are able to penetrate deep into the object, X-ray imaging is characterized by a sample thickness / resolution value of $\sim 10^3$ (see Figure 1.1 [Kut+22a]), which is a ratio that allows tomography. That means, nano X-ray computed tomography (nano-XCT) is a unique analytical technique for non-destructive 3D imaging of the interior of objects or materials with high spatial resolution. In contrast to X-ray microscopy, visible light microscopy provides usually 2D images, and electron tomography in the transmission electron microscope (TEM) requires the preparation of small samples with a lamella thickness in the ~ 100 nm range.

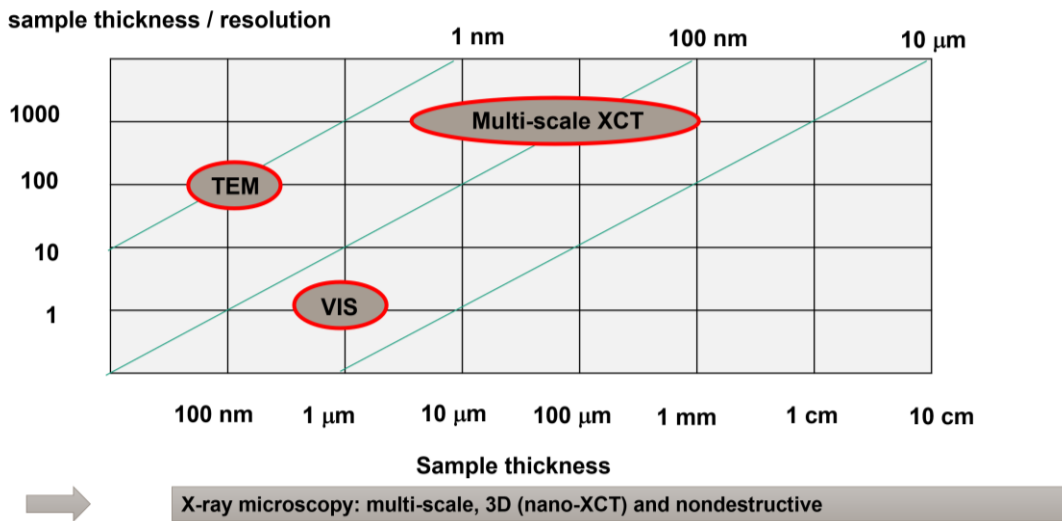


Figure 1.1: Sample thickness / resolution for transmission X-ray microscopy, visual light microscopy and transmission electron microscopy [Kut+22a].

The unique capability of the nano-XCT technique to image the interior of opaque samples non-destructively with sub-100 nm resolution is a necessary condition for the study of kinetic processes in objects and materials. The high-resolution imaging of microstructure or morphology of materials provides valuable information to materials science and engineering, particularly for the design and for the synthesis of new materials. The study of kinetic processes in systems (e.g. microchips, battery electrodes) delivers essential

information for solid-state physics, chemistry and fracture mechanics. Nowadays, 100 years after Griffith's ground-breaking paper describing the fundamentals of fracture mechanics [Gri21], mechanical properties of materials in micro- and nanoscale dimensions have become an important area of fundamental research in solid-state physics and materials science, including the development and introduction of new techniques for micro- and nanomechanical testing [PWK18, Ast+19]. At the same time, there is an increasing need of industry to evaluate the risk of microcrack evolution at small length scales since crack growth can cause catastrophic failure in 3D-nanostructured systems and functional materials such as composites, battery electrodes and integrated circuits (ICs).

Targeting on engineered damage-tolerant 3D-nanopatterned structures, a novel methodology for controlled crack steering into regions with high fracture toughness and for determining the local critical energy release rate G_c for crack propagation in 3D-patterned systems is developed and applied in this thesis. Nanopatterned on-chip copper interconnect structures of advanced microchips, insulated by organosilicate glasses, were chosen as an example system to study fracture effects on small scale, since this a well-defined 3D-nanopatterned system and since a high mechanical robustness is required for microchips. The combination of micromechanical testing and high-resolution X-ray imaging opens the way for the development of design concepts for novel engineered materials systems based on their local mechanical properties.

Mechanical failure caused by microcracks that were introduced into a microchip during the manufacturing process, e.g. during dicing of a semiconductor wafer, are a serious reliability concern for microelectronic products [Kut+22a]. The risk of microcrack growth and eventually fracture in the backend-of-line (BEoL) stack has been increased since the introduction of so-called low-k and ultra-low-k (ULK) materials – with low dielectric permittivity but also low Young's modulus and cohesive strength, and consequently low fracture toughness - to insulate the on-chip metal interconnects. These effects have been further pronounced by new manufacturing technologies (thinned silicon, advanced packaging) and – since these are mainly thermomechanical effects – by the materials used having different coefficients of thermal expansion (CTE). The integration of materials with different CTE values results in mechanical stress caused by thermal processes during the microchip manufacturing – both BEoL manufacturing and (advanced) packaging - and during operation.

Chapter 2 of this thesis is focused on reliability concerns in microelectronic products as well as state-of-the art experimental studies of microcrack evolution, by both *post mortem*

studies in 2D and kinetic studies with 3D data sets. It is concluded that for the understanding of fracture mechanics at small scales, a specially designed experimental setup is needed to steer microcracks into toughened regions of nanopatterned structures by applying a precisely controlled mechanical load and by monitoring force and displacements in materials at the micro- and nanoscale. It is concluded that for the understanding of fracture mechanics at small scales, a specially designed experimental setup is needed to steer microcracks into toughened regions of nanopatterned structures by applying a precisely controlled mechanical load and by monitoring force and displacements in materials at the micro- and nanoscale.

A miniaturized mechanical test for 3D-nanopatterned systems and materials - a micro double cantilever beam (micro-DCB) test in a laboratory X-ray microscope – which provides the capability for high-resolution 3D imaging of microcrack evolution while a force is applied is described in Chapter 3. Laboratory transmission X-ray microscopy (TXM) and nano X-ray computed tomography (nano-XCT) are used to image microcracks and to study the kinetics of microcrack propagation in 3D-nanopatterned integrated circuits with sub-100 nm resolution (Chapter 4) and complemented for thinner samples by synchrotron-radiation studies at lower photon energy with higher resolution (Chapter 5).

The requirement to a mechanically robust 3D-nanopatterned on-chip interconnect stack against wafer processing and packaging stress requires that the fracture driving force for pre-existing defects – e.g. microcracks – is smaller than the fracture resistance of the BEoL stack. As a preventive measure to avoid fracture and mechanical chip damage, metallic guard ring (GR) structures that are mechanically robust against local mechanical stress are designed and integrated at the rim of microchips manufactured in leading-edge CMOS technology nodes. Another option to dissipate energy is to steer the microcrack into regions of the Cu/low-k stack with relatively high fracture toughness, with the consequence that the crack propagation is slowed down and eventually stopped. In chapter 6 of this this thesis, the experimental determination of the local energy release rate G_c in sub-100 nm dimension is explained and the effectiveness of GR structures is demonstrated. In addition, an experimental approach that allows to steer the microcrack in a controlled way by tuning the fracture mode mixity locally at the crack tip and to acquire simultaneously the 3D image information of a region of interest (ROI) that includes the on-chip interconnect stack of an advanced microchip is presented.

2 State of the art: Experimental studies of the mechanical robustness of microchips

2.1 Reliability concerns of microelectronic products manufactured in advanced technology nodes

The continuous scaling down of devices in semiconductor industry challenges design and materials integration of on-chip interconnect stacks. The Cu/low-k technology for Backend-of-Line (BEoL) stacks of integrated circuits has been introduced into high volume manufacturing to improve the performance of microelectronic products manufactured in advanced CMOS technology nodes [Ing+08, Ing+12]. However, the reduced mechanical and chemical robustness of the insulating thin film materials that are characterized by a low dielectric permittivity k is a serious trade-off [LK17]. These low-k and ultra low-k (ULK) materials, i.e. dense and porous CVD-deposited organosilicate glasses with low Young's modulus and cohesive strength, and consequently low fracture toughness, weaken the mechanical stability of the BEoL stack [Gri+14]. In addition, advanced technologies for microchip manufacturing and particularly for the subsequent advanced packaging use a large variety of materials at multiple length scales. The thermomechanical stress, which is primarily caused by the mismatch of coefficients of thermal expansion (CTE) of the materials used in the microchip and for packaging (Table 2.1) can cause propagation of microcracks and increase the risk of device failure. This effect is called chip-package interaction (CPI). It is a serious reliability concern for advanced microelectronic products, particularly caused by advanced packaging with hard interconnect materials such a lead-free solder balls and copper pillars and advanced, mechanically weak thin film materials such as porous organosilicate glass (ULK material) [WHG05].

Table 2.1: Typical materials in chip package and its Young's modules and CTE values [Gal+12, Yoo+06, Liu+17, CL18].

	Material	Young's modulus [GPa]	CTE [ppm/K]
Die level	Copper interconnects	128	16.9
	Dielectrics:		
	Dense low-k	10-20	3-10
	Porous low-k	1-5	10-18
Package level	Solder Bump (Sn-Ag-Cu-Ni)	48-54	20-22
	PCB (x/y/z)	22/22/10	17.6/17.6/64.1

The evolution of the insulating material for several technology nodes applied in semiconductor manufacturing is shown in Figure 2.1. The interconnect lines made of copper ($M1 \dots Mn$) are separated by so-called interlayer dielectrics (ILD) that firstly was silicon dioxide SiO_2 ($k = 3.9$), then fluorosilicate glass FSG ($k = 3.5$) and finally dense ($k \lesssim 2.9$) or porous ($k \lesssim 2.5$) organosilicate glasses [Gri+14].

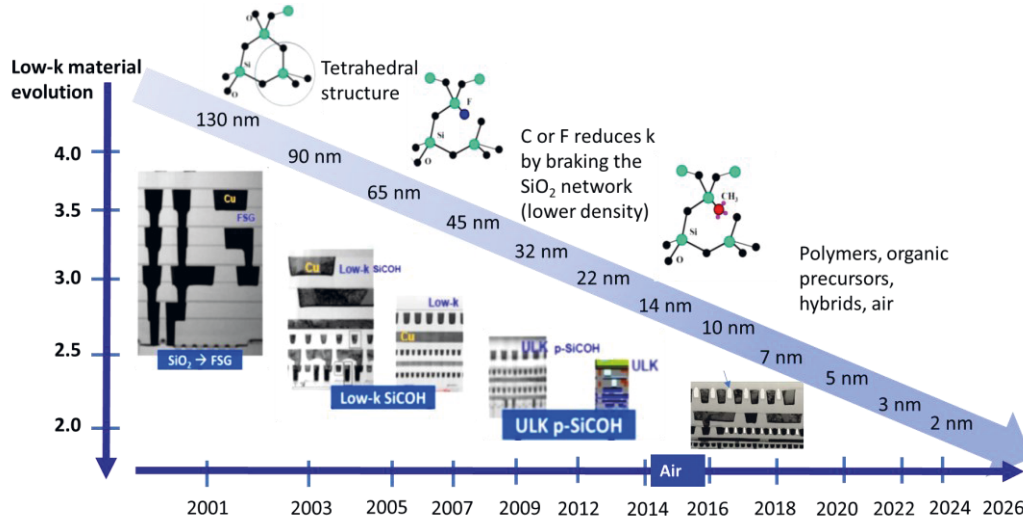


Figure 2.1: Evolution of interlayer dielectric materials [Fan16, Vol+10, Dil2021, Tra2021].

The decrease in dielectric permittivity can be achieved, if $Si-O$ bonds (in SiO_2) are partially replaced by less polar bonds such as $Si-C$, $C-C$ or $C-H$ [Sha+04]. In addition, the introduction of nanosized pores and air gaps in the material decreases k further. As mentioned above, these dense or porous organosilicate glass materials are characterized by low Young's modulus and cohesive strength, and consequently low fracture toughness [Gri+14].

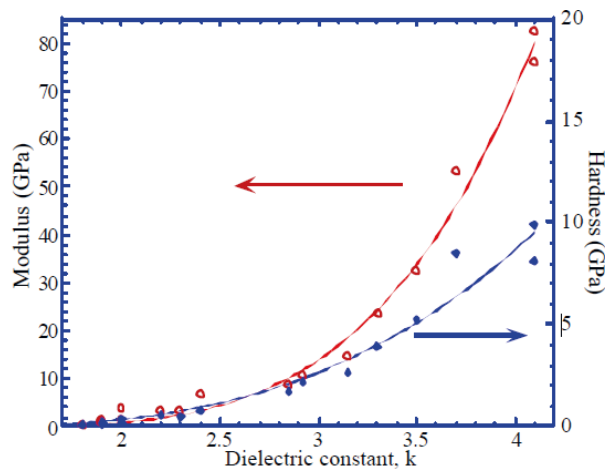


Figure 2.2: Mechanical properties of silicon based materials with varying dielectric constant [Xu+02].

That means, the Young's modulus decreases with the dielectric constant k (Figure 2.2). It reduces the mechanical stability of the BEoL stack (low stiffness) and it increases the risk of cracking and failure (low fracture toughness). In order to predict or to avoid fracture caused by crack propagation, the mechanism of crack initiation and growth have to be well understood. This phenomenon can be studied based on the fundamental principles of fracture mechanics, firstly described by Griffith for brittle materials [Gri21] and later extended by Irwin to metals by including the plastic zone at the crack tip [Irw57]. These fracture theories allow to quantitatively connect fracture stress and flaw size based on a simple energy balance:

$$G = \frac{\pi\sigma^2 a}{E}, \quad (2.1)$$

with G - energy release rate which is defined as the rate of change in potential energy with the crack area for a linear elastic material, π – mathematical constant, σ - stress, a – half crack length, E – Young's modulus. At the moment of fracture, G becomes critical $G = G_c$, the critical energy release rate, which is a measure of the so-called fracture energy or fracture toughness of the material. A crack will grow as long as the condition $G \geq G_c$ is met. If there is a steady growth of crack and if plastic deformation at the crack tip can be neglected, the released energy is used to create new surface areas on both sides of the crack. G_c is associated with a specific surface energy γ , with $G_c = 2\gamma$, and Eq. (2.1) can be written as:

$$\frac{\pi\sigma^2 a}{E} \geq 2\gamma \quad (2.2)$$

Hence, it can be seen that with an increase of stress σ due to material properties mismatch (Table 2.1) and with a decrease of Young's modulus E for low- k materials (Figure 2.1), the risk of crack propagation in the BEoL stack is dramatically increased. Typical failure modes are delamination along dielectrics interfaces (adhesive failure) and fracture in dielectrics (cohesive failure). Delamination can be caused by micro-cracks that were introduced during manufacturing, for instance during the mechanical dicing process [Bak+12]. To improve the fracture behavior of the integrated BEoL structures, a mechanically robust patterned metal stack against fabrication and packaging stresses is required.

One option that chip manufacturers are exercising to prevent fracture and mechanical chip damage is the integration of metallic guard ring (GR) structures, also called "crack stop structures", in the BEoL stack at the rim of the microchip. These GR structures are designed to dissipate energy in such a way that the propagation of cracks, which have been initiated e.g. during the dicing process, is slowed down or even stopped effectively [Zha+09]. The previously discussed weakness of BEoL mechanical material properties shows the importance

of essential questions of interface engineering discussed by Grill [Gri+08]. With decreasing dielectric permittivity of the ILD, both cohesive strength and adhesion between metal interconnects and dielectrics are decreasing linearly [Lan03, Lan+04]. As a consequence, the resistance against the growth of microcracks (e.g. dicing flaws) is reduced. The “energy balance” with its competing components such as ILD cohesive strength, crack stop energy dissipation and dicing defect energy is schematically shown for several technology nodes in Figure 2.3 [Lan+07]. Considering the continuous drop of the ILD cohesive strength and constant crack stop energy dissipation, the gap to the dicing defect energy increases from technology node to technology node. The “energy gap” can be compensated by specially designed GR structures (Figure 2.3).

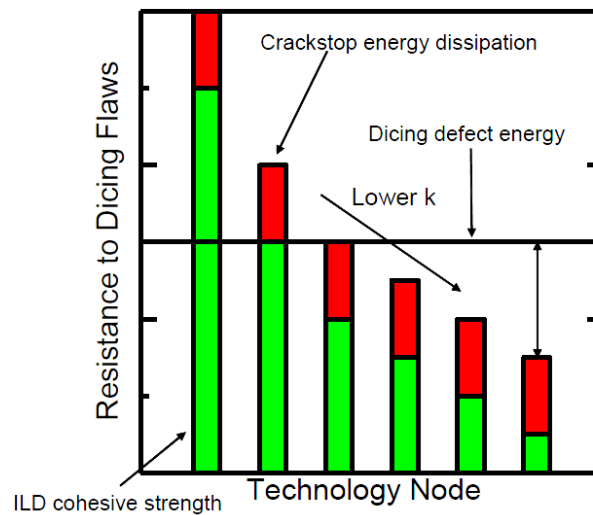


Figure 2.3: Scheme of decreasing of resistance to dicing flaws with evolution of technology node [Lan+07].

The design of on-chip interconnects, and particularly of GR structures that are mechanically robust against packaging stress, and the evaluation of the risk of mechanical failure require the understanding of the kinetics of the fracture process, the identification of weak structures in the BEO_L stack and quantitative measure of fracture resistance, e.g. G_c , under realistic and controlled loading conditions. Li et al. demonstrated a method to control crack propagation in Cu/low-k BEO_L stacks and to extract the fracture properties of metal vias and interlayer dielectrics from integrated structures [Li+13]. This experimental approach is based on a double cantilever beam (DCB) test with various specimen geometries, including symmetric and asymmetric configurations (mode mixity), and *post mortem* scanning electron microscopy (SEM) and transmission electron microscopy (TEM) imaging of the crack path.

This method allows to study how process parameters effect the properties of real interconnect materials and understand its fundamentals of fracture behavior of thin films.

2.2 Experimental studies of crack propagation in BEoL stacks

2.2.1 *Post mortem* (2D) studies

The understanding of mechanical instability and failure of patterned and / or integrated structures that can pose serious problems for the reliability of microelectronic products is currently limited by the existing characterization techniques. Although there is a wide variety of established methods for analyzing a failure *post mortem*, experimental methods that can provide real-time monitoring and control of failure behavior in realistic integrated circuits are significantly limited in resolution and applicability.

Previous studies to investigate the robustness of BEoL stacks including GR structures have been mainly 2-dimensional. One example are semi-quantitative crack observations in the SEM after nanoindentation in the *Si* substrate, the modified cross-sectional nanoindentation (MCSN) technique, proposed by Molina [Mol+07]. Cracks initiated in the *Si* substrate are forced to propagate into the BEoL comprised metal layers (M_n , $n=3$) in x direction (Figure 2.4).

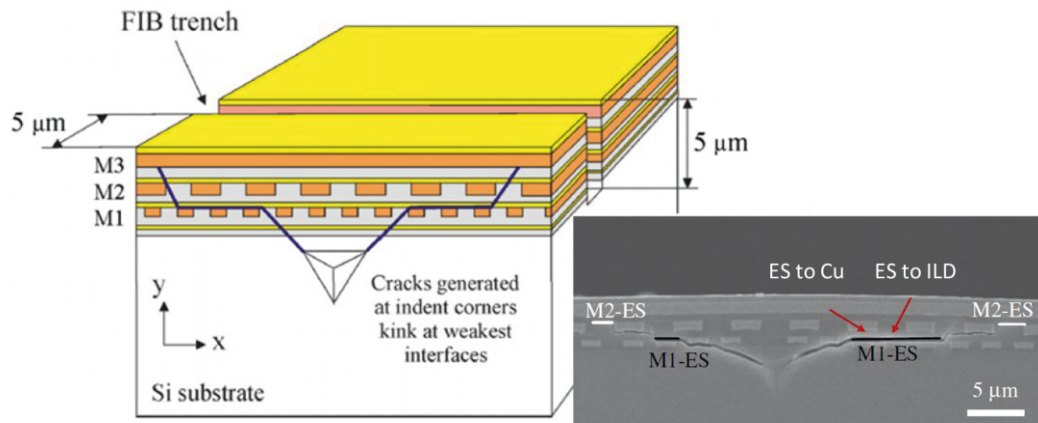


Figure 2.4: Schematics of the indentation procedure and SEM image with marked crack position along the etch stop (ES) layer to patterned Cu interfaces at the middle and lower metallization levels. Here the crack propagates across two different interfaces: ES to Cu and ES to ILD [Mol+07].

Test structures with three types of interlayer dielectrics (ILD- n , $n=3$) and four etch stop layers (ES- n with increased adhesion from ES-1 to ES-4) were investigated. As one of the

important results of this approach, the crack length along a particular interface was correlated to the fracture toughness at this interface for different samples systems as shown in Figure 2.5.

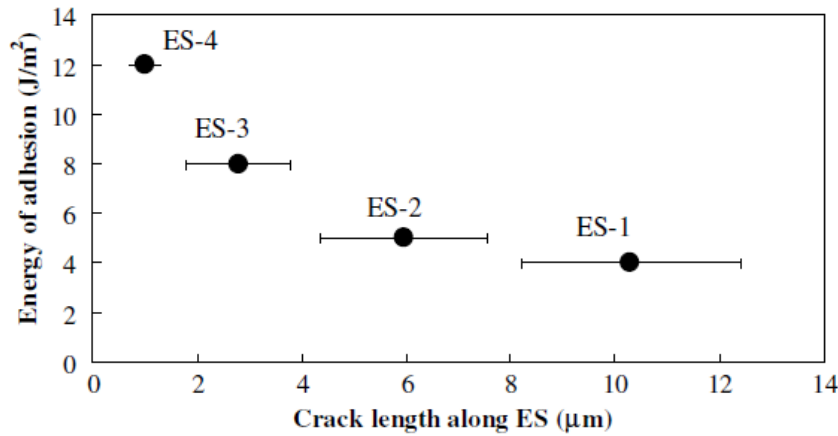


Figure 2.5: Correlation between the energy of adhesion for the interface ES/Cu measured by four-point bending and the crack length along the same interface measured by MCSN for the case of ILD-2 (ES/ILD-2 adhesion energy is about 3 J/m² in all cases). Error bars represent the standard deviation for the mean value for 5–7 indentations. Typical standard deviation for four-point bending is 10% [Mol+07].

The MCSN technique developed by Molina et al. [Mol+07] has been proven useful to study fracture processes in on-chip interconnect stacks. Main advantages of this method are: (1) Provides information on the interaction crack/BEoL metal structure; (2) Useful to find local differences in adhesion; (3) Qualitative quick monitor of bad/good adhesion; (4) Provides information about the efficiency of crack stop structures. However, this technique has several limitations. Here, a 2D approach is chosen which provides no or very limited information about the real situation in a 3D on-chip interconnect stack. That means, no information can be deduced regarding an effective BEoL design and particularly for the design of GR structures. In addition, even a very careful sample preparation changes the mechanical stress state and causes some stress release. There is always the risk of introducing preparation artefacts. And finally, this destructive experiment does not allow the study of crack growth kinetics in a region of interest (surrounding material) that is not destroyed.

Other experimental approaches to quantitatively determine the effective toughness of different designs of GR structures, based on the four-point bend (4PB) test and Modified Edge Lift-off Test (MELT) were reported [Sha+07]. These two tests mimic different loading conditions closely related to the real CPI. In both cases, identical test structures made of a processed wafer and covered by an epoxy layer were investigated. In case of 4PB an additional

dummy wafer glued onto the test structure was cut into sandwich-like bend bars. A notch as initial crack is created in the middle of the achieved beam. This crack is propagating to the BEoL stack and further along the weakest interface within the BEoL stack. As an example, the 4PB test scheme and a typical load-displacement curve are shown in Figure 2.6.

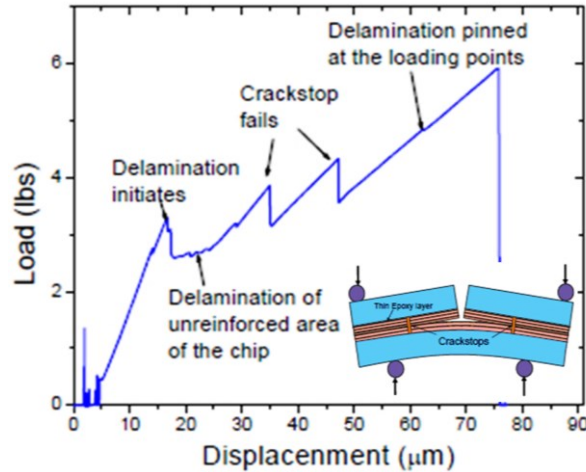


Figure 2.6: Load displacement trace from four-point bend (4PB) testing of crack stops in an eight level BEoL structure with 4PB test configuration for testing crack stop structures [Sha+07].

From the peak loads at which the crack stops failed, the critical crack driving force was determined to be 2 to 2.5 times of the cohesive strength G_0 of the unreinforced dielectrics. It was shown experimentally that modification of the crack stop design can provide values up to 6 times of G_0 [Sha+07]. 4PB and MELT methods require to determine the location where the crack stops with an optical microscope. The determination of the location of the failure in the BEoL stack needs further *post mortem* studies using TEM.

Micro-scale mechanical properties including fracture of brittle materials including silicon, studied with SEM and TEM, were reported recently [Jav+16, Bes+16, Ger+17]. SEM provides mainly surface information and TEM requires extremely thin samples ($< \sim 200$ nm). However, the visualization of cracks in opaque materials and structures is usually not possible using light or electron microscopy due to the limited penetration of the (visible light) photons and electrons into bulk materials. Taking into account the 3D packaging trend and the integration of new materials, the 2D information is not sufficient for the evaluation of the crack evolution in realistic fully integrated multilevel interconnect structures of microchips. In addition, most of the *post mortem* studies do not reflect the real crack behavior and cannot provide any information about the kinetics of the fracture mechanisms in 3D material systems.

Current state of the art -using standard DCB testing without the ability to trace the path of a crack *in-situ* [Li+13]. By changing the experimental parameters of the DCB setup, the crack path can be changed, but the crack path can only be assessed after the test, and it is impossible to fully assess the physical mechanisms leading to crack initiation, crack propagation and subsequent severe delamination. This clearly indicates the need for a non-destructive 3D imaging technique to study the crack behavior in integrated structures with the ability to measure fracture material properties. In addition, it is important that the installed test systems can mimic and bring the stress state closer to reality. In particular, measurements of local material properties are becoming more important for nanoscale materials such as nano-patterned structures. To be meet these demands the combination of a high-resolution X-ray microscope and micromechanical test is a preeminent choice.

2.2.2 *In-situ* kinetic (3D) studies

X-ray imaging is a non-destructive analysis method due to the ability of X-rays to penetrate matter which is opaque for visible light. The method to reconstruct a volumetric (3D) data set from a series of radiographic (2D) images collected from many view directions is called X-ray computed tomography (XCT). This technique allows to analyze the internal structure, without cutting or sectioning the region of interest, hence it provides 3D image data non-destructively. X-ray imaging is performed either in projection mode using a micro-sized X-ray source (micro-X-ray computed tomography, micro-XCT) or in the microscopy mode using an X-ray objective lens in a microscope setup (transmission X-ray microscopy, TXM / nano-X-ray computed tomography, nano-XCT). The final 3D image is produced by transforming a set of 2D X-ray projection data applying a mathematical process called tomographic reconstruction [KS88]. This reconstructed 3D dataset allows to analyze the internal structure with virtual cross-sections through a specific sample thickness, limited by the photon energy, with a specific resolution, limited by the focal spot of the X-ray source in the case of micro-XCT or the objective lens in the case of TXM / nano-XCT [KJ09].

Since 3D-stacked microelectronic products include multiscale feature sizes (from millimeters to nanometers), the choice of the specific XCT setup (projection mode or microscopy mode) depends on the needed field of view and resolution. The state of the art of the X-ray imaging techniques over resolution is schematically summarized in Figure 2.7.

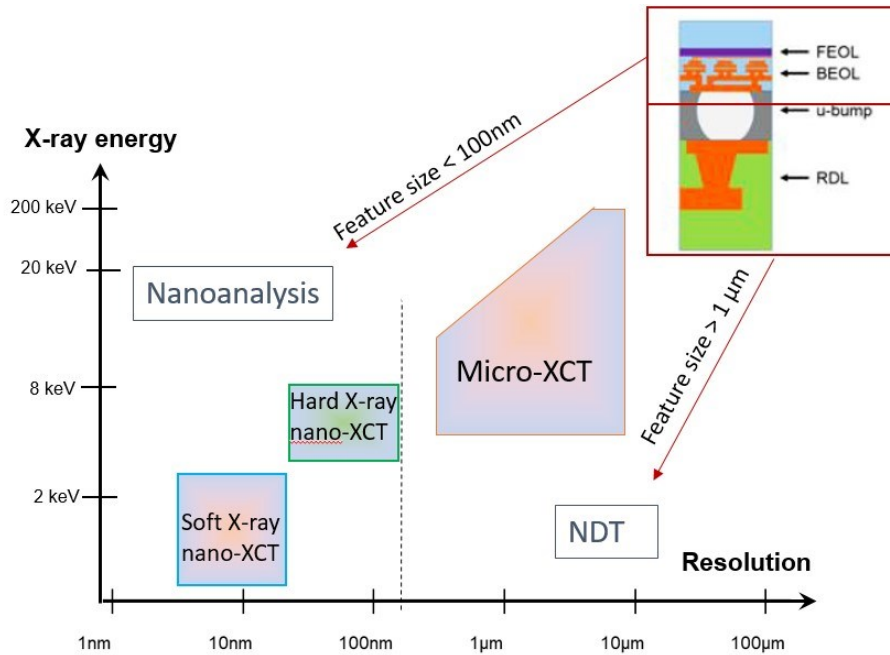


Figure 2.7: Overview of the current X-ray imaging set-ups at several photon energies and resolution.

The ability to view images from any angle as well as across multiple planes enables an effective fault detection for 3D structures and provides information for process improvements. There are many reported studies on non-destructive characterization of multiple levels of interconnects in 3D microelectronic packages, including micro-bumps, based on conventional micro-XCT set-ups with a resolution of 4 - 8 μm [Li+14] and some with sub-micrometer resolution down to 0.2 μm [Har+18, Zul+17, Lut+21]. However, for the on-chip interconnect stack, the so-called BEoL, with structures in the sub-micron range or even in the sub-100 nm range, high-resolution X-ray microscopy is required.

Direct observation of the crack path evolution to determine the weakest structures in the BEoL stacks requires a combination of mechanical testing with high-resolution imaging of cracks in on-chip interconnect stacks [Kut+17]. For 3D crack imaging in BEoL stacks, nano-XCT with a resolution of < 100 nm is needed. This technique is based on TXM which allows to gather non-destructively information for significantly larger sample volumes compared to TEM: samples thickness is about 2 μm to about 50 μm , for photon energies from 1 keV to 8 keV (for comparison: the thickness of a typical TEM lamellae is about 100 nm).

The approach proposed in this thesis, i.e. the 3D imaging of BEoL structures including cracks and crack propagation with high resolution, has several advantages compared to the 2D-based techniques such as the MCSN approach [Mol+07]. X-ray microscopy and nano-

XCT are really 3D imaging techniques, and with the integration of mechanical setups into the X-ray microscope, it is possible to study the 3D crack evolution in BEoL stacks.

2.3 State of the art study of mechanical properties and 3D imaging of BEoL stacks

2.3.1 Conventional DCB test

Mechanical tests such as 4PB test and DCB test were specially designed to measure adhesion properties within layer stacks, deposited on a planar substrate [Dau+98]. Although the 4PB test is typically applied, the DCB test, firstly presented by J. J. Benbow and F. C. Roesler in 1957 [BR57], has been well introduced to measure adhesion properties of layer stacks. While normal and shear stresses occur at the crack tip for the 4PB test (mixed mode I/II condition), the tensile stress normal to the plane of crack dominates for the DCB test [Cha+89]. The respective crack is subjected to mode I condition. The sample of interest (substrate and layer stack) is glued to a dummy sample (substrate only), usually with similar dimensions, to obtain a sandwich structure in such a way that the layer stack to be studied is located in its centre. In contrast to other methods, like tensile or shear tests, a notch is cut into the test sample to have a defined initiation point for the crack evolution. The crack is guided to the mechanically weakest thin film or interface, and, subsequently, the load is applied such that stable crack propagation occurs in a controlled way. As a result of the DCB test, the weakest (cohesive or adhesive) bindings in the thin film material or of an interface can be identified, and the energy release rate for crack propagation within the weakest sub-layer or along the weakest interface can be determined quantitatively. The standard DCB test is one of the most common experimental techniques for determination of the critical energy release rate G_c of macroscopic specimens with plane interfaces. A typical DCB test geometry is schematically shown in Figure 2.8. This scheme includes the geometric measures of a partially delaminated sandwich sample and it indicates the force introduction points. A force F is applied perpendicular to the interfacial plane of the DCB sample to create an interfacial crack with a length L and a crack opening Y (sum of both single beam deflections $u_{y_n}(L)$, $n = \{1,2\}$) at the sample mount position $x = L$ ($x = 0$ at crack tip).

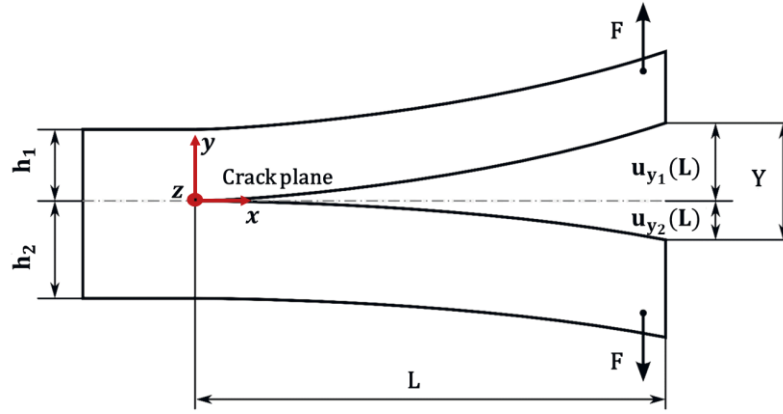


Figure 2.8: Illustration of a partially delaminated standard DCB geometry with freely rotatable beam ends at the force introduction points: F – applied force, h_1 and h_2 – beam heights, $u_{y_n}(L)$ – cantilever deflections at the end of the beam in y , $n = \{1, 2\}$, $Y = u_{y_1}(L) + u_{y_2}(L)$ – maximum beam opening, x – coordinate in interface/crack plane direction with origin in the crack tip, y – coordinate perpendicular to the interface/crack plane, L – crack length.

The energy release rate G is the normalized amount of elastic energy U_{el} stored in the system, which will be released if the crack with a length x propagates. It can be expressed (in contrast to Eq. 2.1) by the following equation:

$$G = -\frac{1}{b} \frac{dU_{el}}{dx}, \quad (2.3)$$

with b being the sample width. Depending on the loading conditions, the energy can be expressed under load-controlled conditions or displacement-controlled conditions [And05, Kun08]. The critical energy release rate G_c that it needed for crack growth can be determined by the condition that the external energy is equal to the stored elastic energy. That means, crack growth is initiated when the energy release rate is larger than a critical value G_c , i.e. $G > G_c$.

2.3.2 Micromechanical test set-up in X-ray microscope

The crack path in a material can be described based on a microscopy and spectroscopy study of the fracture surfaces of the cracked sample, i.e. *post mortem*. However, kinetic studies of the crack evolution are needed to understand the kinetics of fracture in heterogeneous materials and 3D structures, i.e. based on a non-destructive investigation. One of the first kinetic studies in X-ray microscopy was the *in-situ* imaging of electromigration in an on-chip interconnect test structure of a microchip [Sch+02]. This study, performed on a synchrotron

facility with an achieved resolution of 30 nm, demonstrates the advantage of high-resolution X-ray imaging for kinetic studies.

Macroscopic test systems such as the DTS Delaminator (DTS, Menlo Park, CA) [Dau05] consist of a stiff frame, an actuator, and appropriate sensors to measure the applied force and the displacement. Both 4PB and DCB tests are possible with this test system. The samples used have the dimension 1.6...2.0 mm x 3.5 mm x 50 mm, which is much too large for transmission of X-ray photons of an energy of 8 keV (Cu-K α radiation), which is commonly used for X-ray microscopy. Therefore, a novel micro-DCB test was designed for samples that are transparent for photons of 8 keV energy [Nie15]. Depending on the material, a typical cross-section of such samples is about 50...100 μm x 50...100 μm . The advantage of the micro-DCB approach is that the crack evolution can be imaged *in-situ* using X-rays. On the other hand, the efforts for sample preparation are larger than for the macroscopic 4PB and DCB tests. The DCB test was chosen because of its intrinsically given symmetry, in contrast to the 4PB test where the center of the sample is moving during mechanical loading. That means, no sample translation is needed during load increase in the X-ray microscope. Furthermore, the points of load incidence of the test system to the sample are only located on one side of the crack tip, which is an essential advantage for the data acquisition during sample rotation for 3D tomographic imaging since the test system does not shadow the X-ray beam. The comparison of main parameters and features of these tests are presented in Table 2.2 below.

Table 2.2: Comparison of standard DCB and micro-DCB tests

Design	Standard DCB test	Micro-DCB test in a nano-XCT tool
Parameters		
Feature	<i>ex-situ, post mortem</i>	<i>in-situ</i> , kinetic studies
Sample size	1.7x5x50 mm ³	50x50x1000 μm^3
Efforts	Low: Bonding, sawing, notching	Height: Bonding, thinning (polishing, grinding), sawing, advanced notching, assembly on test fixture and alignment to the X-ray beam

Advantages	<ul style="list-style-type: none"> - Well described fracture mechanics models - Pure fracture mode I - High number of samples possible, statistically relevant data 	<ul style="list-style-type: none"> - <i>In-situ</i> crack path investigation - Controlled microcrack steering - 3D data set of the crack front - Determination of local energy release rate
Disadvantages	<ul style="list-style-type: none"> - High efforts of <i>post mortem</i> sample investigation is required to determine the location of the crack in the BEoL stack (SEM/TEM, FIB, spectroscopy) - 2D information of crack front 	<ul style="list-style-type: none"> - Fracture mechanics for small dimensions still in development - Analytical model required - High impact of sample geometry – no pure fracture modes - Low number of samples

Geometrical requirements and boundary conditions of a micro-DCB test in an X-ray microscope set-up are:

- (1) A rigid design of the fixture (micro-DCB test);
- (2) A stable operation of the experiment for one day, considering a total displacement of less than 30 μm ;
- (3) Fit of the fixture onto a base plate with a kinematic mount as used for the commercially available holders;
- (4) No collisions with other parts of the X-ray microscope;
- (5) The ability to acquire radiographs during full rotation of the sample without restrictions (XCT), particularly no shadowing.

In this thesis two micro-DCB test setups are presented, which were built according to these requirements.

3 Advanced micro-DCB test in X-ray microscope

3.1 Laboratory based X-ray microscopy

In this thesis, two micromechanical setups are applied in a laboratory TXM operated at 8 keV photon energy to detect opened cracks in dielectrics and along interfaces of Cu/low – k on-chip interconnect stacks. The *in-situ* observation of crack evolution with a spatial resolution of sub-100 nm provides detailed information on the fracture behavior of microchips and particularly on the robustness of the BEoL stack. This chapter describes the unique micromechanical set-ups, recently designed and integrated into a laboratory TXM.

A commercial laboratory X-ray microscope (Xradia nanoXCT-100) equipped with a rotating anode X-ray source (predominantly Cu-K α radiation, 8 keV photon energy) and two exchangeable Fresnel zone plates (FZP) as imaging lenses were used. The two FZP were applied for overview imaging (10x FZP magnification x 20x optical magnification = 200x total magnification) and high-resolution imaging (40x FZP magnification x 20x optical magnification = 800x total magnification), providing switchable pixel size and field of view configurations of 65 nm at 67 μm x 67 μm and 16 nm at 16.5 μm x 16.5 μm (for 200 x and 800 x total magnification), respectively [MG13, Tka+07]. The spatial resolution of sub-100 nm was demonstrated using a Siemens star test structure [Nie15]. A rotation stage provides the capability of X-ray computed tomography. Usually, virtual 2D cross-sections are used for illustration of the 3D data.

The first miniaturized piezo-driven mechanical micro-DCB test set-up was integrated to visualize crack opening and propagation under applied displacement-controlled load [Nie15]. The sample was mounted on the micro-DCB tester which was positioned on the rotation stage for *in-situ* radiography and tomography. It is shown schematically in Figure 3.1.

This particular DCB test geometry was chosen for several reasons:

(1) the sample could be positioned on top of the sample holder/testing device, with no part of the fixture shadowing the region of interest during sample rotation, and thus minimizing tomography artifacts;

(2) the sample could be aligned in a way that the crack front was parallel to the optical axis of the X-ray microscope, which is the preferred geometry to obtain radiographs.

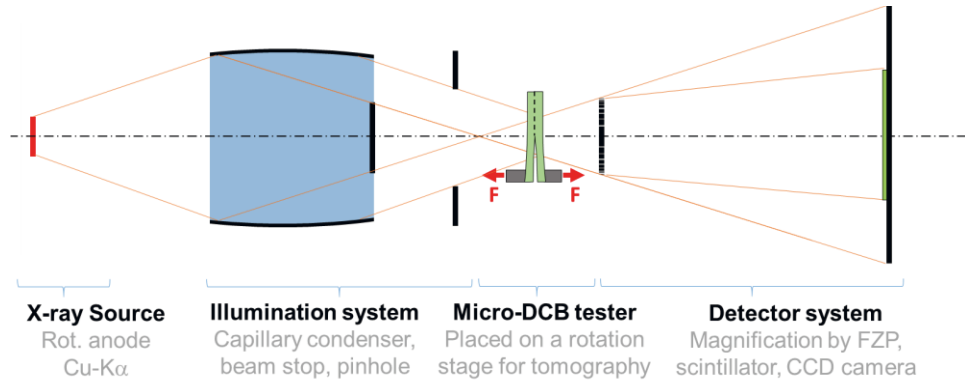


Figure 3.1: Scheme of the micro-DCB test inside X-ray microscope.

3.2 Micro-DCB test set-up

3.2.1 Experimental setup and operation

Figure 3.2 (a) provides the scheme of the micro-DCB test set-up and Figure 3.2 (b) shows how the fixture is positioned on the rotation stage for tomography in the X-ray microscope. The sample is mounted on top of the fixture, which itself is designed as a monolithic device. In addition to the sample position, characterized by the rotation axis for X-ray tomography (Y axis), the direction of the X-ray beam (Z axis) and the direction of the applied load (X axis) are indicated. Hence, the entire sample can be imaged at arbitrary rotation angles without shadowing, except for the bottom part attached to the sample holder.

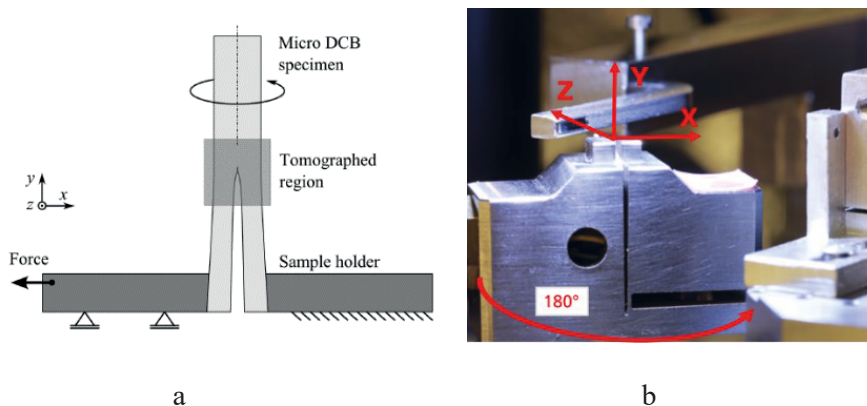


Figure 3.2: (a) Scheme of the micro-DCB test, (b) micro-DCB test setup inside the X-ray microscope: Z axis: X-ray beam direction, Y axis: rotation axis of the sample (sample fixed on sample holder as in (a)), X axis: direction of applied load [Nie15].

The micro-DCB tester is displacement-controlled, i.e. one side of the sample holder is fixed and the other side can be moved horizontally, typically in 50 nm to 100 nm steps, up to

a maximum displacement of 30 μm to 40 μm . The test setup enables a stable operation of the experiment for one day.

The micro-DCB setup is designed for X-ray microscopy and tomography application, i.e. for rotating the sample 180° without shadowing to study *in-situ* the propagation of microcracks in multilayered structures. The mechanical preparation of dedicated specimens for micro-DCB experiments in the nano-XCT tool is explained in [Nie15]. Furthermore, the micro-DCB test design allows to quantify the fracture properties of the multilayered stack (Cu/low-k) through determination of the local energy release rate G . The first applications to crack propagation in materials and multilayers are reported in [Nie15, Kut+18b, Kut+17]. An analytical approach to quantify the energy release rate G is published in [Nie15]. To study more precisely the mechanical properties of the special designed BEOl stacks with GR structures, an advanced analytical approach for micro-cantilevers was developed as described in section 3.2.2.

3.2.2 Determination of energy release rate using micro-DCB test

In this study, the Euler-Bernoulli beam theory is applied to two micro-DCB cantilevers for the determination of the stored elastic energy and eventually of the energy release rate G for crack propagation in patterned structures. The G value is defined as the rate of change in potential energy with the crack area for a linear elastic material. It is possible to determine the local fracture resistance (G_c) of crack stop structures under realistic loading conditions.

The symmetric double beam geometry ($h_1 = h_2$) for the DCB test results in a pure normal force crack opening, the so-called fracture mode I (Chapter 2, Figure 2.8). However, geometric inaccuracies of the sample, i.e. deviations from a symmetric micro-DCB sample, result in asymmetric bending of the beams. Such inaccuracies are more pronounced in the micro-DCB test compared to the conventional DCB test applied in fracture mechanics. Additionally, non-symmetry can also be applied intentionally to steer the crack in multilayered stacks. This non-symmetry causes an additional shear component in the crack driving forces (mixed I and II mode), and the determination of the single beam deflections $u_{y_n}(L)$ becomes important. For demonstration, the typical geometric sizes in a real micro-DCB sample are indicated in a stitched radiograph in Figure 3.3.

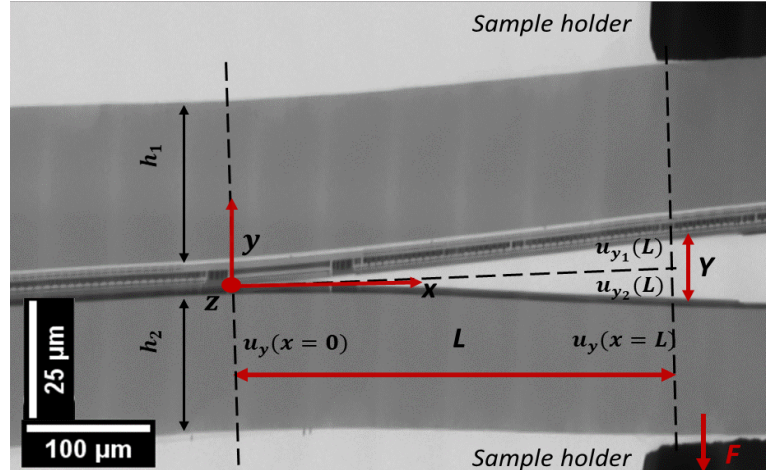


Figure 3.3 Stitched radiograph of a micro-DCB sample. The stitching array of $3y \times 12x$ radiographs is compressed along the x coordinate for better visualization of the geometry.

For the micro-DCB geometry used in this study, the single beam deflections $u_{y_n}(L)$ and other experimental parameters are not directly accessible from the measured data. To determine these experimentally not accessible parameters of the Euler-Bernoulli bending beam differential equation was applied [BR57, BC09]. In the case of small deflections, which approximately applies for the micro-DCB geometry, the shape of the two bending cantilevers can be described by the Euler-Bernoulli differential equation:

$$q = \frac{d^2}{dx^2} \left(EI \frac{d^2 u}{dx^2} \right) \quad (3.1)$$

where q is a distributed load (in N/m^2), E is the Young's modulus (in Pa), $I = I_{zz}$ is the second moment of area (in m^4) for a bending around the out of plane coordinate z (called just I in the following), and $u(x)$ is the beam transverse displacement in y direction at the position x , called the bending line. The term $\frac{d^2 u}{dx^2}$ (or short u'') is the second derivative of the beam deflection. Often the material property E and the geometry parameter I are constant, and consequently, the product EI , which is called flexural rigidity, is also constant. According to Eq. (3.1), the following relations of the bending line $u(x)$, with its slope u' , subsequent derivatives, as well as the loading quantities as shear force Q , bending moment M and distributed load q can be written as:

$$q(x) = \frac{dQ(x)}{dx} = \frac{d^2}{dx^2} \left(EI \frac{d^2 u}{dx^2} \right) \quad (3.2)$$

$$Q(x) = \frac{dM(x)}{dx}; \quad (3.3)$$

$$M(x) = -EI \frac{d^2 u}{dx^2}; \quad (3.4)$$

$$u'(x) = \frac{du}{dx} \quad (3.5)$$

To determine the bending line $u(x)$, a four-step integration from $q(x) \rightarrow u(x)$ including the integration coefficients C_1 , C_2 , C_3 and C_4 was performed to achieve the deflection equation including all micro-DCB-adapted boundary conditions. A schematic representation of the boundary conditions and of the different parameters along the beam length is shown in Figure 3.4.

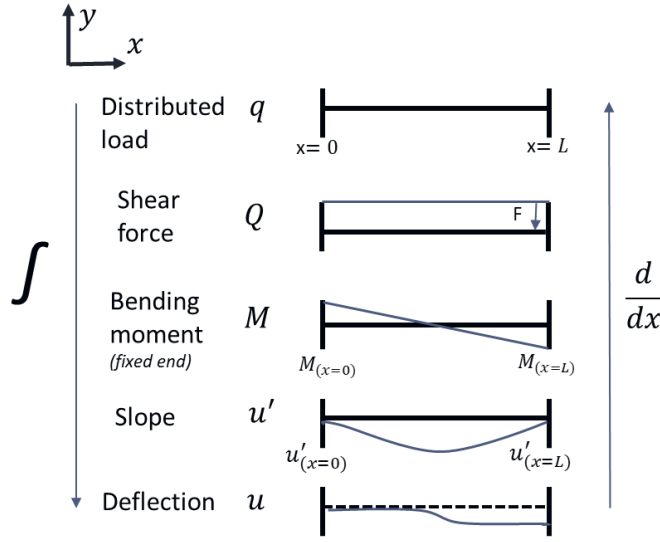


Figure 3.4 Sketch of the bending beam solution highlighting the boundary conditions.

For the micro-DCB geometry, the fixed end of the Euler-Bernoulli beam was chosen at the crack tip position which is defined as $x = 0$. There, the deflection is $u(x=0) = 0$ and the slope is $u'(x=0) = 0$. At the force introduction point, at the beam length $x = L$, the boundary conditions for the micro-DCB geometry deviate from those for the standard DCB geometry. The main difference are the boundary conditions in the bending slopes $u'(x)$ and bending moments $M(x)$ at $x = L$. For the standard DCB geometry, the beam is free to move at $x = L$, and consequently, the bending moment is zero at this point. The slope has a value of non-zero. For the micro-DCB geometry, the beam end at the force introduction points is fixed due to the sample mounting using gluing. A fully fixed beam would lead to boundary conditions of $u'(x=L) = 0$, and the bending moment would be non-zero. In reality, the boundary conditions at $x = L$ of the micro-DCB geometry is between those extremes, i.e. $u'(x=L)$ as well as $M(x=L)$ are non-zero. To adapt to these intermediate boundary conditions, a parameter A is introduced to describe the amount of fixture at the beam ends at $x = L$. The value A is in the range of $0.5 \leq A \leq 1$ with the extremes $A = 0.5$ for $u'(x=L) = 0$ and $A = 1$ for $M(x=L) = 0$. With respect to the micro-DCB test, the situation of the two

extreme cases “fixed beam ends” and “free beam ends” due to geometrical parameter A is shown schematically in Figure 3.5. More details are given in the bending equation solution below.

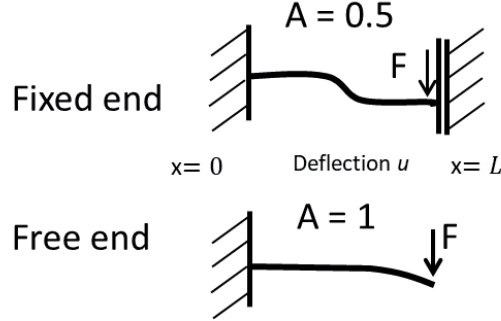


Figure 3.5: Scheme for two extreme cases, fixed cantilever ends and free cantilever ends.

To solve the bending beam differential equation, a stepwise integration and boundary condition implementation is applied. Start is the line load equation Eq. (3.2). The first integration of the line load $q(x)$ equation provides the shear force $Q(x)$:

$$Q(x) = \int q dx + C_1. \quad (3.6)$$

As in the micro-DCB geometry the line loads are zero, $q(x) = 0$, the integration constant equals the shear force $C_1 = Q$, which is a constant along the beam and equals the applied force F . Therefore, the first integration coefficient $C_1 = F$. Then, the second integration of the moment $M(x)$ is determined as [cp. also Eq. (3.4)]:

$$M(x) = \int Q dx = \int F dx + C_2 = Fx + C_2 = -E I u'', \quad (3.7)$$

$$-E I u'' = Fx + C_2. \quad (3.8)$$

For the determination of the integration coefficient C_2 , the specific micro-DCB geometry and its extreme cases need to be considered. In case of a fully blocked free end of the cantilever [$u'(x=L) = 0$], the bending moments at $x=0$ and $x=L$ are symmetric:

$$M_x(x=0) = -M_L(x=L) \quad (3.9)$$

$$F * 0 + C_2 = -F * L - C_2 \rightarrow 2C_2 = -FL \rightarrow C_2 = -\frac{FL}{2} \quad (3.10)$$

In case of a fully rotatable beam and at $x=L$, the bending moment at $x=L$ is zero. With Eq. (3.7) this equals to:

$$M(x=L) = 0 = FL + C_2 \rightarrow C_2 = -FL \quad (3.11)$$

Taking into account the different boundary conditions at the beam end $x = L$, a factor A is introduced and the boundary condition C_2 is defined as:

$$\frac{FL}{2} \leq -C_2 \leq FL; C_2 = -A*FL; 0.5 \leq A \leq 1 \quad (3.12)$$

Taking to account C_2 , Eq. (3.7) can be written as:

$$M(x) = -EI * u'' = -Fx + \frac{AFL}{2}. \quad (3.13)$$

Next integration of the second derivative of the bending line $u''(x)$ provides the equation for slope u' and the integration coefficient C_3 :

$$\int u''(x)dx = \int \left[\left(-Fx + \frac{AFL}{2} \right) * \frac{1}{EI} \right] dx + C_3, \quad (3.14)$$

$$u'(x) = -\frac{F}{2EI}x^2 + \frac{AFL}{2EI}x + C_3. \quad (3.15)$$

This equation provides the slope of the bending beam as a function of the parameter A with $0.5 \leq A \leq 1$. The integration constant C_3 can be determined with the slope boundary condition at $x = 0$: Implementation of $u'(x = 0)$ in Eq. (3.15) leads to $C_3 = 0$. Then, $u'(x)$ can be written as:

$$u'(x) = -\frac{F}{2EI}x^2 + \frac{AFL}{EI}x. \quad (3.16)$$

The final integration step is to determine the beam bending line $u(x)$:

$$\int u' dx = u(x) \rightarrow u(x) = -\frac{F}{6EI}x^3 + \frac{AFL}{2EI}x^2 + C_4. \quad (3.17)$$

Similarly to C_3 , C_4 can be determined using the boundary condition at $u(x = 0) = 0$. Using Eq. (3.17), it results in $C_4 = 0$. With this, a full formulation of the bending line including the micro-DCB specific boundary conditions is given. It is a relationship between the applied force F , the bending line shape, and the resulting beam deflections u_{y_n} $\{n = 1, 2\}$ for the two uniform beams of the micro-DCB experiment:

$$u_{y_n}(x) = -\frac{Fx^3}{6EI_n} + \frac{A_nFLx^2}{2EI_n}. \quad (3.18)$$

The Euler-Bernoulli beam model is valid for beams under the assumptions that the beam cross-section dimensions are small compared to the beam length (equals crack length here) and that the constrained beam ends at the support side (crack tip here) are horizontally oriented. It is applied to the two micro-DCB cantilevers.

The energy release rate G for micro-DCB geometry will be derived from Eq. 2.3. For displacement control test conditions, the external energy needed for crack propagation U_{el} can be calculated by integration over the applied force F up to the maximum beam deflection $u_{\bar{y}}(L)$:

$$U_{el} = \int_0^{u_{y_n}(L)} F(x) dx. \quad (3.19)$$

There is u_{y_n} $\{n = 1, 2\}$ for the two uniform beams of the micro-DCB experiment:

$$u_{y_n}(x) = -\frac{Fx^3}{6EI_n} + \frac{A_n FLx^2}{2EI_n}. \quad (3.20)$$

The value A is in the range of $0.5 \leq A \leq 1$.

The force equation is given from Eq. (3.20):

$$F = \frac{6EI u_{y_n}(x)}{x^3 - 3A_n Lx^2}. \quad (3.21)$$

Considering this energy equation, the following result is derived for each cantilever, i.e. for $n = \{1, 2\}$:

$$U_{el,n} = \frac{3EI u_{y_n}(L)^2}{L^3(3A_n - 1)}. \quad (3.22)$$

Inserting Eq. (3.22) into Eq. (2.3) and considering that the second moment of inertia of the beam's rectangular cross-section is $I = b^3 h^3 / 12$, with b , h_n - width and height of cantilever n , $n = \{1, 2\}$, G_n for one cantilever can be written:

$$G_n = \frac{3Eh_n^3 u_{y_n}(L)^2}{4L^4(3A_n - 1)}. \quad (3.23)$$

Consequently, the G_c value for the crack propagation in the micro-DCB test can be described as the sum of the two beams:

$$G_c = \sum_1^{n=2} \frac{3Eh_n^3 u_{y_n}(L)^2}{4L^4(3A_n - 1)}. \quad (3.24)$$

The beam deflections can be expressed by simple algebraic relationships between the measurable geometric parameters $Y = u_{y_1}(L) + u_{y_2}(L)$, h_1 and h_2 (Figure 3.3) and beam ratio $e = \frac{h_1}{h_2}$, the single beam deflections become:

$$u_{y_1}(L) = \frac{Y}{(e^3 + 1)}, \quad (3.25)$$

$$u_{y_2}(L) = \frac{e^3 Y}{(e^3 + 1)}. \quad (3.26)$$

Finally, the G_c value for the crack propagation in the micro-DCB experiment, taking into account the parameters A_1 and A_2 and the beam ratio e becomes:

$$G_c = \frac{3Eh_1^3Y^2}{4L^4(e^3+1)^2} \left(\frac{1}{(3A_1-1)} + \frac{e^3}{(3A_2-1)} \right) . \quad (3.27)$$

This equation considers geometrical parameters for both cantilevers. Therefore it is applicable for symmetric and asymmetric (mode mixity) sample geometries. The determination procedure of parameter A is based on the stitched radiographs analysis (described in Appendix A1 Image analysis to determine parameter A). Stitched radiographs include $3x * 12y$ (sample length) FOVs at each loading state. The amount of applied load is estimated based on the sample geometry and deflections (incl. parameter A).

The micro-DCB tester, created and designed in [Nie15] (Chapter 3.2) is noted as micro-DCB. It is applied for the quantitative determination of the energy release rate G (Chapter 4). One way to better understand the loading and boundary conditions of beams are the direct force measurements at each loading state. Therefore, one part of this thesis is devoted to the development and proof-of concept of a novel design of the micro-DCB tester with continues force measurement capabilities, also suitable for a dynamic study perspective (e.g fatigue). This tester with force sensor, designed in this thesis, is named micro-DCB 2.0 (Chapter 3.3). The validation of the experimental determination of energy release rate G on the reference structures for both micro-DCB testers is described in Chapter 3.4.

3.3 Micro- DCB test with force sensor - Micro-DCB 2.0

Both testers described in this thesis are displacement controlled, however a load cell for force measurements is implemented into the micro-DCB 2.0 test system, which provides information about the loading state during the measurement of the force-time curve. i.e. without any numerical calculations (as needed for micro-DCB test as described in Chapter 3.2). In addition, for the further data analysis, measured force and radiographs can be easily synchronized. The design of the micro-DCB 2.0 setup considers all major practical requirements and boundary conditions as described in previous section 2.3.1.

The micro-DCB 2.0 stage is built on the standard rotation base plate of the Xradia nano-XCT-100 tool (Appendix B1). In Figure 3.6 the micro load cell (along the Z axis, shown in white), a force sensing module based on strain gauges, enables to measure forces up to 1 N.

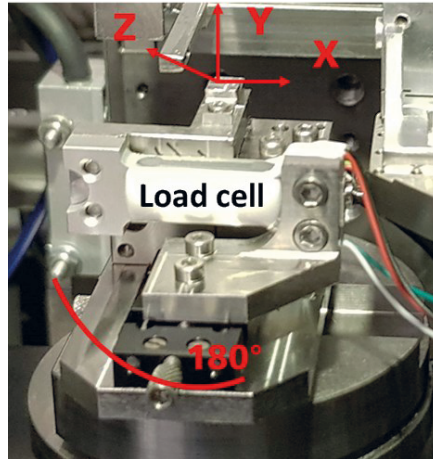


Figure 3.6: Micro-DCB 2.0 test setup inside the X-ray microscope. Z axis: X-ray beam direction, Y axis: rotation axis of the sample X axis: direction of applied load.

The piezo actuator PU 40 SG (Piezosystem Jena GmbH, Jena, Germany) was chosen for the micro-DCB 2.0 setup. It has a single axis motion of 40 μm in open loop and of 32 μm in closed loop. The NV40 / 1CLE voltage amplifier controls the piezo elements with integrated measuring system. The controller is located outside the X-ray shielding and connected through LEMO 0S.302 and LEMO 0S.304 to the piezo and through RS232 socket to the computer. The detailed drawings of the micro-DCB 2.0 tester as well as the developed Graphical User Interface (GUI) for the data measurements, synchronization and recoding are available in Appendix B2.

Table 3.1. summarizes main parameters of both testers: micro-DCB and micro-DCB 2.0.

Table 3.1.: Comparison of micro-DCB tests set-ups.

Design	Micro-DCB	Micro-DCB 2.0
Parameters		
Hardware	- Piezo (open/closed loop) with max 35 μm	- Piezo (open/closed loop) with max 40/32 μm correspondingly - Force sensor max 1 N, calibration before test is required

Integration into nano-XCT/operation	<ul style="list-style-type: none"> -Tomographic access – 360° -Manual operation (through piezo controller communication [Nie15]) 	<ul style="list-style-type: none"> -Tomographic access – 180° -Manual/Semi-manual operation -Automatic data generation and recording
Quantitative (G)	<ul style="list-style-type: none"> -Crack length and crack opening measurement, beam thicknesses -Fitting procedure to find parameters A for loading steps [4] -Solution: Euler-Bernoulli theory for special boundary condition 	<ul style="list-style-type: none"> -Geometrical parameters (crack length, beam thicknesses) -Continuous measurements of force and displacement -Solution: Modified Beam Theory (MBT) [Moll+10]

3.3.1 Performance of the micro-DCB 2.0 test system and its integration into the TXM

A load cell is a force-sensing module - a carefully designed metal structure with small elements called strain gauges, mounted at precisely defined locations to the structure. The load cell is designed to measure the applied force in one direction. The electrical signal output by the load cell is measured and amplified through the board- PhidgetBridge 4- Input (Phidgets Inc., Canada). The application of the load cell requires a calibration that is performed using data of known weights or forces and applying a subsequent linear interpolation. This standard calibration procedure is done as described in [Phi18]. The experimental studies of the temperature influence on the force measurements inside a nano-XCT are presented in the Appendix A2. The displacement calibration based on the evaluation of the system compliance from the measured force–displacement curves and described in Appendix A2.

3.3.2 Quantification of the energy release rate using force measurement

The design of the micro-DCB 2.0 allows to measure continuously the force – displacement data, which provides an advantage in data analysis and loading state control. The ASTM D5528-01 standard contains a data analysis method which we adapted to the available data for the micro-DCB 2.0 setup into a Modified Beam Theory (MBT). The MBT includes the following parameters: force F , load point displacement (deflection) $u(L)$,

crack length L , a calibration parameter δ and beam width b (Eq. 3.28). The calibration parameter δ is the effective delamination extension to correct for rotation of the DCB arms at the delamination front, which is usually very small. It is determined experimentally by generating a least-squares fit plot of the cube root of experimental compliance $C^{1/3}$ as a function of delamination length [Moll+10].

$$G_I = \frac{3Fu(L)}{2b(L+\delta)} \quad (3.28)$$

The micro-DCB 2.0 test configuration is the same as for the micro-DCB test, i.e. it is an asymmetric double cantilever beam test (mixture of fracture mode I and II). Therefore, the analytical procedures developed in the ASTM D5528-01 standard to calculate G_I for symmetric geometries are no longer valid and must be modified according to the boundary conditions of the micro-DCB experiment. Like for to the experiments and data analysis with micro-DCB (section 2.3.1), it is necessary to take into account the beam ratio e ($e = h_1/h_2$). Using the beam ratio e , the single beam deflections $u_{y_1}(L)$ and $u_{y_2}(L)$ at the ends of the single beams n , $n = \{1,2\}$ (same as Eq. 3.25 and 3.26), where the full crack opening Y equals to $u_{y_1}(L) + u_{y_2}(L)$, are determined. The energy release rate G determined from such asymmetric DCB experiments is a mixed G for mode I and II fracture, calculated by summing up from the results of each individual beam n , $n = \{1,2\}$. The calibration parameter δ was neglected for the data analysis in the proof-of-concept experiment since it is usually very small. With that, the equation for each of beam G_c becomes:

$$G_c = \sum_1^{n=2} \frac{3Fu_{y_n}(L)}{2bL} , \quad (3.29)$$

where F is the force, $u_{y_n}(L)$ the beam deflection for each beam $n = \{1,2\}$, L the maximum crack length, and b the beam width.

The force value F is calibrated as described above, with considering 1-hour temperature stabilization inside the nano-XCT tool (Appendix A2). The displacement (crack opening) Y at each loading state is calibrated according to the experimentally measured tool stiffness and due to an initial beam (crack) opening from the pre-cracking. The sample geometry (h_1 , h_2 and b) and the crack length L are measured directly from the X-ray radiographs.

3.4 Experimental validation of G_c determination on reference structures at micro-DCB tests

To better understand the measurement data and to calibrate the system for micro-DCB testers, serial experiments on reference samples with known properties were performed. The reference test structures are unpatterned interlayer dielectrics (ILD) layers with G_c of $3.5 - 5 \text{ J/m}^2$ (Figure 3.7a), deposited on silicon wafer. The reference test samples were made of two identical sample wafers bonded to each other and prepared on the same way as a usual micro-DCB sample (mechanical polishing, sawing [Nie15]) with dimensions of $50 \times 50 \times 1000 \text{ }\mu\text{m}^3$ to fit to the nano-XCT setting (FOV and energy range). The test geometry is shown in Figure 3.7 (a, b).

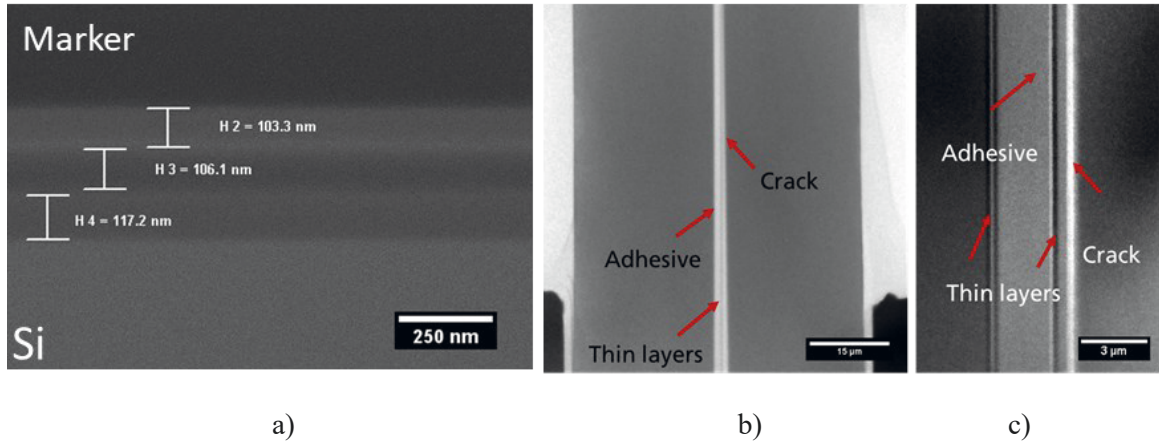


Figure 3.7: (a) Scanning electron microscopy (SEM) image of the reference structure: assumed a one ILD layer (H3) and two etch stop layers (H2, H4); micro-DCB test at nano-XCT: (b) Radiographs in standard resolution mode, stitched radiographs, (c): Radiograph at high resolution mode.

Micro-DCB test

The data analysis is based on the procedure reported in Chapter 3.2.1. The geometric parameters and fitting parameters (A , F) at different loading states (crack length L) for 5 tested samples are shown in the table below (Table 3.1). This table includes geometrical parameters of tested samples, measured from the radiographs: samples height h_1 (beam 1), h_2 (beam 2), beams ratio ($e = h_1/h_2$), crack length at certain loading state L and fitted geometrical parameters A_n and F_n for beam 1 and beam 2, as described in Appendix A1. The quantitative value of G for 5 samples with unpatterned structures listed in Table 3.1 is $G = 4.2 \pm 1.1 \text{ J/m}^2$,

according to Eq. 3.27. This result shows very good correlation with the given reference G for fracture mode I of the $G_I = 3.5$ to $5 J/m^2$.

Table 3.1 Geometrical parameters from micro-DCB experiments on reference test structures.

Sample	$L, \mu\text{m}$	e	A_1	F_1, mN	A_2	F_2, mN
1	440	0.78	0.62	71	0.83	-74
	632		0.63	-51	0.65	54
2	577	0.77	0.69	-39	0.83	26
	647		0.60	-46	0.54	45
	740		0.55	-33	0.54	35
3	410	0.78	0.51	41	0.97	-51
	465		0.66	35	1.00	-38
	580		0.63	37	0.99	-42
	766		0.67	33	1.00	-37
4	396	0.88	0.65	-37	0.70	37
	453		0.70	-29	0.68	30
	495		0.63	-38	0.63	40
5	406	0.93	0.99	-9	0.66	13
	420		0.90	-9	0.56	9

Micro-DCB 2.0 test

To calibrate and validate the entire micro-DCB 2.0 test, similarly to micro-DCB, 5 successive micro-DCB 2.0 measurements with geometric parameters in the Table 3. 2 were performed.

Table 3. 2: Geometrical parameters of tested samples for micro-DCB 2.0.

Sample #	$h_1, \mu\text{m}$	$h_2, \mu\text{m}$	e
1	25	30	0.83
2	24	36	0.67
3	21	34	0.63
4	26	39	0.67
5	31	33	0.94

The sequence of micro-DCB 2.0 tests at the reference samples were performed with displacement control as for micro-DCB, but with the advantage of continuous force

measurements. Diagrams of the measured forces versus crack length for 5 tested reference specimens are provided in Figure 3.8. In order to better understand the values of the output force during the micro-DCB 2.0 experiment an ideal diagram for a reference test sample based on the Eq.3.29 was calculated and plotted showing the expected curve shape (in black).

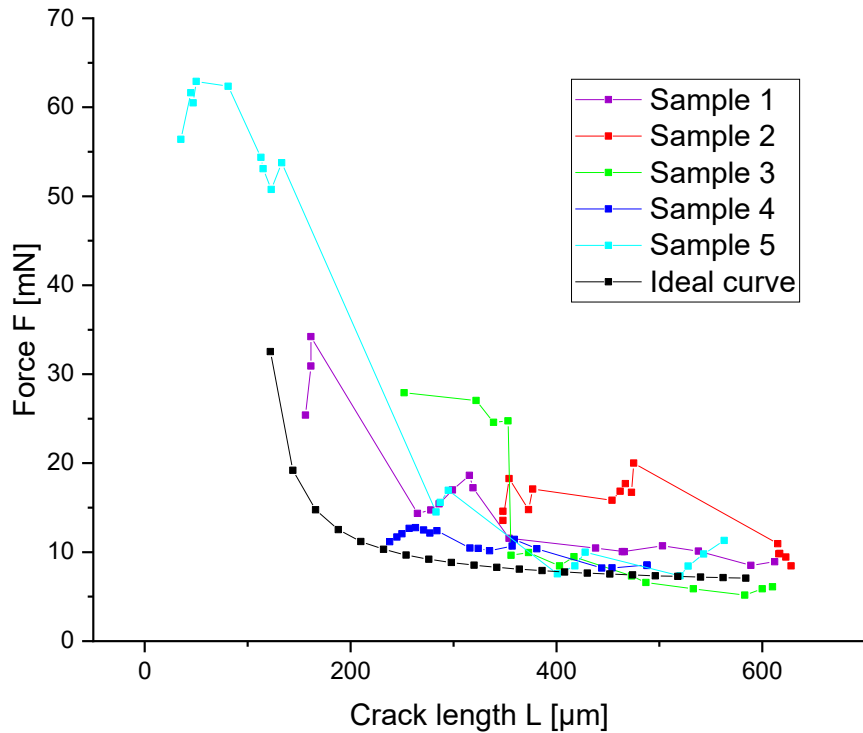


Figure 3.8: Force-crack length diagrams are based on 5 micro-DCB 2.0 experiments on reference samples and the ideal curve in black based on analytical solution (Eq. 3.29) with reference values of: $G = 4.0 \text{ J/m}^2$, $\epsilon = 1$ ($h_1 = h_2$), sample width $b = 50 \text{ } \mu\text{m}$. The initial crack length is $L = 100 \text{ } \mu\text{m}$ and displacement $Y = 0.1 \text{ } \mu\text{m}$.

The included force sensing capability allows the display of unexpected deviations in the force curve (peaks / troughs), which consequently can lead to an increase or decrease in the G values (Figure 3.9). There are uncertain events behind this behavior (see Figure 3.10 b) that can be described through the correlation of these achieved data and *in-situ* imaging. Such results are shown in Figure 3.9 in circles. In some cases, (e.g. sample #3) a high beam bending at very slow crack growth was observed, which may depend on the beams fixture parameter e.g geometrical parameter A (Chapter 3.2.1), which has not yet been fully described and need more investigations in the future. Other examples of uncertain experimental events, such as cracking in layers and cracks in silicon beams, are shown schematically in Figure 3.10.

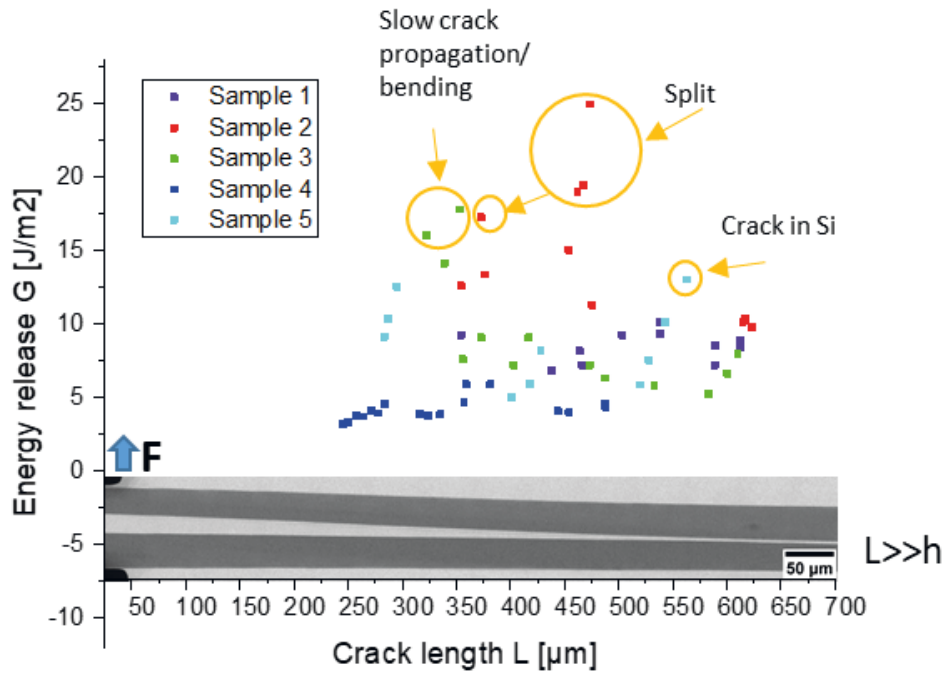


Figure 3.9: Plot of calculated G values over the crack length based on 5 micro-DCB 2.0 experiments on reference samples. The data in circles is described by the correlation of the images with a specific uncertain event in the micro-DCB experiment.

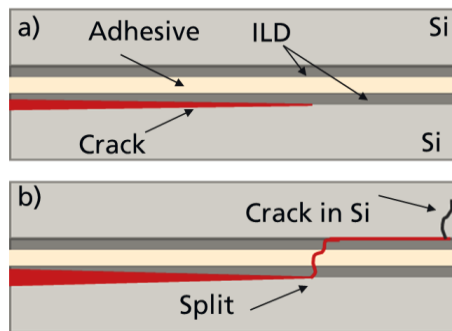


Figure 3.10: Scheme of the reference sample design: a) crack propagates between Si and/or ILD layers; b) crack splits at different interfaces and a crack at silicon beam. (crack propagation from the left to the right).

Finally, the resulting energy release rates G over the crack length without outliers (uncertain events) are presented in Figure 3.11. The length of the radiograph on the bottom and the crack length L (x-axis) are calibrated to visualize the crack length. In this proof-of-concept, the experimental value $G = 7.92 \pm 2.47 \text{ J/m}^2$ compared with the given G for fracture mode I $G_I = 3.5 \text{ to } 5 \text{ J/m}^2$ of the unpatterned reference samples. Differences are due to contribution of the mode mixity (sample geometry) and uncertain events. In addition,

calibration parameter δ , mode mixity and experimental conditions, for example humidity, affect the data.

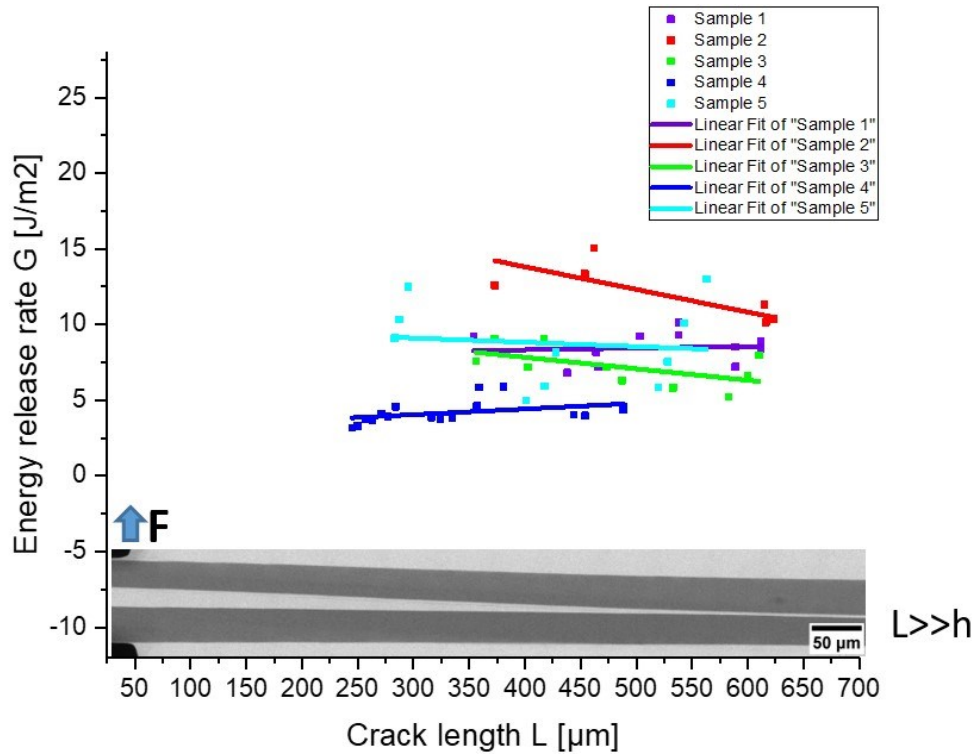


Figure 3.11: Plot of calculated G values over the crack length based on 5 micro-DCB 2.0 experiments on reference samples. The linear fit does not include outliers of certain events. The radiograph on the bottom and crack length L (x-axis) are calibrated to visualize the crack length.

4 Crack propagation imaging in patterned structures of microchips

4.1 Micro-DCB sample description

The object of this study are microprocessor chips and particularly its Cu/low-k BEO_L stack with guard ring (GR) structures, implemented on the rim of the die (Figure 4.1a). Depending on the technology node, GR have a different design in geometry, length, number of metallization layers. In this study, the particular BEO_L stack consists of 12 layers of *Cu* interconnects, the *Cu* interconnects are insulated by thin film materials with low dielectric permittivity (low-k/ULK materials) [Gri+14]. The crack stop structures are visualized in Figure 4.1b.

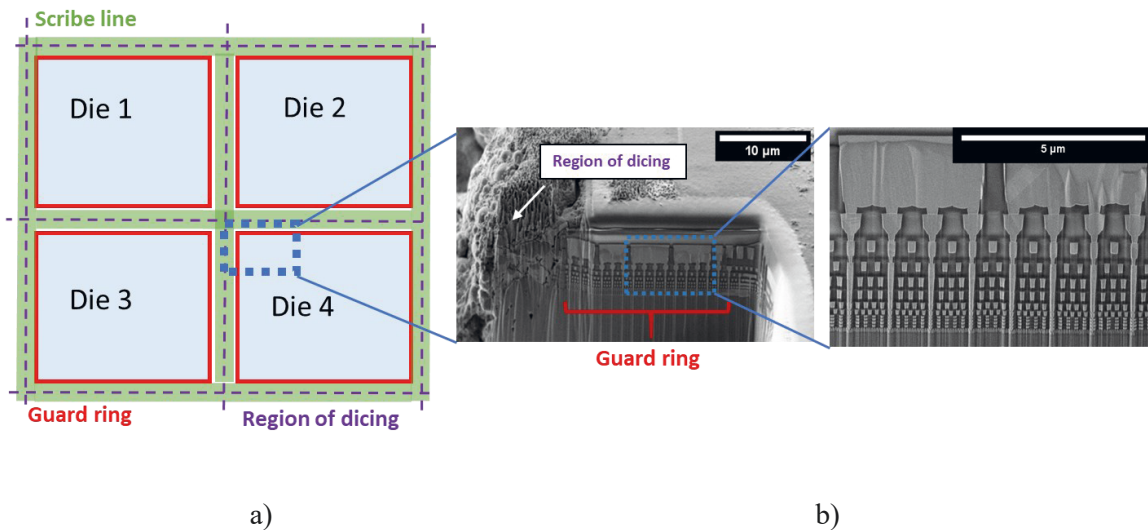


Figure 4.1: Scheme of the part of wafer with 4 dices, showing the dicing area, and SEM cross-section images with crack stop structures with 12 layers of *Cu* interconnects, for a microprocessor manufactured in 14 nm CMOS technology node.

The TEM image of a cross-section through a part of a GR structure is shown in Figure 4.2. The different grey values indicate the copper structures (dark) and different dielectrics used to isolate the metal structures and for the post passivation. The table with the thicknesses of single layer (metal plug layer *M0*, *Cu* metallization layers *M1* to *M12*, and post passivation layer *P*), based on the TEM image is shown in Table 4.1.

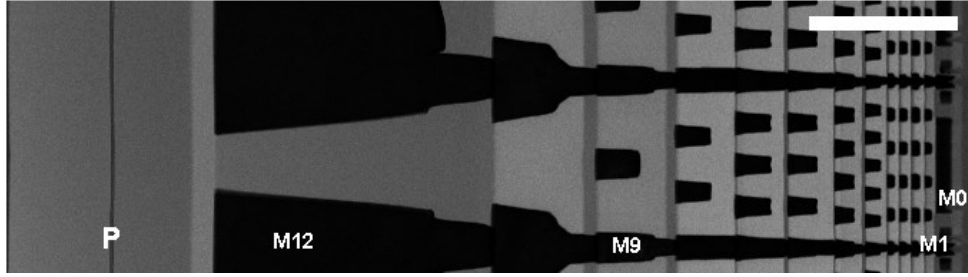


Figure 4.2: TEM image of a part of a GR structure with 12 metallization and a post passivation layer P , consisting of two sub-layers with different composition of the dielectrics. Scale bar is 1 micron. Image rotated by 90° in respect to Figure 4.1.

Table 4.1: Thicknesses of metallization layers based on TEM image.

Metal layer	P	M12	M11	M10	M9	M8	M7	M6	M5	M4	M3	M2	M1	M0
Thickness [μm]	1.37	2.02	0.72	0.54	0.42	0.38	0.35	0.20	0.15	0.08	0.08	0.08	0.08	0.13

The micro-DCB sample has a sandwich structure that consists of the original chip (thinned Si substrate and BEoL stack), a thin layer of epoxy (to glue the two beams together), and a dummy sample (thinned bare Si). For imaging the crack propagation within the sample using X-rays with 8 keV photon energy (Cu- $K\alpha$), the total sample thickness has to be in the range of 50 to 60 μm .

Table 4.2: X-ray attenuation length and transmission thickness at 8.05 keV of several materials [Hen93].

Material	Density [g/cm^3]	Attenuation length [μm]
SiO ₂	2.20	132.90
SiN	2.33	100.00
Si	2.30	70.80
Cu	8.96	22.30
Epoxy	1.50	1287.00
Low-k	1.14	309.00

A sample had to be prepared out of the wafer in the preparation procedure shown schematically in Figure 4.3. To characterize the GR structure under applied load, the wafer was sectioned to have scribe line and guard ring in the middle of the sample (Figure 4.3 a). A *dummy* silicon piece of wafer with corresponding size was glued by *Adhesive* (EpoTek 375, Epoxy Technology Inc., Billerica, MA, USA) on top of the patterned sample to form a sandwich structure in Figure 4.3 (b) side view. The micro-DCB samples includes the ROI - two guard ring structures (*GR1* and *GR2*) with scribe line (*SL*) in between as shown in Figure 4.3 (b). Curing of *Adhesive* was done on a heating plate at approximately 120 °C for two hours.

Afterwards the sandwich was sawed two times parallel to the scribe line, in Figure 4.3 (b) top view, to obtain a one millimeter wide stripe. Next, grinding from the wafer side was done manually using by *SiC* abrasive paper with a grit range from 500 till 4000 (RotoPol - 25, Struers ApS, Ballerup, Denmark). The progress of the grinding was monitored using a dial indicator and stopped at a final thickness of the wafer of 25 - 40 μm . Afterwards, a wafer saw DAD 321 (DISCO Corp., Tokyo, Japan) was used to precisely cut (Figure 4.3 (b) top view) stripes with a width of 50 μm . The sandwich was flipped over and glued to a grinding holder. Subsequently, the sandwich was grinded from the dummy side. The grinding progress was monitored using an optical microscope and stopped when individual columns were visible. Finally, the specimens were individualized by immersion in an acetone bath (Figure 4.3 (c)).

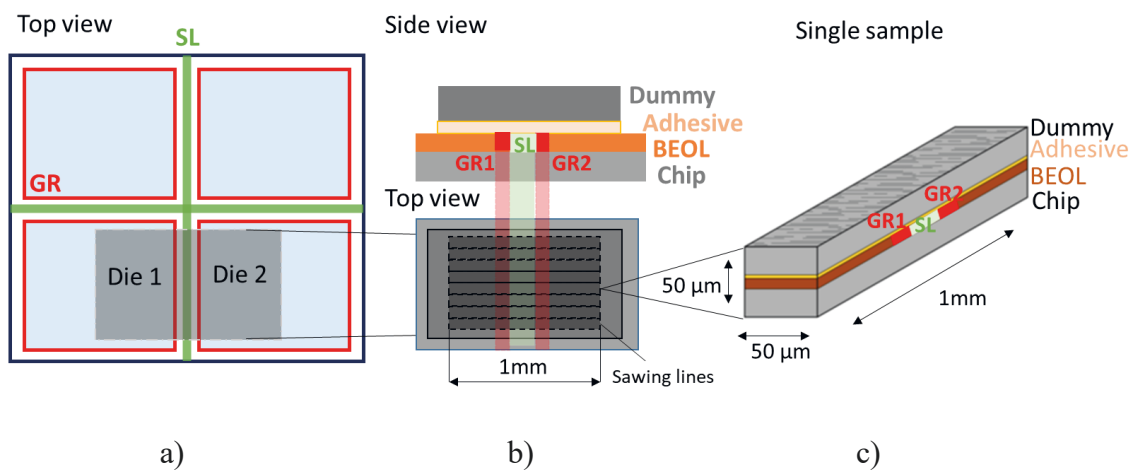


Figure 4.3: Scheme of the sample preparation procedure: (a) Scheme of the sample preparation procedure: (a) Top view of a centered dummy with fully processed dies, scribe lines and guard rings;(b) Side view of the sandwich structure after curing and top view after first step of grinding process, with the sawing lines in size of 1mm length, 50 μm width and ca. 80 μm depth; (c) sandwich sample after final step of grinding and acetone bath.

A notch has to be introduced into the sample to generate a defined starting point for the crack evolution in direction to ROI. Such sample design allows to investigate a crack path from the inner chip area to the *SL* through the failed *GRI*, and from the *SL* to *GR2*. In this thesis, the study is devoted to mimic the crack propagation from *SL* into *GR*, therefore the *ROI* includes *GR2* (Figure 4.4 b).

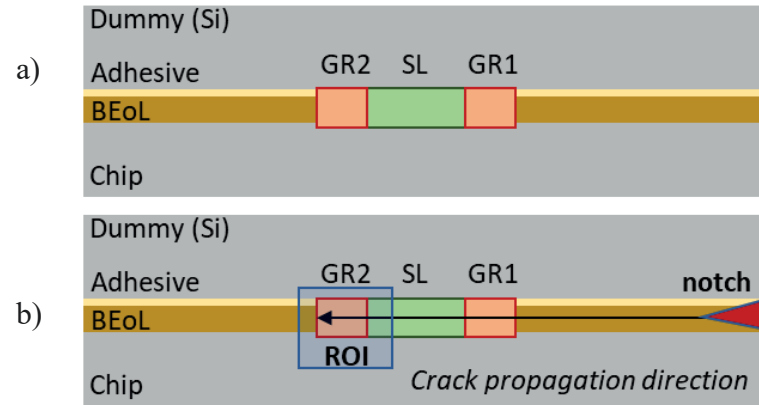


Figure 4.4: Sample design (a) sample geometry, (b) crack scheme.

The process of sample notching can be visualized using pre-alignment microscope (PAM) (Figure 4.5 b and c). To fabricate a notch with a sufficient depth for the micro-DCB experiment in the range 50 to 100 μm , the use of a razor blade turned out to be the method of choice [Nie15].

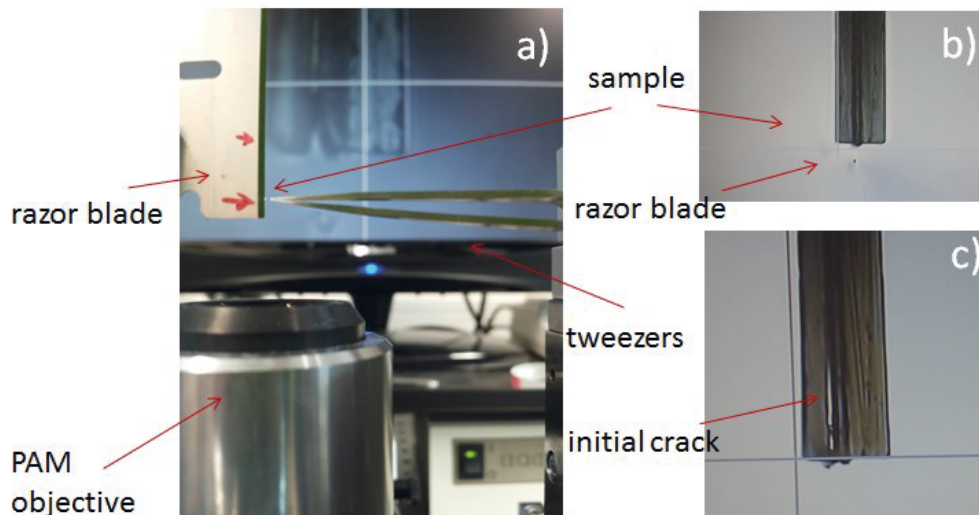


Figure 4.5: Photograph of the initial cracking at the PAM: a) Image of PAM set-up with razor blade aligned to the sample fixed in the tweezers; b) the beam is aligned to the razor blade (black dot) at the 50X objective magnification; c) crack initiation at the BEoL stack.

After notching, the sample was mounted perpendicular to the X-ray beam at the sample holders (two brackets) of the micro-DCB tester (see Figure 4.6). The sample fixation at the brackets position was carried out with small drops of super glue (Gorilla Glue, Inc., Cincinnati, OH, USA).

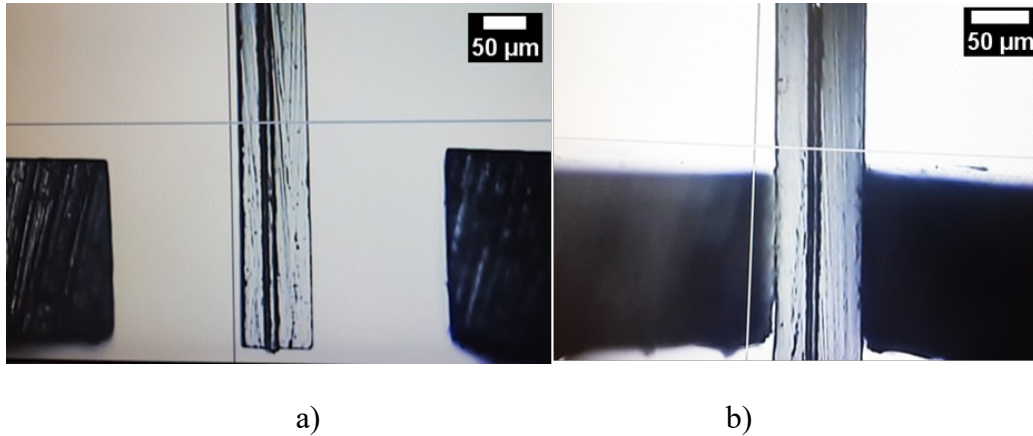


Figure 4.6: Photographs of the sample mounting to the micro-DCB tester at the PAM: a) sample alignment to brackets of the tester, brackets are open, b) fixed sample with the glue, brackets are closed.

The final step before the nano-XCT experiment is to attach a marker – e.g. a small spherical gold particle - onto the surface of the specimen at the ROI, which helps to find the focus and to perform the 3D reconstruction of the data [KN13].

4.2 Static loading – driving the crack to tough regions

4.2.1 *In-situ* radiography

The micro-DCB tests were performed displacement-controlled, i.e., one side of the sample holder was fixed and the other side was moved perpendicularly to the glue plane, stepwise (with a speed of loading of $1 \mu\text{m/s}$) to drive an initial crack in BEO_L structure. The sample was positioned in the TXM in such a way that the rotation axis (for tomography experiments) was located in the middle of the glue area vertically. The load was applied perpendicular to the rotational axis of the sample stage of the TXM, i.e. horizontally, to generate the crack propagation within the BEO_L stack, from the *SL* to the *GR2* structure, as illustrated in Figure 4.7 b. Due the interest to mimic the real microcrack (from outside (*SL*) to inside the chip) towards the *GR2*. The acquisition time per image was 15 s (camera binning 2), which allowed a stable operation of the experiment for one day. The applied load, estimated based on the geometry of the sample in case of micro-DCB and/or measured directly with

micro-DCB 2.0, was in the range of several tens of mN. For illustration, a SEM image of a FIB cross-section through the sample with the region of interest is shown in Figure 4.7 a too. The stitched radiograph (mosaic) of the micro-DCB sample is shown in Figure 4.7 c.

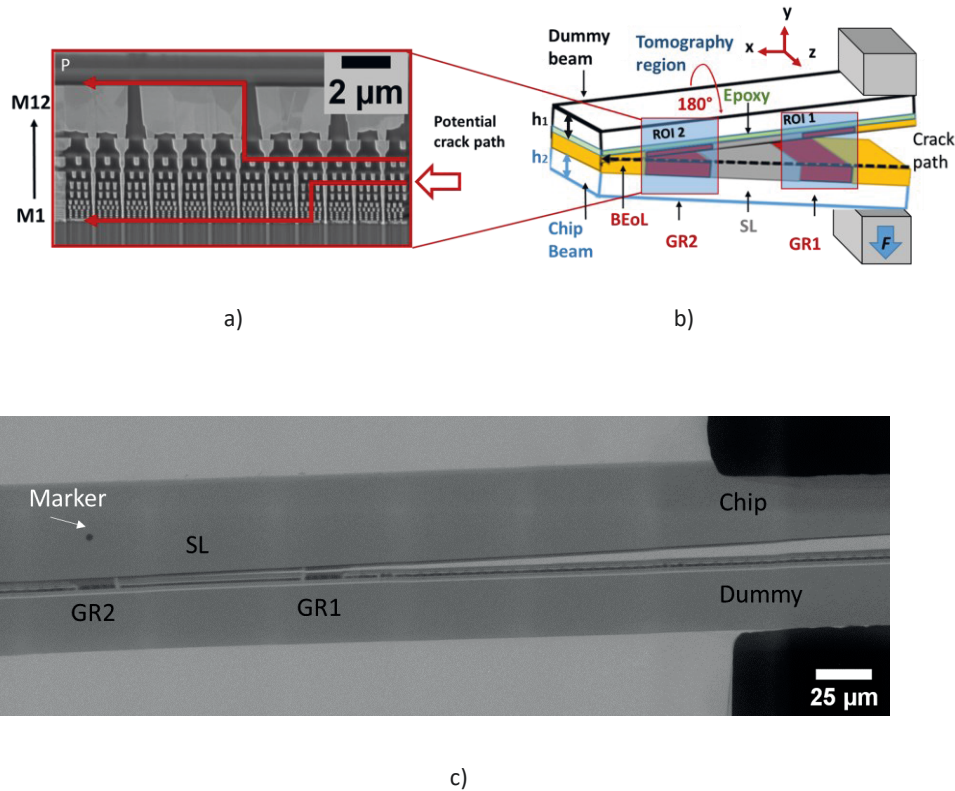


Figure 4.7: (a) SEM cross-section image of a GR structure with 12 metallization ($M1 - M12$) layers and a passivation layer on top, and two schemes for potential crack paths (red lines). The microcrack propagates from right to left. Mn refers to the n -th metallization layer, P to the post passivation layer; (b) Scheme of the micro-DCB test using a sandwich sample with the region of interest (ROI): Copper guard ring (GR) structure in the BEoL stack of a microchip; (c) Stitched radiograph (8x, 3y) of the micro-DCB sample inside TXM.

The micro-DCB test setup inside the TXM allows to follow the crack tip during sample loading and consequently a simultaneous acquisition of the radiographs of the sandwich sample while the micro-DCB test is performed. The displacement of the actuator was increased in steps of 100 to 50 nm until the crack reached the $GR2$ structure, and radiographs were acquired at each step (for constant displacement). That means, X-ray microscopy and tomography data of the BEoL structures can be collected while the displacement of the actuator was held at a certain position using closed-loop operation (steady state). Figure 4.8 shows a sequence of 2D radiographs of the crack tip for three different load steps, proving

that the crack stops at the *GR2* structure. Subsequently, the crack changes the layer and it propagates further.

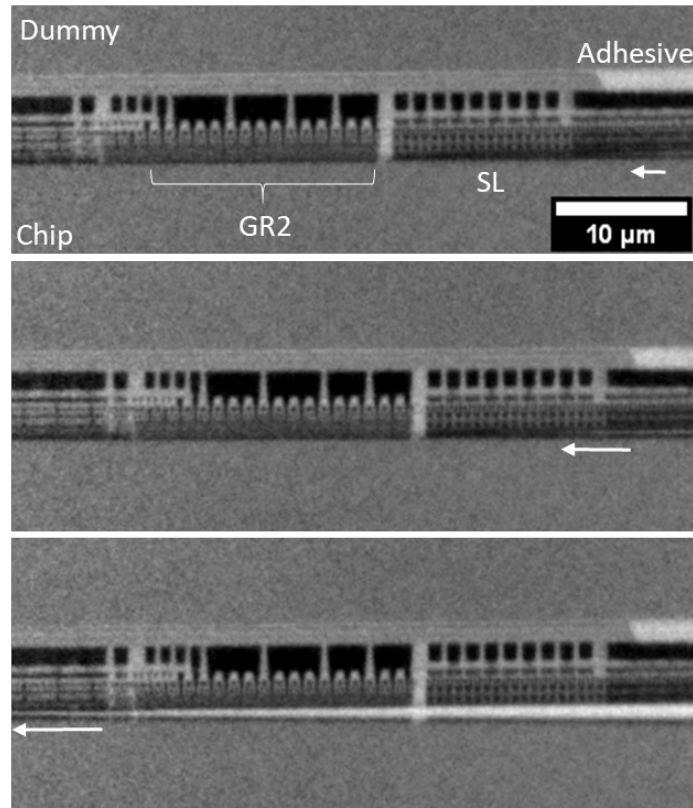


Figure 4.8: Radiographs of the micro-DCB sample with acquisition time per each of 15 seconds (*Dummy*, *Chip*, *GR2* - guard ring 2, *SL* - scribe line, *Adhesive*): crack tip towards the *GR2* (middle) and after passing the *GR2* (bottom). The middle and bottom radiographs were taken at the same displacement position.

For a quantitative determination of the energy release rate, based on the micro-DCB and micro-DCB 2.0 tests, radiographs at the crack tip position for all loading steps are required. Furthermore, in case of the micro-DCB tester, the acquisition of the stitched radiographs (mosaics) at certain displacement positions (steady state) is necessary to describe the boundary conditions for the beams (see section 3.2.2). Depending on the crack position, the mosaic consists of 21 (7x, 3y) to 33 (11x, 3y) single radiographs – exemplarily shown in Figure 4.7c.

4.2.2 Tomography

For tomography, the region of interest – *GR2* with a length of approx. 16 µm - was placed in the middle of the FOV of 65 µm at standard resolution, so that parts of the active

area of the microchip and the *SL* area are included in the FOV. Typical tomography settings that provide a sub-100 nm resolution are 801 projections with 90 s each in a 180 angular range, using camera binning 1 (1024 px x 1024 px). To reduce vertical and horizontal movements of the projections and to achieve a condition close to the ideal alignment of all projections, a sinusoidal movement of a spherical gold marker is assumed for the fitting, using imageJ [RAs13] software [KN13, Nie15]. The resulting offsets can be directly written to the original tomography file for the 3D reconstruction of the data. XMReconstructor 9.0 - standard software of the X-ray microscope, NanoXCT-100 (Xradia Inc., Pleasanton, CA, USA) - was used to perform the 3D reconstruction. An example of virtual cross-sections of the Cu/low-k stack with a *GR2* structure for several stages of the micro-DCB test with gradually increased load is visualized in Figure 4.9 [Kut+17].

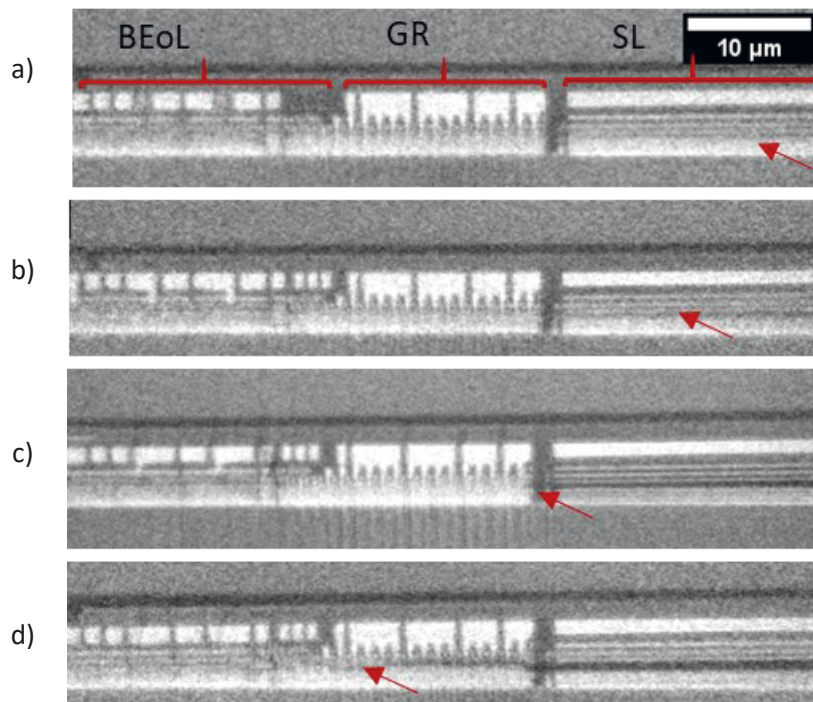


Figure 4.9: XY Virtual cross-sections through the Cu/low-k BEoL stack at several stages of the micro-DCB test, based on nano-XCT data [Kut+17]. The virtual cross-sections are based on four tomography datasets at several states of the crack propagation from the right to the left. Crack openings at the end of the beams and the crack lengths in μm are: a) 11.3/410, b) 11.8/ 425, c) 15.85/432, and d) 16.0/442. The values of crack opening are different from the displacement values from the actuator (max. 13.7 μm) because of the initial crack opening of several micrometers.

These cross-section images, taken from nano-XCT data at several load steps, allow one to track the crack path through the whole BEoL structure. The crack propagated from the

scribe line horizontally along weak interfaces (adhesive failure) or within interlayer dielectrics (cohesive failure) of the BEOl stack in the direction of the *GR2* structure (from right to the left). Subsequently, the crack propagated into another layer in the *GR2* structure. Eventually, the crack propagated into the active chip region. Eventually, the crack propagated into the active chip region. The delaminated area at the *SL* is shown dark in Figure 4.10 (a) and (b), as well as in *GR2* and at the beginning of the active area of the chip (BEOl) in Figure 4.10 (b). Virtual sections show the redirection of crack paths through the metallization layers at *GR2* in more detail in Figure 4.10 (c).

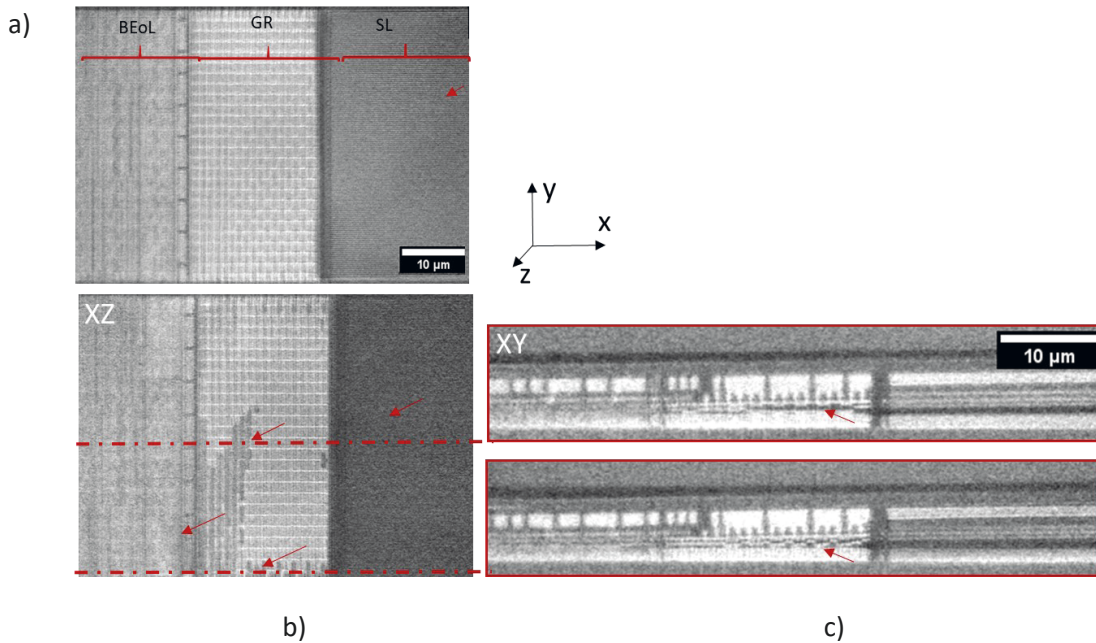


Figure 4.10: (a) and (b) XZ Virtual cross-sections through the Cu/low-k BEOl stack corresponding to loading position in Figure 4.9 (b) and (d), respectively. Two respective XY cross-section at the red lines position in (b), showing multiple cracking at GR2 (c).

4.2.3 3D data analysis

The 3D tomography data allow to evaluate the number of the damaged metallization layer (location in the metallization stack). A virtual plane view showing the crack propagation in the Cu/low- k BEOl interconnect stack, based on non-destructively acquired nano-XCT data, is provided in Figure 4.11. The vertical dark lines in Figure 4.11 (a) are dielectrics which absorb less X-ray photons than metals. The medium-dark irregular region in Figure 4.11 visualizes the delaminated area above metallization layer *M8*. *Post mortem* SEM inspection of the fracture surface (Figure 4.11) confirms the crack in the metallization layer as determined

based on nano-XCT data, and it is a prove of the applicability of the approach described in this thesis. Both the virtual plane view based on nano-XCT data and the SEM image of the fracture surface show the crack front very clearly. The data analysis is based on the reconstructed tomography data, and further processing using the software packet *ImageJ*. To extract the location of the crack at the sample, an image analysis script was developed (Appendix C). The result is shown in Figure 4.11 a.

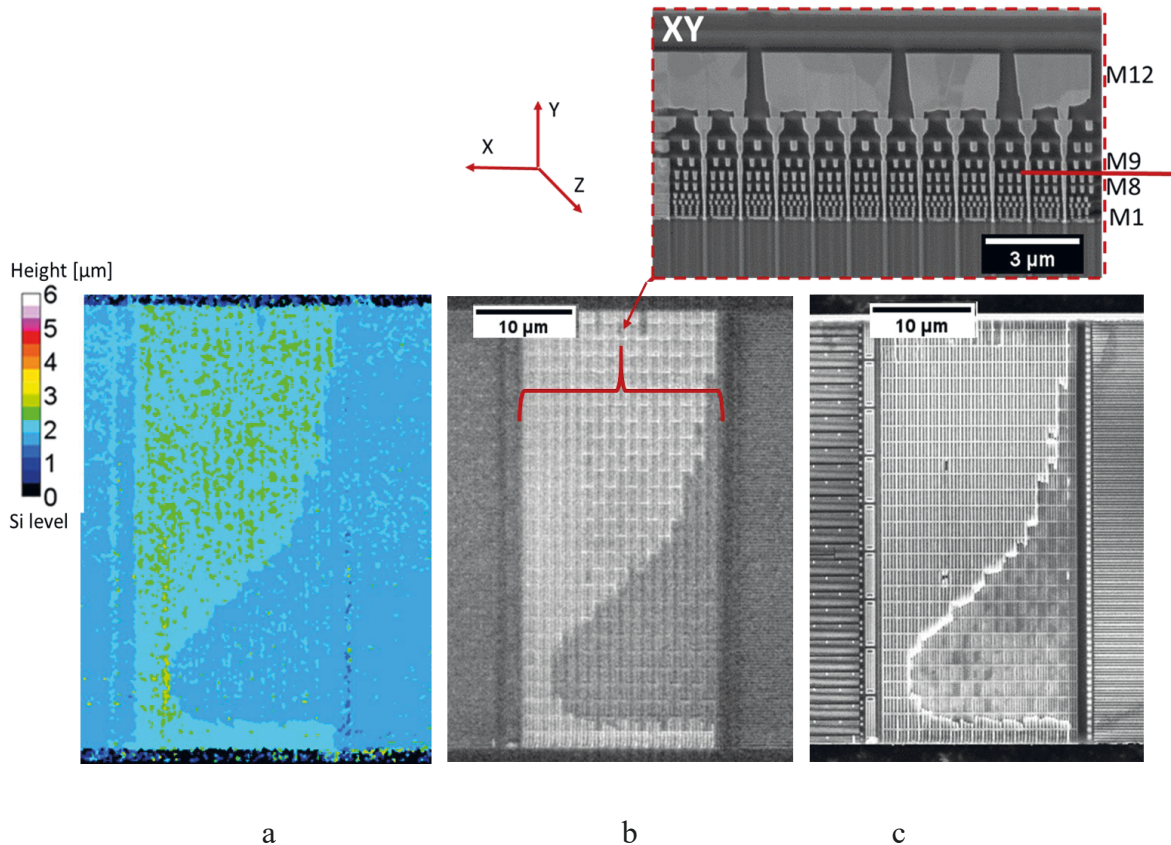


Figure 4.11: Representation of the crack path (from right to left) between metallization layers: a) Result of the image analysis script to detect the location of the crack. Shown is the XZ scan with the height (in μm) above the silicon substrate indicated as color b) Virtual plane view (above metallization layer 8, *M8*) showing the crack propagation in the Cu/low-k BEoL interconnect stack, based on the reconstructed nano-XCT data. c) *Post mortem* SEM image of the fracture surface. Upper image: SEM image of a FIB cross-section with a red line indicating the crack position.

The analysis allows to detect the height of the crack above the silicon substrate. With the knowledge of the thickness of the metallization layers (Table 4.1), the height can be translated into a metallization layer number. In the example shown in Figure 4.11 (a) the crack propagated above metallization layer *M8*.

SEM images of the fracture surface that were acquired *post mortem* (Figure 4.11 c) clearly show the microcrack propagating above metallization layers *M10* to *M8*, from scribe line to *GR2*. These SEM images confirm the results obtained by X-ray tomography.

Based on the height map derived from the tomography data using ImageJ software it is possible to calculate the percentage of fractured area of each metallization layer. One example of such data analysis, there is the crack propagated in lower metallization layers shown in Image Figure 4.12 (a, b). This result achieved with image analysis script as height map, that can be correlated to individual metallization layers by knowing the height of the individual layer (as explained above). By setting a threshold one can visualize the amount of fractured area for each metallization layer as shown in Figure 4.12 c.

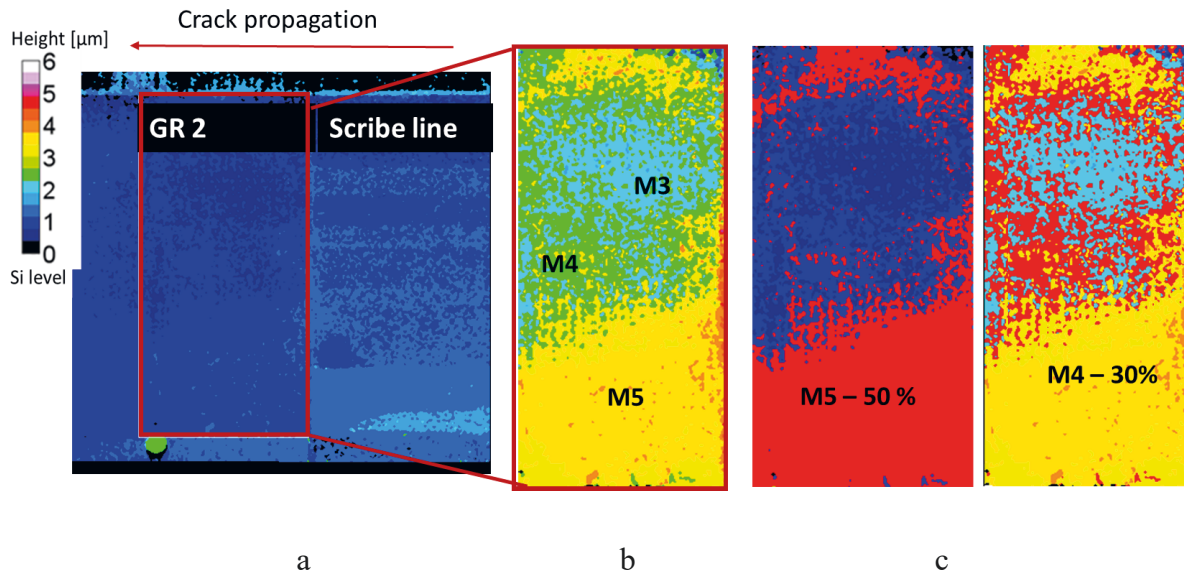


Figure 4.12: Example of the data analysis: a) Height map based on the tomography data 16-bit image; b) Zoom in of the GR region 32-bit; c) thresholding of the image (b) for single layer investigation according to height map: Red color indicate M5 (50%) and yellow color indicate M4 (30%).

4.3 High resolution imaging at nano-XCT

The nano-XCT tool provides switchable pixel size and FOV configurations of 65 nm at 67 μm x 67 μm (standard resolution mode, SR) and 16 nm at 16.5 μm x 16.5 μm (high resolution mode, HR) with 200x and 800x total magnification), respectively.

The micro-DCB and micro-DCB 2.0 test stages fit to the nano-XCT for both imaging modes. The previously reported experiments were performed in SR mode due to the larger

FOV, which provides a more efficient 3D data set (volume) of fractured layers from *SL*, *GR* and microchip (*BEoL*) regions. However, HR studies of detailed crack propagation during micro-DCB tests at the GR are possible. The stitched radiograph at HR mode is presented in Figure 4.13.

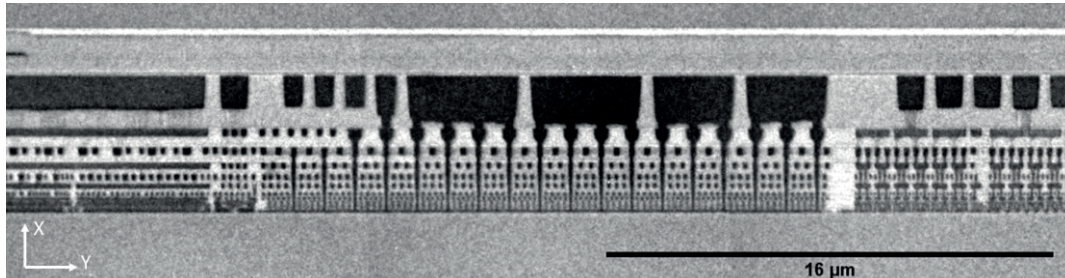


Figure 4.13 Stitched radiograph of the GR structure at HR with FOV of $16\ \mu\text{m}$ ($1x,3y$) of unloaded sample.

The micro-DCB experiment in HR mode, based on the quantitative data analysis described in section 3.2.2, requires an extremely long data acquisition time. Therefore, the developed micro-DCB 2.0 experiment with a force sensor and the resulting reduced efforts for data analysis is more suitable for this HR study. The micro-DCB experiment on the sample with beam ratio $e = 1.2$ was performed at HR mode for detailed crack propagation in 2D. The tomography data were collected in SR mode. Two stitched radiographs taken in SR and HR modes are shown in the Figure 4.4.

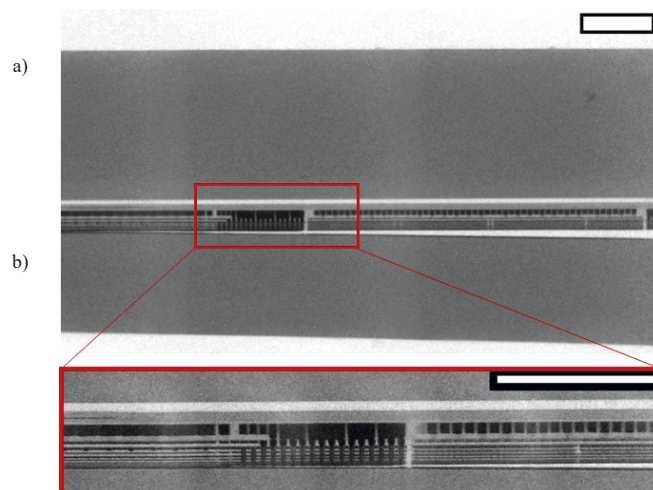


Figure 4.14: Stitched radiographs at SR mode (a) and HR mode (b) at the final step of experiment. Scale bar $16\ \mu\text{m}$. Beam ratio of dummy to chip $e = 33\ \mu\text{m} / 28\ \mu\text{m} = 1.2$.

A sequence of radiographs of the crack propagation from *SL* to *GR 2* taken during a micro-DCB test using the micro-DCB 2.0 tester at HR imaging mode is shown in

Figure 4.15 (a-c). During the micro-DCB experiment the measured force reached a maximum of 15.5 mN and fast drop was observed at the point of guard ring cracking. A diagram of the force evolution at the moment of crack propagation through *GR2* (from the *SL* towards the *GR2*) according the radiographs in Figure 4.15 (a-c) is presented in Figure 4.15 d.

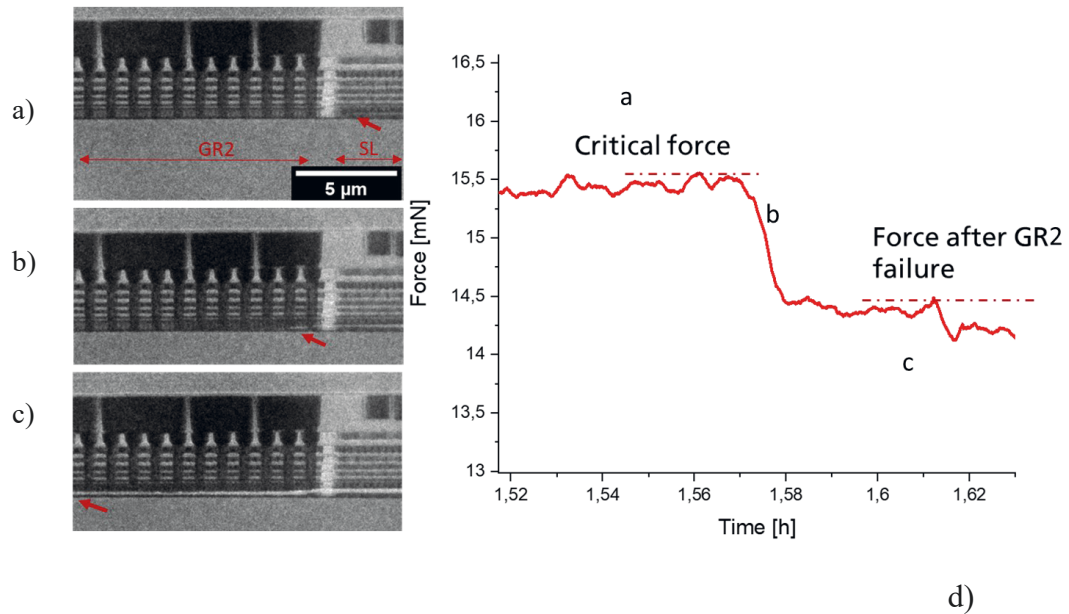


Figure 4.15: Series of radiographs taken at HR of a micro-DCB sample with a beam ratio $e = 1.2$: a) crack in *SL* toward *GR2* at *M4*, b) crack starts to penetrate *GR2*, c) crack passed *GR2* down to *M2*. Force-time plot for micro-DCB 2.0 experiment indicates the critical force of 15.5 mN at position (a) dropping down to 14.5 mN at position (c) Figure 4.14.

The high-resolution study of the crack propagation using the micro-DCB 2.0 setup allows to visualize fracture of the Cu/low-k stack locally and to detect crack the tip position at a certain loading state more precisely. The data recorded during the test enable a comprehensive analysis of the GR fracture behavior.

Complimentary to this study, a high-resolution micromechanical X-ray microscopy experiment at GR structures was performed at a synchrotron radiation beamline. The experiment and the results are presented in Chapter 5.

5 Complimentary study- *in-situ* synchrotron soft X-ray microscopy of the BEOl structure

5.1 Micromechanical test at a synchrotron radiation based TXM

This chapter describes the application of synchrotron-radiation based X-ray microscopy for *in-situ* crack detection and study of crack evolution kinetics in microchips with a spatial resolution 25 nm.

The experiments at the U41-TXM beamline at the synchrotron radiation source BESSY II at Helmholtz Zentrum Berlin, Germany, were complimentary performed experiments. Table 5.1 compares photon energy, sample thickness and resolution for laboratory-based X-ray microscopes using Cu-K α radiation and synchrotron beamline microscopes operated at low photon energies. The application of an indenter manipulator at the TXM beamline of the synchrotron radiation source BESSY II provides an unprecedented level of details on the fracture behavior of microchips.

Table 5.1: Comparison of laboratory-based and synchrotron-based set-ups.

Parameter Set-up	X-ray Energy	Resolution	Sample thickness	Manipulator
Lab Nano-XCT	8 keV	130 - 50 nm	~ 50 μ m	Micro-DCB test
U41- TXM	< 2 keV	25 -12 nm	~ 2,5 μ m	Modified PI95

The crack propagation in Cu/low-k BEOl stacks of microchips was visualized *in-situ* using an experimental setup which combines high-resolution X-ray imaging with mechanical loading. The full-field transmission X-ray microscope at the U41-TXM beamline of the synchrotron radiation source BESSY II (see Figure 5.1) is operated in the photon energy range between 270 eV and 2500 eV. A detailed description of the microscope can be found

in [Sch+12]. For the experiments, a photon energy of 1200 eV was used. Lamella samples with the region of interest (BEoL stack of the microchip with crack stop structures) were thinned to a thickness up to 2.5 μm using the focused ion beam (FIB) technique. The chosen photon energy provides high absorption contrast. The spatial resolution of the TXM was about 25 nm in this study, which allowed to image all *Cu* interconnect structures in microchips manufactured in 14 nm CMOS technology nodes. The mechanical manipulation of the samples was performed using a Picoindenter PI95 (Hysitron/Bruker) (Figure 5.2 a), equipped with a tungsten wedge indenter (Figure 5.2b). During the TXM imaging, the wedge was indented into the BEoL stack to initiate and to propagate a crack.

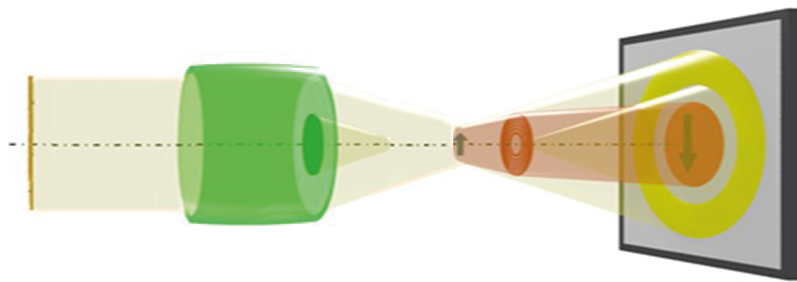


Figure 5.1: Optical set-up of the full-field transmission X-ray microscope: Monochromatized synchrotron radiation, condenser with central stop, sample with mechanical test setup, Fresnel zone plate, CCD detector.



Figure 5.2: (a) Mechanical manipulator (Picoindenter PI95, Bruker Corporation); (b) Scheme of the indentation of the BEoL stack using a tungsten wedge.

The Hysitron PI 95 TEM PicoIndenter is designed for depth-sensing indentation and allows direct-observation nanomechanical testing inside a transmission electron microscope (TEM). This holder is also compatible to the JEOL, ThermoFischer, Hitachi, and Zeiss microscopes. The HZB-TXM sample stage is a modified FEI Compustage which allows to use PI95 TEM holder for the micromechanical experiments. To be able to provide enough force and displacement to drive a crack in the BEoL stack, an additional piezo actuator was

implemented into the set-up. With this, the force was increased from 1 mN up to 10 mN, and the travelling range from ca. 3.5 μm to 15 μm . The designed connection from the PI95 transducer through the new piezo actuator to the wedge tip is shown in Figure 5.3. A special tungsten (tungsten on *Si* substrate) wedge tip with sharp curvature was prepared by FIB milling (Figure 5.4).

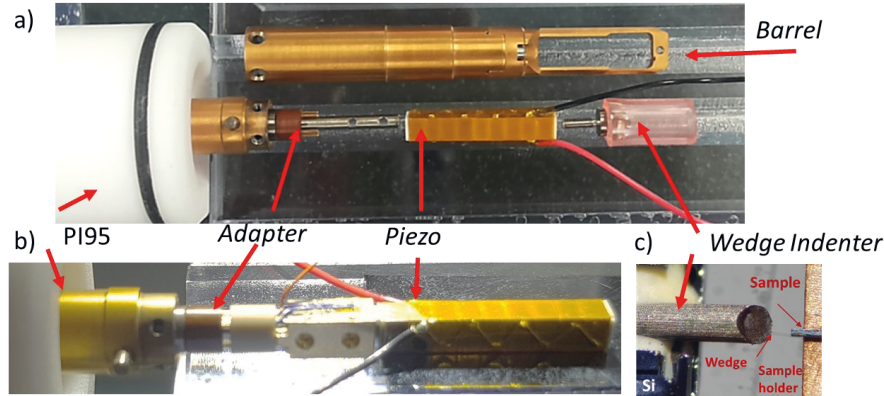


Figure 5.3: The modifications in the set-up of PI95 (a) designed and (b) built. The scheme of the indenter and sample position is shown in (c).

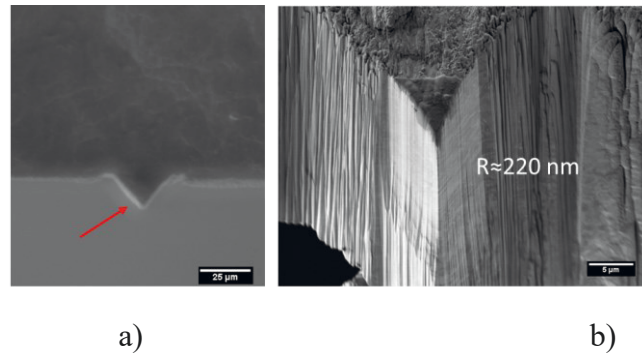


Figure 5.4: (a) SEM image (top view) of the wedge indenter; (b) tip curvature with radius of ca. 220 nm.

5.2 High-resolution *in-situ* soft X-ray microscopy

The samples were prepared in such a way that the tungsten wedge indenter could be applied to initiate the crack, and by increasing the load to propagate the crack. Figure 5.5 shows a scanning electron microscopy (SEM) cross-section image with GR structure of a microchip. The initial crack (12 μm length and 225 nm width) prepared by FIB milling was positioned at the cross-sectioned BEoL structure (scribe line position) towards the crack stop structure between metal layer *M8* and metal layer *M9* (see Figure 5.5 b).

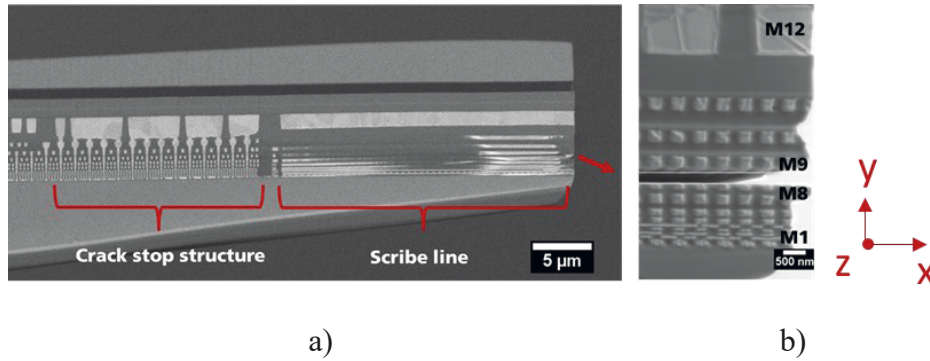


Figure 5.5: (a) SEM image of a cross-section with crack stop structures of a microchip with 12 layers of Cu interconnects. (b) SEM image of the initial crack (12 μm length and 225 nm width) prepared by FIB milling that is positioned between metal layer M8 and metal layer M9. Sample thickness in z direction 2.5 μm .

Figure 5.6 demonstrates the sequence of crack propagation. The initial crack (small notch) was introduced into the cross-sectioned sample, particularly at the scribe line position, which is the location where the micro-cracks can be initiated during the wafer dicing process (Figure 5.6 a). This notch provides a defined starting point for the crack evolution. If the subsequent stable crack propagation in the BEoL stack occurs in a controlled way, it allows to determine the pathway of the crack along weak interfaces (adhesive failure) or within the soft dielectrics (cohesive failures). Figure 5.6 b shows the further propagated crack which is stopped in front of the crack stop structure above *M8*. Subsequently, the crack propagates between metal layer *M8* and metal layer *M7*, and finally, it is directed to metal layer *M4* (Figure 5.6 c).

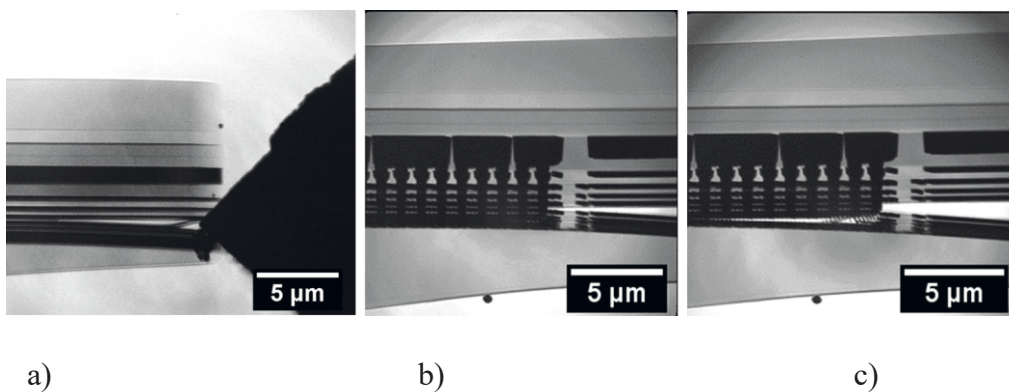


Figure 5.6: (a) The tungsten wedge indenter is initiating the crack from in the scribe line (toward the crack stop). (b) The crack is stopped in front of the crack stop structure, then it propagated down at metal 8. (c) The crack propagates between metal *M8* and metal *M7* and is then directed to metal *M4*.

Another example in Figure 5.7 demonstrates the sequence of crack propagation in the sample with different design of the *SL*. The initial crack introduced at the scribe line position between metal layer *M6* and *M7* was driven toward the *GR* structure where its stopped (Figure 5.7 a). With further increasing force to the tungsten tip the crack propagates through metal layers *M7* and *M8*, and finally, it is directed above layer *M9* (Figure 5.7 b).

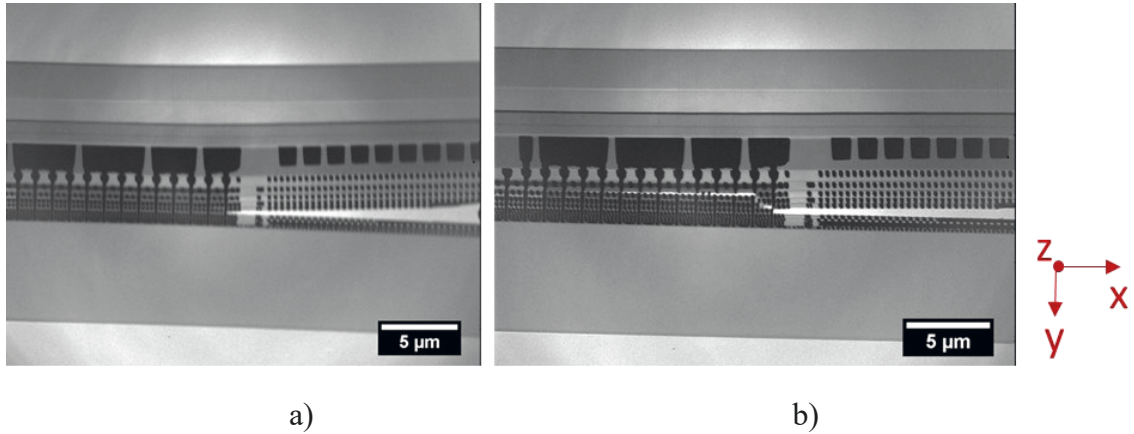


Figure 5.7: (a) The tungsten wedge indenter is initiating the crack from in the scribe line (toward the GR). (b) The crack propagates between *M6* and *M7* and is then directed above *M9*. The mounting of the sample is flipped vertically for the better visualization. The sample thickness in *z* direction is 2.2 μm . Energy range: 1200 eV, exposure time 2s/image.

These *in-situ* experiments allow to identify weak layers and interfaces in BEoL stacks of microchips and to evaluate the robustness of the BEoL stack against CPI. It provides detailed information on the fracture behavior with a spatial resolution of 25 nm.

5.3 Nano X-ray tomography

The tomography of the tested sample in Figure 5.7 was performed at the BESSY TXM at a photon energy of 1200 eV. The tilt angle was from -60° to $+60^\circ$, with 1° angle step, the exposure time per image was 2 s. The achieved pixel size is 18.4 nm. Several software packages were used for reconstruction: Tomo3D based on weighted back projection (WBP) and simultaneous iterative reconstruction method (SIRT) [AF11] and hybrid developed software with elements of deep learning algorithms (DLA) [Top+20] (Figure 5.8). Figure 5.8 (a, b) show virtual cross sections obtained with Tomo3D (within a few minutes. The more advanced reconstruction with DLA (Figure 5.8 c) is characterized by less noise and better contrast. With both data analysis approaches, broken Cu / low-k interfaces were identified.

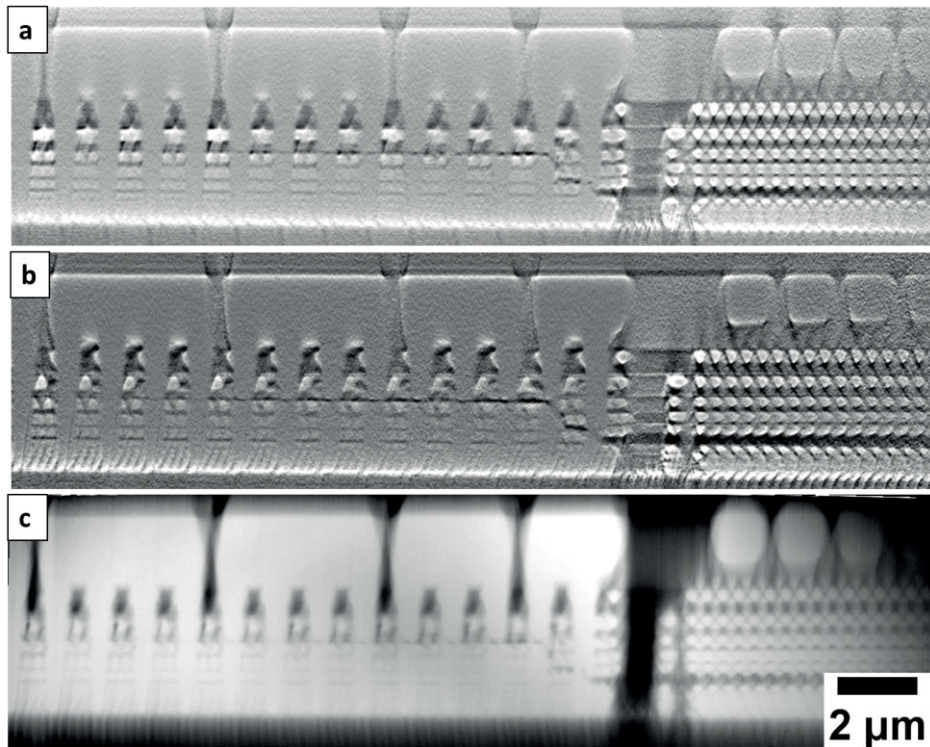


Figure 5.8: Synchrotron-based nano-XCT reconstructed data of sample (Figure 5.7) after experiment (a) WBP, (b) WBP+SIRT (10 iterations), (c) Hybrid reconstruction algorithm [Top+20].

The combination of high-resolution X-ray imaging with *in-situ* mechanical testing, here the application of a specially designed indenter manipulator in a transmission X-ray microscope at a synchrotron radiation source beamline, provides an unprecedented level of details on the fracture behavior of microchips. The pathways of microcracks, and consequently the weakest structures for cracking, were identified in fully integrated, realistic multilevel Cu/low-k interconnect structures of microchips manufactured in advanced technology nodes. The change of the crack direction in front of a crack stop structure provides information about the effectiveness of the design these dense metal structures. Compared to laboratory TXM studies, the main advantage of the synchrotron-based TXM experiment at photon energies < 3 keV is the better spatial resolution: 11 nm resolution have been demonstrated for the full-field transmission X-ray microscope at the U41-TXM beamline of BESSY II [Reh+12]. Currently, the typical resolution of laboratory TXM tools, commonly operated at 8 keV photon energy (Cu-K α radiation), is 50 nm [Kut+18c]. This resolution is not sufficient to distinguish clearly between cohesive and adhesive fracture, particularly for interconnect structures at low metallization layers of microchips manufactured in 14 nm CMOS technology nodes.

In summary, the application of the novel, specially designed indenter manipulator in the transmission X-ray microscope at BESSY II allows the (*in-situ*) visualization of crack opening and propagation in Cu/low-k interconnect stacks, and to distinguish clearly between adhesive and cohesive failure in Cu/low-k interconnect stacks of microchips. These studies provide complementary data regarding the robustness of BEoL stacks against CPI and for the evaluation of the effectiveness of crack stop structures.

6 Discussion of the experimental results

In this chapter the validation of methodology for determination of the critical energy release rate (G_c) in patterned structures in fully integrated multilevel interconnect structures of a microchip by using a miniaturized micro double cantilever beam (micro-DCB) tests in a high-resolution laboratory X-ray microscope is presented. Experimental results, main observations and achievements of non-destructive 3D visualization and localization of the crack path in a GR structure with a resolution of less than 100 nm are interpreted and discussed.

6.1 Determination of local G_c of BEoL stacks

All three regions (SL , GR , $BEoL$) of the thinned wafer piece were manufactured using the Cu dual damascene process [Lit+03], with organosilicate glass as insulating dielectrics between the Cu interconnects. For unpatterned porous low-k thin film materials as used in 14 nm CMOS technology node, G_c values in the range of 2 – 5 J/m² were reported [PWK18, Chu+09, Li+13], i.e. the fracture toughness of these materials is low. Compared to this G_c value for unpatterned OSG thin films, the G_c value is increased for patterned Cu/ low- k structures. It depends on the Young's modulus - and consequently on the critical energy release rate G_c as a measure for the fracture toughness - of the dielectrics as well as on the design of copper structures in the SL , GR and $BEoL$ stack regions of the studied wafer piece. Since the dielectrics is identically for each level of the (patterned) layer stack, the differences of the G_c values of different regions (SL , GR , $BEoL$) have to be explained with the design of the Cu structures.

In this section, the critical energy release rate for crack propagation G_c of different regions of a processed silicon wafer with fully integrated multilevel interconnect structures of a microchip (SL , GR , $BEoL$) are determined quantitatively, and the design-caused increase of the G_c value, e.g. the role of GRs, is discussed. The geometry of the microcrack is measured at several loading steps during the micro-DCB test together with a data analysis based on the linear elastic fracture mechanics and the Euler-Bernoulli beam model. The combination of a displacement-controlled crack propagation through different regions of a thinned wafer piece, particularly the on-chip interconnect stack, and at the same time imaging of the crack allows to determine the local critical energy release rate G_c for crack propagation in these regions quantitatively.

The load enforced in the micro-DCB test in the range of several tens of milli-Newtons was applied perpendicular to the rotational axis of the sample stage of the TXM. As a result, the crack length was growing with increasing crack opening in the *SL* (see Figure 6.1 a). In this particular example, the beam thickness ratio is approximately 1.3:1. The crack growth rate was progressively reduced when the crack approached the guard ring, and it stopped propagating when it reached the *GR2* (at a crack length of 332 μm for the sample shown in Figure 6.1 a). No crack propagation occurred during the increase of the crack opening from 10.8 μm to 12.1 μm . Only when the applied force, and consequently the crack opening (and beam displacement), was large enough, the crack propagated through the *GR2* structure. The critical energy release rate G_c for crack propagation was calculated at each loading step, considering geometrical and materials parameters of the studied sample as well as F and A from the fitting procedure described in Appendix A1.

Figure 6.1 b visualizes quantitative G_c values in the *SL* and in the *GR*. The first 6 data points in Figure 6.1 b belong to the *SL* region at crack lengths from 290 to 316 μm . The calculated G_c value for this region is determined using the 3 values that form a plateau, resulting in $8.8 \pm 0.5 \text{ J/m}^2$ (statistical error). Then, the G_c value is progressively increasing until it reaches its maximum value of 34.8 J/m^2 . This is the critical energy release rate G_c of the *GR2* structure. After penetrating the *GR2*, G_c is dropping down to 6 J/m^2 in the *BEoL* structure of the microchip (measured at a crack length of 440 μm).

The critical energy release rate G_c of different regions of the thinned wafer piece (*SL*, *GR2* and *BEoL* stack) were determined applying a unique experimental setup, a micro-DCB test integrated into a laboratory X-ray microscope, and subsequent data analysis using the Euler-Bernoulli beam model described in 3.2.2. The values for scribe line, guard ring and *BEoL* stack, are about 9 J/m^2 , 35 J/m^2 and 6 J/m^2 , respectively.

Once the crack tip reaches the *GR2*, it is stopped completely by the *GR2* that is made of primarily copper with a thin diffusion barrier. The ductility of *Cu* helps blunt the crack tip and provides toughness to retard crack propagation. The crack tip opening increases sharply and the strain energy builds up while the crack length remains constant. When the crack tip opening increases to 12.1 μm , the energy release rate reaches the critical value of 35 J/m^2 , at which catastrophic failure of the *GR2* occurs. This critical energy release rate provides a measure of fracture resistance of the *GR2* structure against inward crack propagation. It is significantly higher than the respective value in the *SL* and in the *BEoL* stack. We note that the mechanics model developed in this study accounts for the geometric imperfection of the

sample and the specific clamping boundary condition of the micro-DCB specimen due to the finite sample length relative to the clamping part.

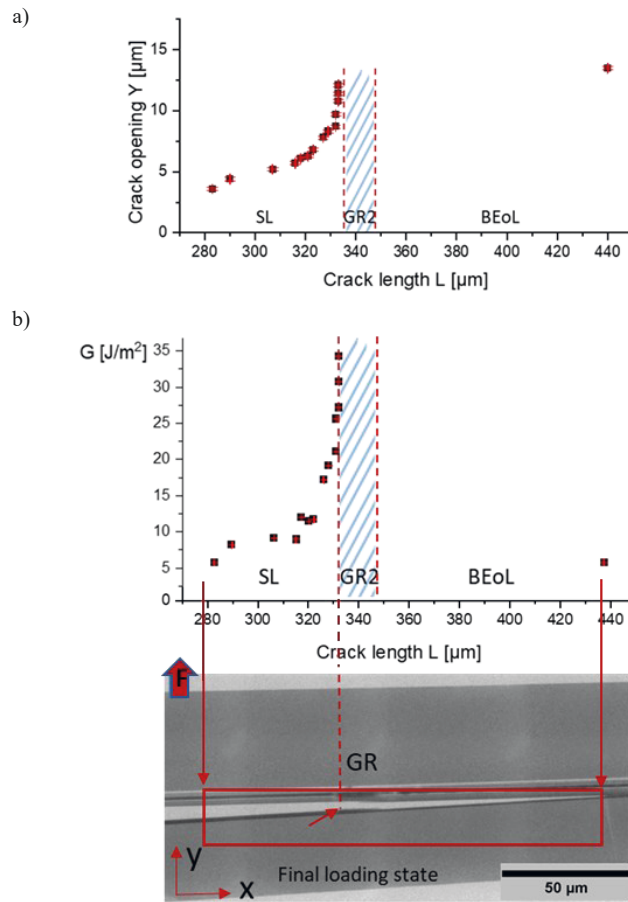


Figure 6.1:(a) Crack opening vs. crack length at several loading steps during the micro-DCB test, (b) calculated G values at several loading steps (and respective crack lengths).

The real-time monitoring of crack propagation provides invaluable insight to the failure mechanism and directions to optimize the $GR2$ design. That means, once the outermost GR ($GR1$) is broken through, the crack cannot be arrested by the remaining GRs in the current design, and eventually damage to the functional interconnect structure can occur. To understand this failure behaviour, finite element analysis, particularly 2D static calculation of the energy release rate as a function of crack length, was conducted from the manufacturer site. The result shows that the energy release rate, which is the fracture driving force, increases with longer crack length, while the fracture resistance is constant as determined by the GR materials and dimension. Therefore, an even distribution of identical GRs is not the most efficient way to stop crack penetration. Only the real-time imaging capability – and not conventional *post mortem* analysis – can reveal the critical role of the GR .

A virtual cross-section through a piece of wafer (XY plane, perpendicular to the metallization layers) at the final loading stage of a micro-DCB test, visualizing the microcrack in the on-chip interconnect stack (SL, GR2, Cu/low-k BEO_L), is provided in Figure 6.2 a. This image is based on a reconstruction of X-ray computed tomography (XCT) data (from 801 projections, data acquisition time for each projection 90 seconds). The microcrack propagated from the SL within interlayer dielectrics or along weak interfaces towards the GR2 structure, and eventually into the BEO_L stack of the microchip. The nano-XCT data allow to determine in which layer of the BEO_L stack or along which interface the microcrack propagated. To visualize the crack position in the stack, the heights of the crack above the silicon substrate (XZ horizontal map with height indicated by colors) are mapped as shown in false colors in Figure 6.2 b.

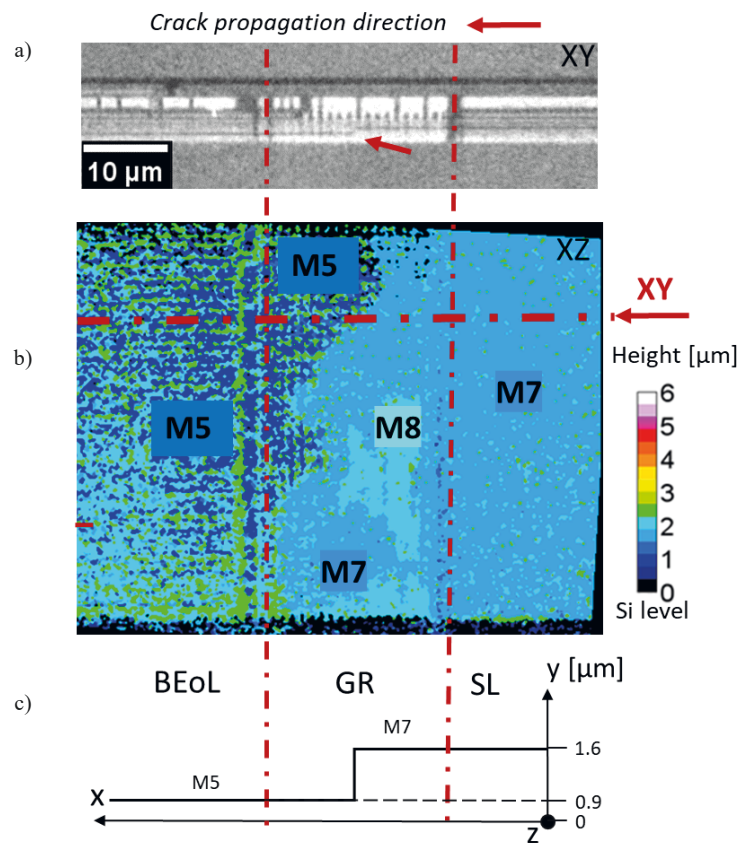


Figure 6.2: (a) Virtual cross-section (XY view) with indicated crack path change from *M7* to *M5*; (b) XZ height map of the crack in the on-chip interconnect stack (SL, GR, Cu/low-*k* BEO_L), heights above the Si substrate indicated by colors; (c) Scheme of the cross-section XY at the indicated *z* location (red line) with crack pathway, showing crack path change from *M7* to *M5*, heights above the Si substrate in μm. The color scale bar corresponds to the heights from zero (Si substrate) to about 6 μm (post passivation layer *P*).

In addition, the schematic crack path in an interconnect stack for one particular z position is provided Figure 6.2 b, that shows the crack path along $M7$ and then transferring to $M5$. The change of the crack path down from $M7$ to $M5$ is indicated by a red arrow in Figure 6.2 according scheme in Figure 6.2 c.

In this thesis, a proof-of-concept experiment was performed, to determine the critical energy release rate G_c for cracks at $GR1$ and $GR2$ using the micro-DCB test 2.0 setup, that allows to measure the applied force and the displacement simultaneously while for several loading steps. The load was applied perpendicularly to the rotational axis (same as with micro-DCB) of the sample stage of the TXM, causing the crack propagating within the BEoL stack as illustrated at $GR1$ and $GR2$ in Figure 6.3.

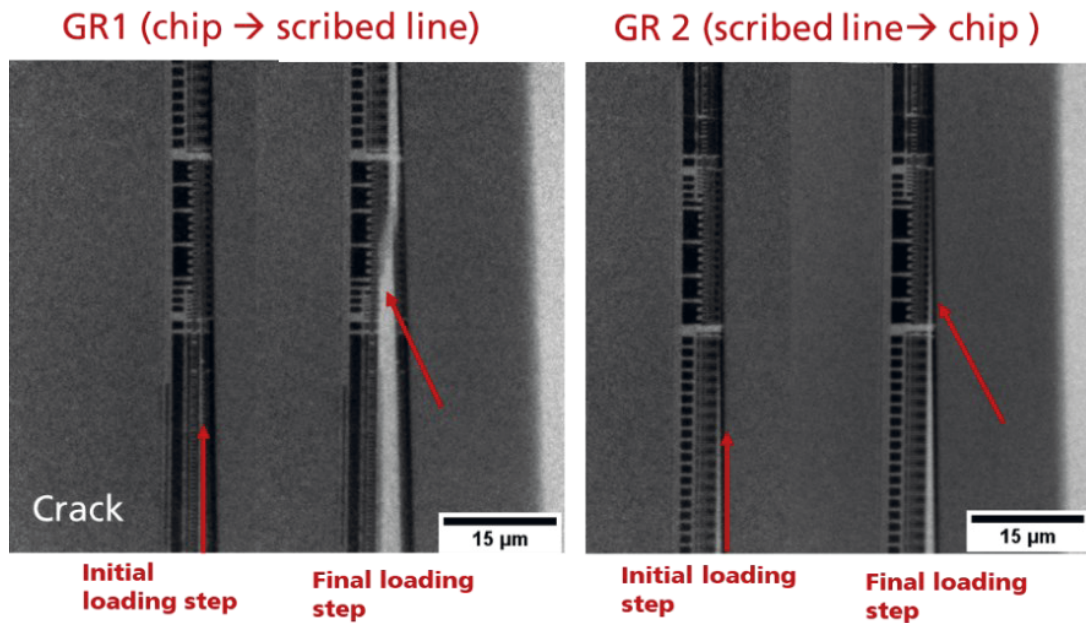


Figure 6.3: Sequence of radiographs during micro-DCB test, beam ratio $e = 0.74$ at the Guard Rings 1 and 2 ($GR1$ - crack from chip side to scribe line, and $GR2$ – from scribed line to the microchip).

The measured and corrected load-crack length data are shown in Figure 6.4, where the first drop in force value corresponds to $GR1$ failure (crack length of $240 \mu\text{m}$) and the second to $GR2$ (crack length $337 \mu\text{m}$), indicating the critical force.

X-ray tomography data of the microchip sample at the $GR2$ position were collected (801 projections each lasting 180 seconds in 180° angular range) after the micro-DCB 2.0 test. The localization of a microcrack at $M4$ and $M5$ within the $GR2$ structure is shown in a virtual

cross-section in Figure 6.5 a, and the heights of the crack above the silicon substrate (XZ horizontal map with height indicated by colors) in Figure 6.5 b.

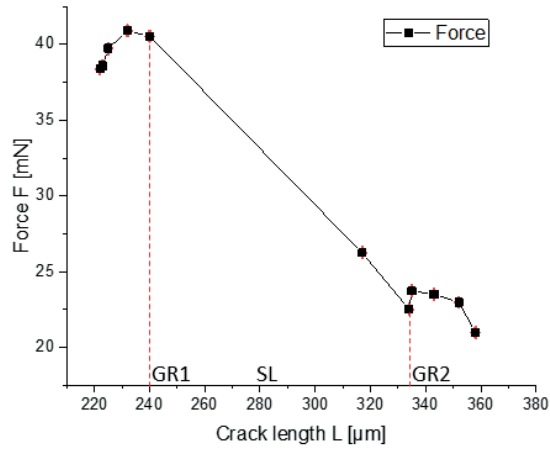


Figure 6.4: Force-crack length curve of the micro-DCB2.0 experiment with critical force for *GR1* and *GR2* failures.

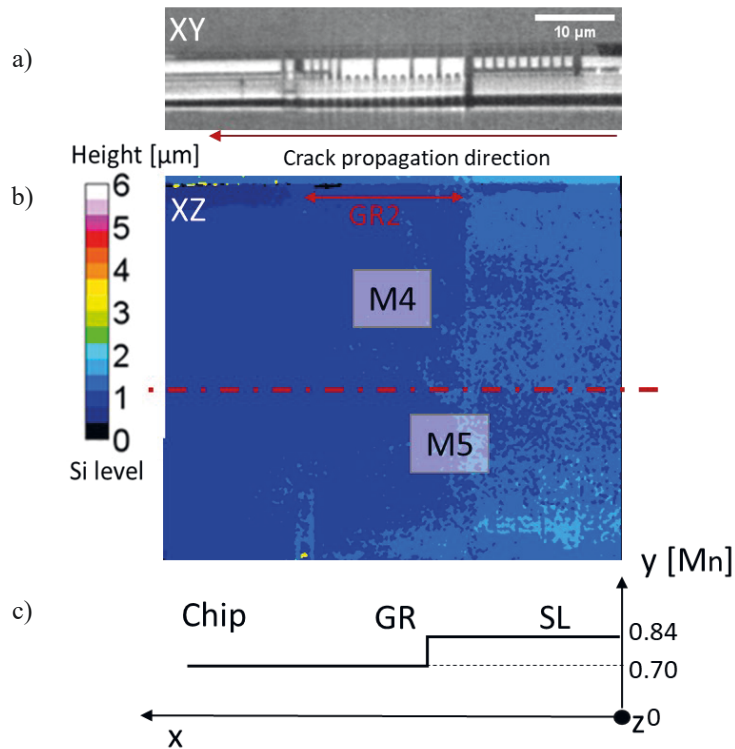


Figure 6.5:(a)Virtual cross-section (XY view) with indicated crack path change from *M5* to *M4*; (b)XZ height map of the crack in the on-chip interconnect stack (*SL*, *GR2*, *Cu/low-k BEOl*), heights above the *Si* substrate indicated by colors; (c) Scheme of the cross-section XY at the indicated *z* location (red line) with crack pathway, showing crack path change from *M5* to *M4*, heights above the *Si* substrate in μm . The color scale bar corresponds to the heights from zero (*Si* substrate) to about $6 \mu\text{m}$ (post passivation layer *P*).

The quantitative data of the energy release rate G of the guard rings achieved by applying the analytical approach described in section 3.3.2 are shown Figure 6.6 below.

The first experimental estimation of the critical energy release rate G_c of $GR1$ is approx. 56 J/m^2 and for $GR2$ approx. 27 J/m^2 . One reason of the difference could be the complex crack front at high metallization layers of $GR1$.

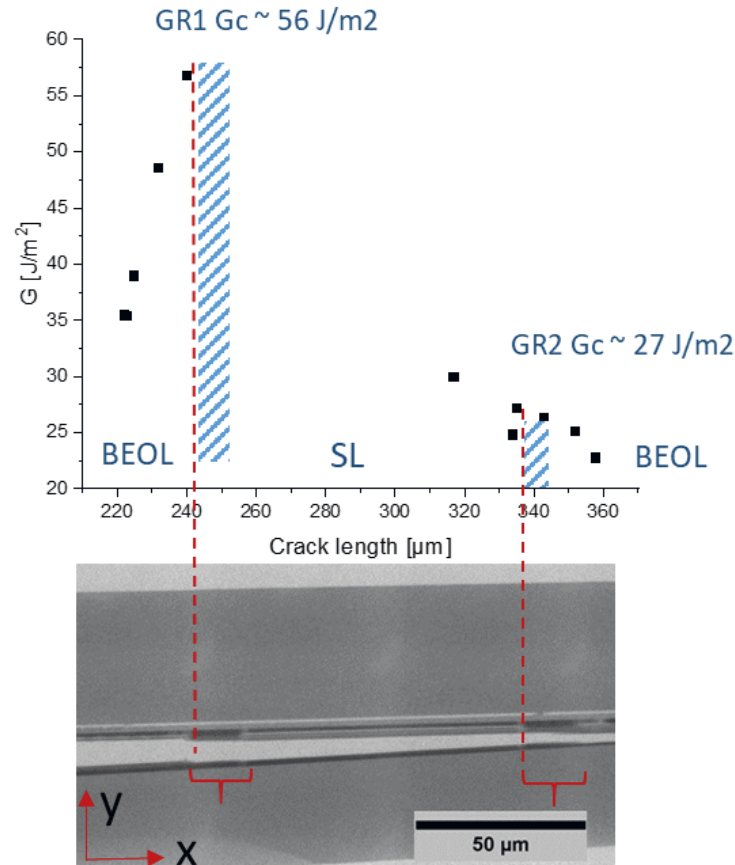


Figure 6.6: Plot of calculated G over the crack length of the micro-DCB 2.0 experiment microchip sample from Figure 6.4 and Figure 6.5. Beam ratio $e = 0.74$.

In contrast to the standard DCB test which is described in section 2.3.1, geometric inaccuracies of the sample, e.g. caused by the sample preparation, are more dominant and have to be considered in case of the micro-DCB test. In addition, 3D effects at the crack tip have to be taken into account [BCP15]. The energy release rate G for crack propagation in fracture mode I (opening or tension mode) [Cha+89] is well described for the standard DCB test, based on the Euler-Bernoulli beam model [BR57, BC09]. Considering the boundary conditions, as discussed in 3.2.2 and 3.3.2 the critical energy release rate G_c for crack propagation in the micro-DCB test can be described as the sum of the two beams, taking into

account measurable and fitted parameters: crack opening Y and ratio of the cantilever heights $e = h_1 / h_2$, force F and geometry parameters A .

As expected, the specially designed GR structures have the highest G_c value. It is several times higher than the G_c value of BEoL structures of the integrated circuit. As experimentally shown, the crack is stopped at the guard ring. This effect can be explained by the fact that the critical energy release rate G_c for crack propagation includes not only the breaking of chemical bonds across the interface (interface debond energy) but also the plasticity of adjacent ductile structures, such as copper guard rings [Dau+98]. The energy dissipation process that results in the increase of the G_c value close to the GR and a high G_c value of the GR structure itself can be explained with the geometry of the GR (GR length) and the size-dependent plasticity of copper. Compared to the dimensions of the Cu interconnects in the BEoL stack ($< 1 \mu\text{m}$, except for *M12*), the GR length in crack direction is $16 \mu\text{m}$. For Cu structures with a dimension $> 1 \mu\text{m}$, the dislocation confinement is relaxed and the plasticity zone is enlarged when the crack is approaching the copper structure, thus dissipating more mechanical energy. This effect of copper plasticity is exploited in the functionality of the guard rings. Lane and Dauskardt [Lan+00b] analyzed unpatterned layer stacks and reported an increase of G_c from 5 J/m^2 for Cu films with a thickness $< 0.5 \mu\text{m}$ to 10 J/m^2 for $1 \mu\text{m}$ films and 40 J/m^2 for $5 \mu\text{m}$ films. A direct comparison between these data for unpatterned films with dense dielectrics and data for patterned Cu /low- k structures with porous dielectrics is not possible. However, considering Cu structures with dimensions up to $2 \mu\text{m}$ (*M12*) in the BEoL stack and GR lengths of about $16 \mu\text{m}$, the G_c values determined in the micro-DCB test in this study are very reasonable.

To sum up, the implementation of a micro-DCB test in an X-ray microscope allows a 3D imaging of the pathways of micro cracks in fully integrated multilevel on-chip interconnect structures with a spatial resolution of about 100 nm . The micro-DCB experiment in an X-ray microscope allows to control fracture and to steer crack paths to regions in the on-chip interconnect stack with relatively high fracture toughness. With this technique it is possible to study the complex failure modes in realistic BEoL stacks, and to discuss the effects of process-induced thermomechanical stress and CPI on chip reliability. Based on the knowledge of how fracture mode mixity modulates the crack propagation in nanopatterned structures, it is possible to study the fracture mechanics of small structures and draw conclusions for the dielectrics materials selection to control the crack path and to ensure the required fracture resistance of BEoL structures for future advanced technology nodes. As a result, conclusions

for interconnect design, materials and processes can be drawn. Based on measured geometric shape of the crack and cantilever bending lines at several loading steps during the micro-DCB test as input data and the data analysis based on the Euler-Bernoulli beam model, the critical energy release rate G_c for crack propagation was determined in different patterned regions of the wafer manufactured in 14 nm CMOS technology node with a patterned Cu/low-k interconnect stack. The critical energy release rate G_c for crack propagation of a guard ring structure of $> 30 \text{ J/m}^2$ is significantly larger than the respective values in patterned surrounding regions with G_c values $< 10 \text{ J/m}^2$, and about one order of magnitude higher than the G_c values of the respective unpatterned dielectric thin films. These results show that, in addition to the materials properties of the dielectric materials, the geometry of the metal structures is playing an essential role for the fracture behavior of Cu/low-k interconnect stacks [Kut+22b].

With the methodology described in this thesis, conclusions for the robustness of on-chip interconnect stacks can be drawn and input for the design of guard ring structures can be provided. The importance of the controlled crack path steering to the tougher regions opens great opportunity to provide information for the future developing nodes. This new approach has important implications for on-chip interconnect technology development and for fundamental study of fracture behaviors of materials in the nanometer scale non-destructively. The demonstration of the role of plasticity of 3D micro- and nano-scaled metal structures on the fracture mechanics of nanopatterned structures provides a better understanding of fracture mechanics at small scales, and eventually, to avoid material cracking and interface delamination.

6.2 Controlled crack path steering in BEoL stacks

The micro-DCB test results were achieved from a sample of two beams with the same target heights (“symmetric samples”), i.e. the ratio of the heights $e = h_1/h_2$ of the dummy beam h_1 and the chip beam (with the ROI) h_2 was supposed to be $e = 1$. However due to sample geometry imperfections, the real value is $e = 1.3$ for instance provided in Figure 6.2. Hence, the crack path changes from metallization layer $M7$ to the lower metallization layer $M5$, even for a nearly “symmetric sample” can be explained with the e value, which deviates from the ideal value $e = 1$, i.e. with the superposition of the fracture modes I and II for crack propagation.

In addition, defined asymmetric DCB samples, i.e. with different beam heights h_n , $n = \{1,2\}$, were prepared and studied. For these asymmetric sample geometries, mode II (sliding mode or in-plane shear mode) condition for crack propagation occurs in addition to the mode I condition. These test conditions reflect a combination of loading modes, the mode-mixity [LK17, Li+13]. The chosen thickness ratios $e = h_1 / h_2$ of dummy beam (h_1) and chip beam (h_2), 2.0 and 0.5, respectively, are related to the global mode angles $\pm 23^\circ$ for these asymmetric cases – in contrast to 0° for the symmetric case. For micro-DCB samples with a targeted sample thickness of $50 \mu\text{m}$, the target beam heights in these asymmetric cases were $16.7 \mu\text{m}$ and $33.3 \mu\text{m}$. However, the real beam geometries that differ slightly from the target values were determined based on radiographs, and the real beam thickness ratios e were calculated from these image data, as shown in Figure 6.7 below.

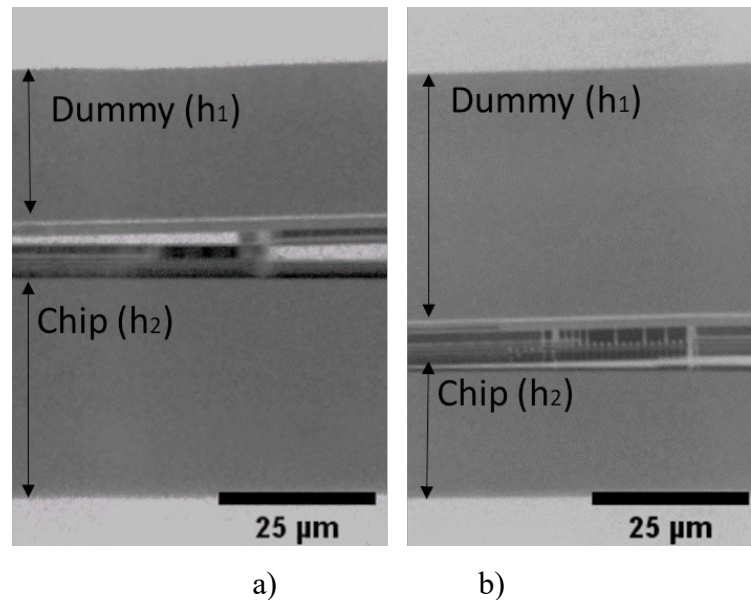


Figure 6.7. Radiographs of two micro-DCB samples with asymmetric geometry: (a) $e = 0.65$ ($h_1 = 25 \mu\text{m}$, $h_2 = 38 \mu\text{m}$) and (b) $e = 2.10$ ($h_1 = 40 \mu\text{m}$, $h_2 = 19 \mu\text{m}$).

Figure 6.8 shows virtual cross-sections through pieces of wafers at the final loading stage of a micro-DCB test, visualizing the microcrack in the on-chip interconnect stack (*SL*, *GR*, *Cu/low-k BEO_L*) in virtual x-sections (a), the heights of the crack above the silicon substrate (*XZ* horizontal maps of the cracks (b) and schematic crack paths in the interconnect stacks for particular *z* positions (c) for two different mode mixity cases shown in Figure 6.7. The microcrack is steered from *M10* to *M12* in the case of $e = 0.65$ and from *M6* via *M3* to *M2* in the case of $e = 2.10$.

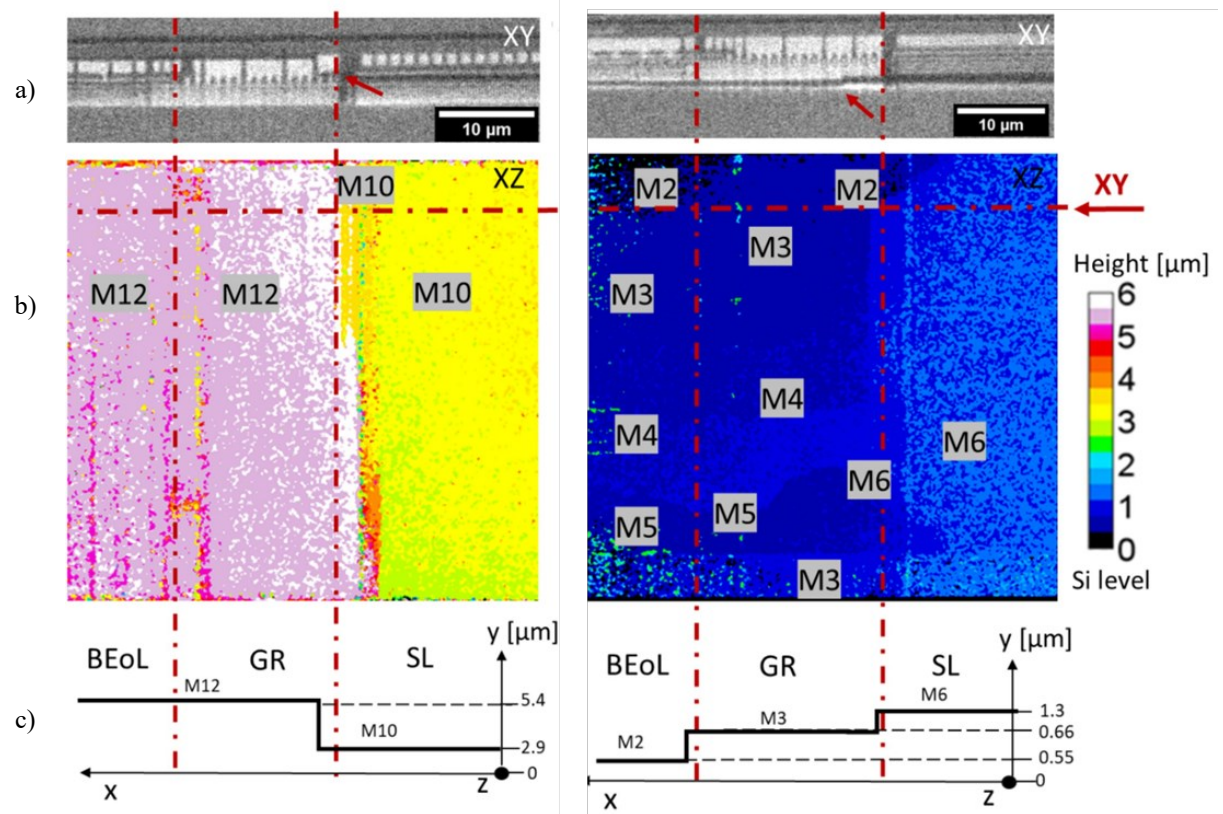


Figure 6.8: Virtual cross-sections (XY views) with indicated crack path changes (a); XZ height maps of the crack in the on-chip interconnect stack (*SL*, *GR*, *Cu/low-k BEOl*), heights above the *Si* substrate indicated by colors; Schemes of the cross-section XY at the indicated *z* location (red line) with crack pathways (c), showing crack path changes from *M10* to *M12* (sample in Figure 6.7 a) and *M6* via *M3* to *M2* (sample in Figure 6.7 b).

For each geometrical configuration (symmetric case and two asymmetric cases), a set of micro-DCB experiments in the X-ray microscope were performed, and nano-XCT data sets were generated as described above. The crack pathways were analyzed based on the 3D tomography data set for each sample. The resulting data for each geometrical configuration is presented in the graph in Figure 6.9.

Figure 6.9 shows that microcracks are moving predominantly to higher metallization layers for $e < 1$ and predominantly to lower metallization layers for $e > 1$. That means, microcracks can be steered into a particular level of the layer stack as a result of fracture mode mixity for crack propagation.

The steering of the crack path to higher metallization levels, as characteristic for beam thickness ratios $e < 1.0$, is the preferred option since the fracture resistance or the critical energy release rate for crack propagation is increased the closer the microcrack will be to *M12*. The reason is the thickness of the *M12 Cu* metallization of about 2 μm, in contrast to the *M1*

to *M11* metallization layers with thicknesses lower than 1 μm . In addition to an enhanced near-tip sliding and friction caused by mode mixity [HS91], the plasticity of the copper in *M12* increases the energy dissipation. This effect can be explained by the fact that the critical energy release rate G_c includes not only the breaking of chemical bonds across the interface (interface debond energy) but also the plasticity of adjacent ductile structures, such as relatively thick *Cu* lines [Dau+98].

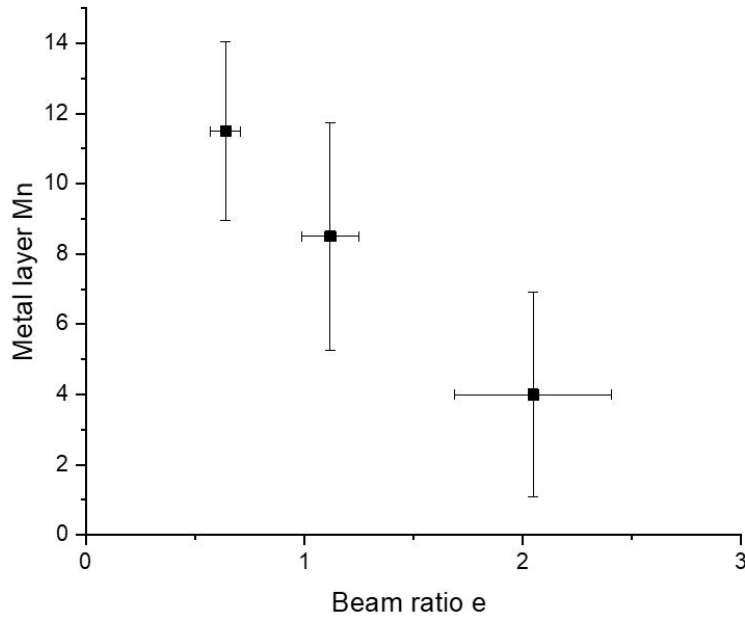


Figure 6.9: Dominant metal layers of crack propagation for several beam height ratios e , based on 7 samples for $e \approx 0.5$, 9 samples for $e \approx 1$, and 12 samples for $e \approx 2$, error bars from statistical data analysis.

The energy dissipation process that results in the increase of the G_c value close to the thick *Cu* lines can be explained with the size-dependent plasticity of copper. For *Cu* structures with a dimension > 1 mm, the dislocation confinement is relaxed and the plasticity zone is enlarge when the microcrack is approaching the *Cu* structure, thus dissipating more mechanical energy. This effect of copper plasticity is exploited in the *M12* *Cu* lines. Lane et al. [Lan+00a, Lan+00b] analyzed unpatterned layer stacks and reported an increase of G_c by $> 400\%$ as the *Cu* layer thickness was increased from 0.3 mm to 3.3 mm. From a figure published in [Lan+00b], G_c values of 5 J/m^2 , 5 – 10 J/m^2 and 14 J/m^2 were extracted for *Cu* thickness values of ≤ 0.20 μm (*M1* – *M6*), 0.35 – 0.72 μm (*M7* – *M11*) and 2.02 μm (*M12*). A quantitative comparison between these data for unpatterned films with SiO_2 dielectrics and data for patterned *Cu*/low- k structures with porous dielectrics is not possible. In addition, chemical composition of the electroplated copper and process parameters for deposition and

thermal treatment are certainly different. However, considering *Cu* structures with dimensions of 2 μm (*M12*) in the BEoL stack, the crack propagation is expected to be slowed down, and in the best case the microcrack will be stopped. Since the plastic zone size exceeds the *Cu* layer thickness [Lan+00b], this effect occurs also in the dielectrics next to the *Cu* structure. This toughening effect – energy dissipation caused by plasticity - is consistent with model predictions [WH99, Kle+99]. The importance of the controlled crack path steering to the tougher regions opens great opportunity to study certain layer at high resolution and provide high level information for the future developing nodes.

7 Summary and outlook

7.1 Summary

An experimental approach for in-situ high-resolution 3D imaging of the fracture behavior of 3D-nanopatterned structures and of the kinetics of microcrack propagation in solids is presented in this thesis. With the combination of a miniaturized micromechanical experiment and high-resolution X-ray imaging, controlled steering of microcracks was demonstrated for a technically relevant 3D-nanopatterned system, the 3D on-chip interconnect stack of an integrated circuit, and the critical energy release rate at the crack tip was determined quantitatively in sub-100nm dimension.

- A micromechanical test set-up was integrated into an X-ray microscope for high-resolution imaging of 3D details of microcrack evolution in the on-chip interconnect stack of a microchip manufactured in the 14 nm CMOS technology node. Two miniaturized piezo-driven double cantilever beam test set-ups (micro-DCB) were applied in a laboratory TXM (photon energy 8 keV) to study in-situ crack opening and propagation in 3D-nanopatterned Cu/low-k interconnect stacks, while applying a load to the specially prepared sandwich-like sample. The fracture behavior of a Cu/low-k interconnect stack based on a displacement-controlled micro-DCB test, with sub-100 nm spatial resolution. For both micromechanical testers, without and with force sensor measurement, image analysis procedures were developed and applied. The advantage of the new micro-DCB 2.0 tester is a significant reduction in the numerical efforts for data analysis.
- Based on the measured crack geometry, the critical energy release rate for crack propagation can be determined for 3D-nanopatterned structures, e.g. for fully integrated multilevel interconnect structures of microchip. Using the measured geometry of the crack at several loading steps during the micro-DCB test together with a data analysis based on linear elastic fracture mechanics and the Euler-Bernoulli beam model, the critical energy release rate for crack propagation in different regions of a processed silicon wafer was determined quantitatively.
- It was demonstrated that it is possible to steer the microcrack in a controlled way by tuning the fracture mode mixity locally at the crack tip and to acquire simultaneously the 3D image information of a region of interest. This experimental approach allows

to force a displacement-controlled crack propagation through the on-chip interconnect stack of an integrated circuit and at the same time to image the pathways of microcracks in fully integrated, nanopatterned multilevel interconnect structures with sub-100 nm resolution.

- For the synchrotron-radiation based X-ray microscopy study of crack evolution in the on-chip interconnect stack, a specially designed manipulator for the indentation into a sample thinned to several micrometers was developed and used. The experiment allowed a direct observation of crack propagation with a spatial resolution of 25 nm. This resolution will be needed for the studies at nanopatterned structures with sub-100 nm features.

The role of the design of a 3D-nanopatterned structure on the microcrack propagation was demonstrated for metallic guard ring (GR) structures at the rim of the microchip. These specially designed metal structures are integrated into BEoL stacks to dissipate energy in such a way that the microcrack propagation is efficiently slowed down and eventually stopped. It was experimentally proven that these GR structures are effective to prevent the mechanical damage of microchips manufactured in leading-edge CMOS technology nodes.

- The critical energy release rate G_c for crack propagation was determined for different patterned regions of the wafer manufactured in 14 nm CMOS technology node with a patterned Cu/low-k interconnect stack. The critical energy release rate G_c for crack propagation of a GR structure of $> 30 \text{ J/m}^2$ is significantly larger than the respective values in patterned surrounding regions with G_c values $< 10 \text{ J/m}^2$, and about one order of magnitude higher than the G_c values of the respective unpatterned dielectric thin films. These results show that, in addition to the materials properties of the dielectric materials, the geometry of the metal structures is playing an essential role for the fracture behavior of Cu/low-k interconnect stacks.

- It was experimentally shown that the mode mixity – given by the sample geometry, i.e. the thickness ratio $e = h_1/h_2$ of the two beams of a micro-DCB sample (thickness of the dummy beam h_1 and of the microchip beam h_2) - plays an important role in determining the path selection of a propagating crack inside the multi-level integrated on-chip interconnect structure, and consequently for a controlled microcrack steering. It was shown that microcracks tend to kink predominantly to upper metallization layers for $e < 1$, and predominantly to lower metallization layers for $e > 1$. At the same time,

initiation location, local metal density and toughness at each metallization layer collectively contribute to determine the eventual crack path selection.

The test of the integrated structures and materials with the novel approach described in this thesis allows to evaluate process-induced materials changes and provides a pathway to study the scaling of mechanical properties of materials. The experimental results gathered at realistic interconnect structures provide valuable information to control the fracture path in the BEoL materials stacks for design-for-reliability (DFR) of advanced microelectronic products. The experimental study of controlled microcrack steering into regions with high fracture toughness provides knowledge for the design of guard ring structures in microchips to stop the propagation of microcracks, e.g. generated during the wafer dicing process.

The experimental approach and the test samples used are not limited to samples from microelectronic products. The established concept for a controlled crack propagation can be adopted to study other materials systems as well. It opens new approaches for fundamental studies of the fracture behavior of constrained nanoscale materials and structures. The results reported in this thesis have implications for the understanding of fracture mechanics at small scales, e.g. in microchips as presented here, but also in other nanopatterned materials, e.g. bio-inspired, hierarchically structured engineered materials.

7.2 Outlook

The methodology presented in this thesis, i.e. the high-resolution 3D imaging of kinetic processes in 3D-nanostructured systems and materials, is extendable to the use of other experimental set-ups for in-situ studies (e.g. set-ups for fatigue studies and other mechanical tests such as 4-point bending and indentation as well as for the additional impact of environmental conditions) and to other natural and bio-inspired systems and materials (e.g. hierarchically structured biological and engineered materials such as composites, porous and skeleton materials).

The study of micromechanical properties of natural systems and biomaterials, that have been 'designed' during a long-term evolution process, with the goal for the living object to survive and to adapt to its surrounding environment, requires the integration of specially designed and built in-situ set-ups into the X-ray microscope, allowing in-situ experiments under conditions that are close to the reality. Examples are laboratory TXM studies of fossil diatom frustules in wet environment and of protecting mollusk shells applying

indentation [Str+20]. Because of the ability to study not only the morphology of biomaterials in a certain state but also kinetic processes in natural systems, an increase of such studies is expected in the next years, both at synchrotron radiation facilities and in laboratories. X-ray microscopy will support biomimetics in particular, e.g. targeting on bio-inspired engineered damage-tolerant 3D-nanopatterned structures, e.g. microchips as discussed in this thesis. The nature's design principles for damage-tolerant materials that result in a controlled crack steering into regions with high fracture toughness [MKB14] can provide valuable information for the design of engineered materials systems such as backend-of-line stacks of integrated circuits or guard ring structures.

A particular future field of *in-situ* and *operando* X-ray microscopy studies will be the investigation of morphology changes in materials as well as of ageing and degradation effects in systems including defect evolution, e.g. microcrack propagation, in materials and systems during timely changing load profiles (frequency, stress ratio, etc.), e.g. during mechanical fatigue in structural and functional materials. The understanding of the degradation mechanisms such as micropore and microcrack evolution, depending on in-service mechanical, thermal and electrical load profiles, will be the basis for the design and fabrication of more robust high-tech products such as microchips, sensors or batteries.

The experimental approach to control the fracture behavior of 3D-nanopatterned structures in real time and to describe the microcrack propagation in solids quantitatively is presented in this thesis for an on-chip interconnect stack of a microchip manufactured in 14 nm CMOS technology node. For 10 nm and sub-10 nm CMOS technology nodes, not only the transistors are scaled down but also the metal interconnects. Consequently, a higher spatial resolution of TXM will be needed to identify the location of the microcrack paths in the BEoL stack. In addition to complementary synchrotron radiation TXM studies in the soft X-ray range as described, there will be also the request from semiconductor industry to image the microcrack propagation in thicker samples using high-energy X-rays with sub-50 nm resolution, preferable using laboratory TXM tools. This demand will need new scientific and engineering solutions, particularly novel X-ray lenses, e.g. Fresnel zone plates with thinner zones.

Since the described combination of a miniaturized micromechanical experiment and high-resolution X-ray imaging is able to provide micromechanical properties of materials quantitatively in sub-100 nm dimension, the scale-dependence of these parameters can be investigated systematically. With this unique characterization capability, essential

experimental input will be provided for design and manufacturing of robust microchips in future technology nodes, and it is expected that it will be applied in addition to a broad variety of 3D nanostructured material systems.

High-resolution 3D imaging of microcrack evolution using X-ray microscopy and the determination of micromechanical properties in sub-100 nm regions, combined with modeling and simulation, will provide an essential impact to the development of fracture mechanics at small scales. Fracture mechanics of materials in micro- and nanoscale dimensions will become an increasingly important field of fundamental research, including solid-state physics. Based on a profound understanding of fracture mechanics in small dimensions, risk mitigation strategies for fracture of materials and failure of devices and systems will be established.

References

- [AF11] J.I. Agulleiro, J.J. Fernandez „Fast tomographic reconstruction on multicore“, *Bioinformatics* 27, pp. 582-583 (2011), doi:10.1093/bioinformatics/btq692
- [And05] T.L. Anderson, “Fracture Mechanics: Fundamentals and Applications”, Third edition, CRC Press Taylor & Francis Group, (2005), pp 34-36.
- [Ast+19] J. Ast, M. Ghidelli, K. Durst, M. Goeken, M. Sebastiani, A. M. Korsunsky, „A review of experimental approaches to fracture toughness evaluation at the micro-scale“, *Mater. Des.* 173, (2019), doi: 10.1016/j.matdes.2019.107762
- [Bak+12] M. Baklanov, P. S. Ho, E. Zschech (Eds.), “Advanced Interconnects for ULSI Technology”, J. Wiley & Sons, Chichester (2012), doi:10.1002/9781119963677
- [BC09] O. A. Bauchau, J. I. Craig, eds. „Structural Analysis“, Springer Dordrecht, pp. 173 – 221 (2009)
- [BCP15] F. Berto, A. Campagnolo, L. P. Pook, “Three-dimensional effects on cracked components under anti-plane loading”, *Frattura ed Integrità Strutturale*, 33, 17 - 24 (2015), doi: 10.3221/IGF-ESIS.33.03
- [Bes+16] J. P. Best, J. Zechner, J. M. Wheeler, R. Schoeppner, M. Morstein, J. Michler, „Small-scale fracture toughness of ceramic thin films: the effects of specimen geometry, ion beam notching and high temperature on chromium nitride toughness evaluation“, *Phil. Mag.* 96, pp. 3552 – 3569 (2016), doi:10.1080/14786435.2016.1223891
- [BR57] J. J. Benbow, F. C. Roesler, “Experiments on controlled fractures”, *Proc. Phys. Soc. B* 70.2, 201 (1957), doi:10.1088/0370-1301/70/2/307
- [Cha+89] P. G. Charalambides, J. Lund, A. G. Evans, R. M. McMeeking, “A test sample for determining fracture resistance of bimaterial interfaces”, *J. Appl. Mech.* 56(1), pp.77 - 82 (1989), doi:10.1115/1.3176069
- [Chu+09] D. Chumakov, F. Lindert, M. U. Lehr, M. Grillberger, E. Zschech, *IEEE Transactions on Semiconductor Manufacturing*, Vol. 22, no. 4, pp. 603-616, (2009), doi: 10.1109/TSM.2009.2035677

- [CL18] Y-L. Cheng, C-Y. Lee, "Porous Low-Dielectric-Constant Material for Semiconductor Microelectronics", In: IntechOpen, Open access peer-reviewed chapter: Nanofluid Flow in Porous Media, (2018), doi: 10.5772/intechopen.81577.
- [Dau+98] R. H. Dauskardt, M. Lane, Q. Ma, N. Krishna, „Adhesion and debonding of multi-layer thin film structures", Engineering Fracture Mechanics 61.1, pp. 141 - 162 (1998), doi:10.1016/S0013-7944(98)00052-6
- [Dau05] R. H. Dauskardt, "Delaminator - Adhesion Testing System", Menlo Park/CA, USA (2005)
- [Dil2021] T. Dillinger, in SwmiWiki, "The Latest in Dielectrics for Advanced Process Nodes", <https://semiwiki.com/semiconductor-manufacturers/intel/294379-the-latest-in-dielectrics-for-advanced-process-nodes/>, visited on 08.01.2022.
- [Fan16] Y. Fan, „Resistive Switching Behavior in Low-K Dielectric Compatible with CMOS Back End Process ", Master Thesis, Virginia Polytechnic Institute and State University (2016), <http://hdl.handle.net/10919/78172>
- [Gal+12] S. Gallois-Garreignot, V. Fiori, C. Moutin, C. Tavernier, "Chip/package interactions on advanced flip-chip packages: Mechanical investigations on copper pillar bumping," 2012 4th ESTC, 2012, pp. 1-6, doi: 10.1109/ESTC.2012.6542106.
- [Ger+17] W. Gerberich, E. B. Tadmor, J. Kysar, J. A. Zimmerman, A. M. Minor, I. Szlufarska, J. Amodeo, B. Devincre, E. Hintsala, R. Ballarini, "Review Article: Case studies in future trends of computational and experimental nanomechanics", J. Vac. Sci. Technol. A 35, 060801 (2017), doi: 10.1116/1.5003378
- [Gri+08] A. Grill, D. Edelstein, M. Lane, V. Patel, S. Gates et al., "Interface engineering for high interfacial strength between SiCOH and porous SiCOH interconnect dielectrics and diffusion caps", J. Appl. Phys. 103, 054104 (2008); doi: 10.1063/1.2844483
- [Gri+14] A. Grill, S. M. Gates, T. E. Ryan, S. V. Nguyen, and D. Priyadarshini, "Progress in the development and understanding of advanced low k and ultralow k dielectrics for very large-scale integrated interconnects - State of the art", Appl. Phys. Rev.1.1 p. 011306 (2014), doi: 10.1063/1.4861876

- [Gri21] A. A. Griffith, "The phenomena of rupture and flow in solids", *Philosophical Transactions of the Royal Society of London, A*, 221 pp 163–198, (1921), doi:10.1098/rsta.1921.0006
- [Har+18] C. Hartfield, C. Schmidt, A. Gu and S. T. Kelly, "From PCB to BEoL: 3D X-Ray Microscopy for Advanced Semiconductor Packaging," 2018 IEEE (IPFA), Singapore, pp. 1-7, (2018), doi: 10.1109/IPFA.2018.8452551
- [Hen93] B. L. Henke, E. M. Gullikson, and J. C. Davis. X-ray interactions: photoabsorption, scattering, transmission, and reflection at $E=50\text{-}30000$ eV, $Z=1\text{-}92$, *Atomic Data and Nuclear Data Tables Vol. 54* (no.2), 181-342 (1993). henke.lbl.gov/optical_constants/
- [HS91] J. W. Hutchinson, Z. Suo, "Mixed Mode Cracking in Layered Materials", *Adv. Appl. Mech.* 29, pp.63 – 191, (1991), doi.10.1016/S0065-2156(08)70164-9
- [Ing+08] D. Ingerly, S. Agraharam, D. Becher, V. Chikarmane, K. Fischer, R. Grover, M. Goodner, S. Haight, J. He, T. Ibrahim et al., "Low-K Interconnect Stack with Thick Metal 9 Redistribution Layer and Cu Die Bump for 45nm High Volume Manufacturing", *Proceedings of IITC, Burlingame, CA, USA*, pp. 216–218, (2008), doi: 10.1109/IITC.2008.4546971
- [Ing+12] D. Ingerly, A. Agrawal, R. Ascazubi, A. Blattner, M. Buehler, V. Chikarmane, B. Choudhury, F. Cinnor, C. Ege, C. Ganpule et al., "Low-k interconnect stack with metal-insulator-metal capacitors for 22nm high volume manufacturing", *Proceedings of the IITC, San Jose, CA, USA*, pp. 1–3, (2012), doi: 10.1109/IITC.2012.6251663
- [Irw57] G. Irwin, "Analysis of stresses and strains near the end of a crack traversing a plate", *J. Appl. Mech.* 24, pp. 361–364, (1957), doi:10.1115/1.4011547
- [Jav+16] B. N. Jaya, J. M. Wheeler, J. Wehrs, J. P Best, R. Soler, J. Michler, C. Kirchlechner, G. Dehm, "Microscale Fracture Behavior of Single Crystal Silicon Beams at Elevated Temperatures ", *Nano Lett.* 16, pp. 7597 – 7603, (2016), doi: 10.1021/ACS.NANOLETT.6B03461
- [KJ09] J. Kirz, C. Jacobsen, "The history and future of X-ray microscopy", *J. Phys. Conf. Ser. Vol. 186*. 012001, pp. 1-11, (2009), doi: 10.1088/1742-6596/186/1/012001

- [Kle+99] P. Klein, H. Gao, A. Vainchtein, H. Fujimoto, J. Lee, and Q. Ma, Proceedings Annual Meeting MRS, Warrendale, PA, (1999)
- [KN13] P. Krüger, S. Niese. Bead Aligner. Projection alignment plugin for ImageJ written in Java. In-house development of Fraunhofer IKTS-MD (2013)
- [KS88] A. C. Kak, M. Slane, “Principles of Computerized Tomographic Imaging”, IEEE Press, (1988). url: <http://www.slaney.org/pct/>
- [Kun08] T. Kundu, “Fundamentals of fracture mechanics”, CRC Press Taylor & Francis Group, pp 120-123, (2008)
- [Kut+17] K. Kutukova, J. Gluch, Y. Standke, E. Zschech, “Crack Evolution In Cu/Low-K Stacks And Crack Stop Evaluation Using In-Situ Micro-DCB In A Nano-XCT Tool”, FCMN conference, March 2017, Monterey/CA (2017).
- [Kut+18a] K. Kutukova, S. Niese, J. Gelb, R. Dauskardt, and E. Zschech, “A novel micro-Double Cantilever Beam (micro-DCB) test in an X-ray microscope to study crack propagation in materials and structures”, Mater.Today Commun. 16, pp. 293–299, (2018), doi: 10.1063/1.3169259
- [Kut+18b] K. Kutukova, S. Niese, C. Sander, Y. Standke, J. Gluch, M. Gall and E. Zschech, “A laboratory X-ray microscopy study of cracks in on-chip interconnect stacks of integrated circuits”, in Appl. Phys. Lett. 113, 091901 (2018); doi: 10.1063/1.5031204
- [Kut+18c] K. Kutukova, P. Guttman, Z. Liao, S. Werner, Y. Standke, J. Gluch, G. Schneider, E. Zschech, „In-situ X-ray Microscopy of Crack-Propagation to Study Fracture Mechanics of On-Chip Interconnect Structures”, MRS Adv. 3(39), pp. 2305–2310 (2018), doi: 10.1557/adv.2018.410
- [Kut+22a] K. Kutukova, J. Gluch, M. Kraatz, A. Clausner, E. Zschech, “In-situ Micro-DCB / Nano-XCT Test to Ensure the Robustness of Leading-edge Cu/ULK BEoL Stacks”, FCMN conference, June 2022, Monterey/CA (2022)
- [Kut+22b] K. Kutukova, J. Gluch, M. Kraatz, A. Clausner, E. Zschech, „In-situ X-ray tomographic imaging and controlled steering of microcracks in 3D nanopatterned structures”, Materials & Design, Volume 221, 110946,(2022), doi: 10.1016/j.matdes.2022.110946

- [Kut16] K. Kutukova, "Combination of X-ray tomography and in-situ micro mechanical testing of composites", Master Thesis, Dresden international University, December 2016, Dresden, Germany (2016)
- [Lan+00a] M. Lane, R.H. Dauskardt, N. Krishna, et al., "Adhesion and reliability of copper interconnects with Ta and TaN barrier layers", *Journal of Materials Research* 15, pp. 203–211 (2000), doi:10.1557/JMR.2000.0033
- [Lan+00b] M. Lane, R. H. Dauskardt, A. Vainchtein, et al., "Plasticity contributions to interface adhesion in thin-film interconnect structures", *Journal of Materials Research* 15, 2758–2769 (2000), doi:10.1557/JMR.2000.0395
- [Lan+04] M. Lane, Xia Hu Liu, T. M. Shaw, "Environmental effects on cracking and delamination of dielectric films," in *IEEE Transactions on Device and Materials Reliability*, vol. 4, no. 2, pp. 142-147, June 2004, doi: 10.1109/TDMR.2004.829123
- [Lan+07] M. Lane, T. M. Shaw, X. H. Liu, "Effects of material advancement and scaling on chip-package reliability", Presentation on 8th ICEPT, Shanghai, China, 14-17 Aug. (2007)
- [Lan03] M. Lane, „Interface Fracture”, *Annu. Rev. Mater. Res*, vol 33, pp.29–54, 2003, doi: 10.1146/annurev.matsci.33.012202.130440
- [Li+13] H. Li, M. J. Kobrinsky, A. Shariq, J. Richards, J. Liu, M. Kuhn, "Controlled fracture of Cu/ultralow-k interconnects", *Appl. Phys. Lett.*, 103, 231901 (2013), doi: org/10.1063/1.4837676
- [Li+14] Y. Li, M. Pacheco, D. Goyal, J. W. Elmer, H. D. Barth, D. Parkinson, "High resolution and fast throughput-time X-ray computed tomography for semiconductor packaging applications," 2014 IEEE 64th ECTC, Orlando, FL, USA, pp. 1457-1463, (2014), doi: 10.1109/ECTC.2014.6897485
- [Lit+03] C. Litteken et al., "Interfacial adhesion of thin-film patterned interconnect structures," *Proceedings of the IEEE*, pp. 168-170, (2003), doi: 10.1109/IITC.2003.1219744
- [Liu+17] X. Liu, J. Shang, J. Hao, A. Hu, L. Gao, M. Li, "Impact of tensile strength on thermal fatigue properties and failure modes of Sn-Ag-Cu-Ni solder joints". 18th ICEPT, 984-987 (2017), doi:10.1109/ICEPT.2017.8046608.

- [LK17] H. Li, M. Kuhn, “Controlled Fracture and Mode-Mixity Dependence of Nanoscale Interconnects”, *IEEE TDMR* 17, (2017), pp. 636–642, doi: 10.1109/TDMR.2017.2767905
- [Lut+21] F. Lutter, P. Stahlhut, K. Dremel, S. Zabler, J. Fell, H.G. Herrmann, R. Hanke, “Combining X-ray Nano Tomography with focused ion beam serial section imaging — Application of correlative tomography to integrated circuits”, *NIMB*, Vol. 500-502, pp.10-17, (2021), doi: 10.1016/j.nimb.2021.05.006
- [MG13] A. P. Merkle, J. Gelb, “The Ascent of 3D X-ray Microscopy in the Laboratory”, *Microsc. Today* 21(2), pp.10–15 (2013), doi: 10.1017/S1551929513000060
- [MKB14] M. Mirkhalaf, A. Khayer Dastjerdi, F. Barthelat, „Overcoming the brittleness of glass through bio-inspiration and micro-architecture “, *Nat Commun* 5:3166 (2014); doi: 10.1038/ncomms4166.
- [Mol+07] J. M. Molina-Aldareguia, I. Ocan, D. Gonzalez, M. R. Elizalde, J. M. Sanchez, J. M. Martinez-Esnaola, J. Gil-Sevillano, T. Scherban, D. Pantuso, B. Sun, G. Xu, B. Miner, J. He, J. Maiz „Adhesion studies in integrated circuit interconnect structures “, *Engin. Fail. Analys.*, 14, 349–354 (2007), doi: 10.1016/j.engfailanal.2006.02.008
- [Moll+10] V. Mollon, J. Bonhomme, J. Vina, A. Argüelles, “Mixed mode fracture toughness: An empirical formulation GI/GII determination in asymmetric DCB specimens”, *Engineering Structures* 32, 3699-370, (2010), doi: 10.1016/j.engstruct.2010.08.014
- [Nat+14] S. Natarajan, M. Agostinelli, S. Akbar, M. Bost, A. Bowonder, V. Chikarmane, S. Chouksey, A. Dasgupta, K. Fischer, Q. Fu et al., “A 14nm Logic Technology Featuring 2nd-Generation FinFET, Air-Gapped Interconnects, Self-Aligned Double Patterning and a 0.0588 μm^2 SRAM cell size”, *EEE IEDM*, San Francisco/CA, (2014), doi: 10.1109/IEDM.2014.7046976
- [Nie15] S. Niese, “Lab-based in-situ X-ray microscopy – Methodical developments and applications in materials science and microelectronics “, PhD thesis, BTU Cottbus (2015)
- [Phi18] Phidgets Inc., last modified on 27 November 2018, licensed under a Creative Commons Attribution-NonCommercial-NoDerivs 3.0 Unported License, https://www.phidgets.com/docs/Calibrating_Analog_Sensors

- [PWK18] R. Pippan, S. Wurster, D. Kiener, "Fracture mechanics of micro samples: Fundamental considerations ", *Materials and Design*, Volume 159, pp. 252-267, (2018), doi: 10.1016/j.matdes.2018.09.004
- [Ras13] W. Rasband. ImageJ, U. S. National Institutes of Health, Bethesda, Maryland, USA, (1997–2013) <http://imagej.nih.gov/ij/>
- [Reh+12] S. Rehbein, P. Guttmann, S. Werne, G. Schneider, „Characterization of the resolving power and contrast transfer function of a transmission X-ray microscope with partially coherent illumination “, *Optics Express* Vol. 20, pp.5830-5839 (2012), doi: 10.1364/OE.20.005830
- [Sch+02] G. Schneider, M. A. Meyer, G. Denbeaux, E. Anderseon, B. Bates, A. Pearson, C. Knoechel, D. Hambach, E. A. Stach, E. Zschech, “Electromigration in Passivated Cu Interconnects Studied by Transmission X-ray Microscopy”, *J. Vac. Sci. Technol. B20*, 3089-3094 (2002), doi: 10.1116/1.1523403
- [Sch+12] G. Schneider, P. Guttmann, S. Rehbein, S. Werner, R. Follath,” Cryo X-ray microscope with flat sample geometry for correlative fluorescence and nanoscale tomographic imaging”, *J. Struct. Biol.* 177, pp. 212-223 (2012), doi: 10.1016/j.jsb.2011.12.23
- [Sha+04] D Shamiryany, T Abell, F Iacopi, K Maex, “Low-k dielectric materials”, *Materials Today* 7.1 (2004), pp. 34-39. doi: 10.1016/S1369-7021(04)00053-7
- [Sha+07] T. M. Shaw, E. Liniger, G. Bonilla, J. P. Doyle, B. Herbst, X. H. Liu, M. Lane, “Experimental Determination of the Toughness of Crack Stop Structures”, *IEEE* 2007, doi: 10.1109/IITC.2007.382368
- [Str+20] M. Strąg, Ł. Maj, M. Bieda, P. Petrzak, A. Jarzębska, J. Gluch, E. Topal, K. Kutukova, A. Clausner, W. Heyn, K. Berent, K. Nalepka, E. Zschech, A. G. Checa, K. Sztwiertnia, „Anisotropy of Mechanical Properties of Pinctada Margaritifera Mollusk Shell “, *Nanomaterials* 10(4) 634 (2020), doi: 10.3390/nano10040634
- [Tka+07] A. Tkachuk, F. Duewer, H. Cui, M. Feser, S. Wang, W. Yun, “X-ray computed tomography in Zernike phase contrast mode at 8 keV with 50-nm resolution using Cu rotating anode X-ray source”, *Zeitschrift für Kristallographie* 222 (11), (2007), doi: 10.1524/zkri.2007.222.11.650

- [Top+20] E. Topal, M. Löffler, E. Zschech, “Deep Learning-based Inaccuracy Compensation in Reconstruction of High Resolution XCT Data”, *Sci. Rep* 10, 7682 (2020), doi: 10.1038/s41598-020-64733-7
- [Tra2021] T. Trader, in *HPC wire*, “IBM Research Debuts 2nm Test Chip with 50 Billion Transistors”, <https://www.hpcwire.com/2021/05/06/ibm-research-debuts-2nm-test-chip-with-50-billion-transistors/>, visited on 08.01.2022.
- [Vol+10] W. Volksen, R. D. Miller, G. Dubois, “Low Dielectric Constant Materials”, *Chem. Rev.* 110, pp. 56–110, (2010), doi:10.1021/cr9002819
- [WH99] Y. Wei, J.W. Hutchinson, “Models of Interface Separation Accompanied by Plastic Dissipation at Multiple Scales”, *International Journal of Fracture* 95, 1–17 (1999), doi: 10.1023/A:1018627712739
- [WHG05] G. Wang, P. S. Ho, S. Groothuis, “Chip-packaging interaction: a critical concern for Cu/low k packaging”, *Microelectron. Reliab.* 45, pp. 1079 - 1093, (2005), doi: 10.1016/j.microrel.2004.12.008
- [Xu+02] G. Xu, Eb. Andideh, J. Bielefeld, T. Scherban, “Cohesive strength characterization of brittle low-k films”, *Proceedings of the IEEE*, (2002), doi: 10.1109/IITC.2002.1014886
- [Yoo+06] S. Yoon, D. Witarsa, S. Lim, V. Ganesh, A.G.K. Viswanath, T. Chai, K. O. Navas, V. Kripesh, “Reliability studies of a TSV stacked module for 3D microsystem packaging”, (2006) doi:10.1109/ECTC.2006.1645847
- [Zha+09] X. Zhang, R. S. Smith, R. Huang and P. S. Ho “Chip-Package Interaction and Crackstop Study for Cu/Ultra low-k Interconnects”, *AIP Conf. Proc.* 1143, pp. 197 – 203, (2009), doi: 10.1063/1.3169259
- [Zsc+18] E. Zschech, M. Löffler, P. Krüger, J. Gluch, K. Kutukova, I. Zgłobicka, J. Silomon, R. Rosenkranz, Y. Standke, E. Topal, “Laboratory Computed X-Ray Tomography – A Nondestructive Technique for 3D Microstructure Analysis of Materials”, *Pract. Metall.* 55, (2018), doi: 10.3139/147.110537
- [Zul+17] S. M. Zulkifli, B. Zee, W. Qiu, A. Gu, "High-res 3D X-ray microscopy for non-destructive failure analysis of chip-to-chip micro-bump interconnects in stacked die packages," 2017 IEEE 24th IPFA, pp. 1-5, (2017), doi: 10.1109/IPFA.2017.8060111

Appendix

A. Data analysis and calibration procedures

A1 Image analysis to determine parameter A

The parameter A is introduced to describe the boundary conditions of the beams (first derivative of the bending line) at the displaced cantilever ends, affecting the bending moment of the beam that presented in 3.2.2. Solving the differential equation (Eq. 3.1) for the two extreme cases “free beam end” and “fixed beam end” results in $A = 1$ for a free beam end and in $A = 0.5$ for a fully constrained beam with a zero slope at the beam end. The values for the parameters A_1 and A_2 (for the two cantilevers) were determined from radiographs of the real bending line, applying a least-square fitting procedure based on the micro-DCB adapted Euler-Bernoulli beam model (Eq. 3.18).

Stitching radiographs is performed semi-automatically based on Fiji [Ras13] software with a plug-in Grid / Collection stitching module. The overlap used is 16 to 17% estimated from the field of view (approx. $66 \mu\text{m}$) and the step size of the X-ray images taken ($55 \mu\text{m}$). The archived radiographs at each loading state (Figure A1 a) are binned (squeezed) with ratio of $XY = 4:1$, shown in in Figure A1 b.

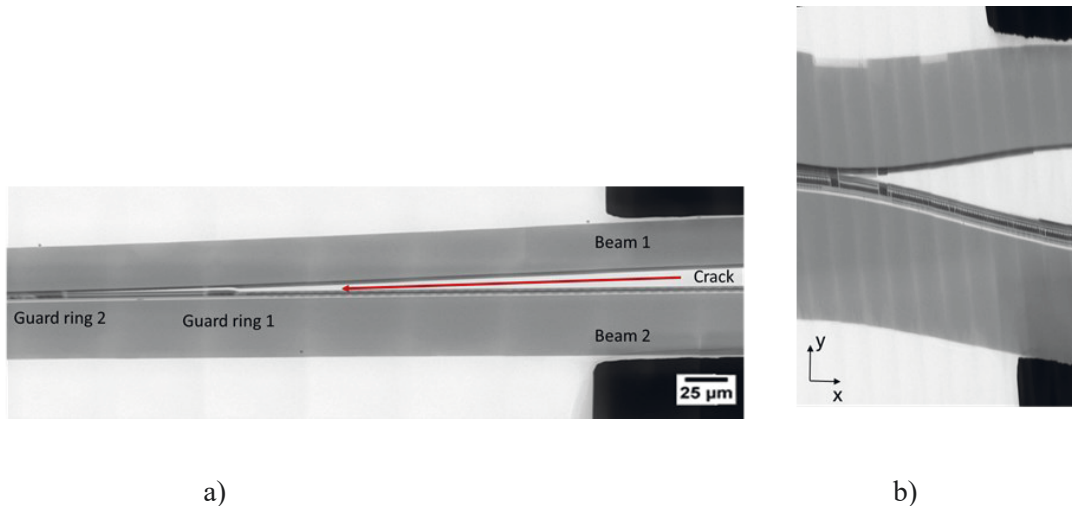


Figure A1: (a) Stitched radiograph of the micro-DCB test. The crack propagates towards the guard ring 2 (GR2), (b) binned radiograph.

The x - y coordinates of the measured data points that characterize the bending line geometry were extracted from radiographs at each loading step. Firstly, the x - y coordinates for several crack tip positions (loading steps) along each cantilever were determined

(“measured data points” in Figure A2). The bending line from the Euler-Bernoulli theory is a cubic function. However, this is only valid under the assumption that the fixed beam end at the support side ($x = 0$) is horizontally oriented. Therefore, the measured bending lines were rotated around the coordinate origin (at the crack tip, $x = y = 0$) to meet this condition. The rotation was done by adapting the linear coefficient of the polynomial fit of 3rd degree that equals the inverse tangent (arctan) of the angle between the beam and the x-axis at the origin. For the well aligned micro-DCB experiments in this study, the rotation angle needed is only a few degrees. With this rotation, the first derivative at the crack tip of the “rotated measured data” in Figure A2 is zero. Subsequently, a polynomial fit of 3rd degree (cubic fit) was performed for the bending geometry of each beam. Finally, the Euler-Bernoulli fit is applied according to Eq. 3.18. Since there is an inflection point in the bending line, two parameters can be determined by the cubic fit, i.e. the applied force F and the parameter A . That means, for the steady state (no crack propagation), it is possible to fully parameterize the Euler-Bernoulli model and to determine the potential (elastic) energy for the different loading steps of each cantilever. These A and F values are used for the calculation of the energy release rate for crack propagation for the respective loading conditions (Eq. 3.27). The data manipulation procedures were written to be used in Microsoft Excel. For the rotated curve, the Euler-Bernoulli fit can be applied. The Young’s modulus of the silicon was considered as isotropic, with the value of 130 GPa.

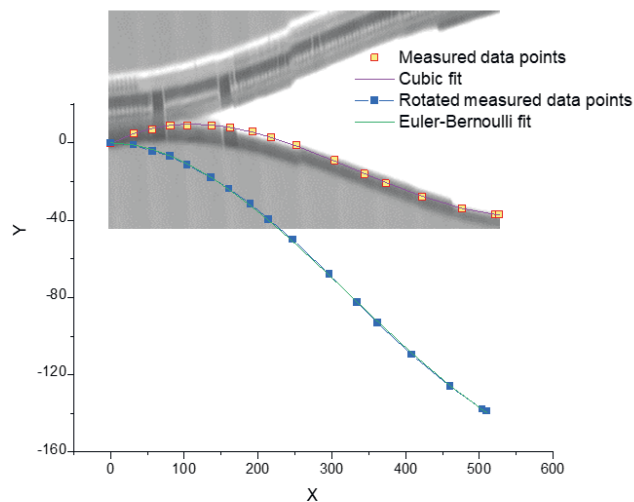


Figure A2: Illustration of the data analysis: measured data points from compressed ($x:y = 4:1$) stitched radiograph (shifted to the origin $x = 0$, $y = 0$), polynomial fit of 3rd degree (cubic fit), measured data points rotated by a small angle, and Euler-Bernoulli beam model, fitting according to Eq. 3.18.

A2 Micro-DCB 2.0 calibration

Force sensor calibration

A load cell is a force-sensing module - a carefully designed metal structure with small elements called strain gauges, mounted at precisely defined locations to the structure. The load cell is designed to measure the applied force in one direction. The electrical signal output by the load cell is measured and amplified through the board- PhidgetBridge 4- Input (Phidgets Inc., Canada). The application of the load cell requires a calibration that is performed using data of known weights or forces and applying a subsequent linear interpolation. This standard calibration procedure is done as described in [Phi18].

To understand and compensate temperature effects, the thermal drift of the three identical load cells during long-time static measurements under controlled conditions was measured. Using climate test cabinets from Mytron Bio- und Solartechnik GmbH (Gaussring, Germany), three temperature cycles in the range between 20 °C and 30 °C were applied (cooling/holding, heating/holding). The output data during cycling for the 3 load cells with corresponding force values are shown in Figure A3. From the graph we see that temperature changes have a high impact to the load measurement. The load sensors are reacting differently at 27 °C and higher. Sensor number 3 with less temperature impact on the force measurement was installed to the micro-DCB 2.0 tester.

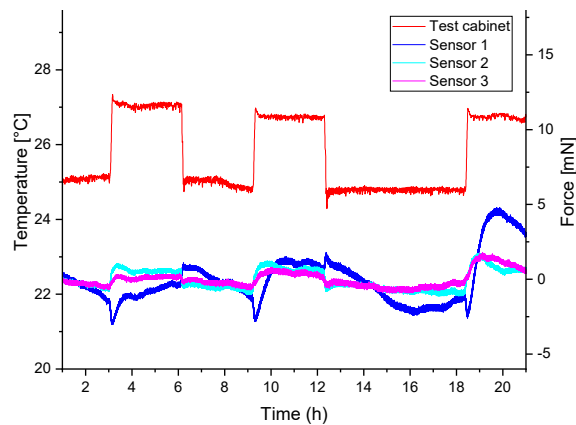


Figure A3. Temperature and force output plot at long term cycling for three identical load cells.

To understand thermal drift of the load cell of the micro-DCB 2.0 set-up inside the X-ray microscopes safety box, additional investigations were performed. The micro-DCB 2.0 tester was placed on the rotary table of the TXM. Three thermocouples (Type K) were placed on the following positions: (1) bottom and (2) top of stage (inside TXM) of micro-DCB 2.0

tester, and (3) outside TXM, as shown in Figure A4. An 8-channel thermocouple data logger (Omega Engineering, Connecticut, USA) was used for recording of the temperature values over 16 hours (typical acquisition time for a tomography).

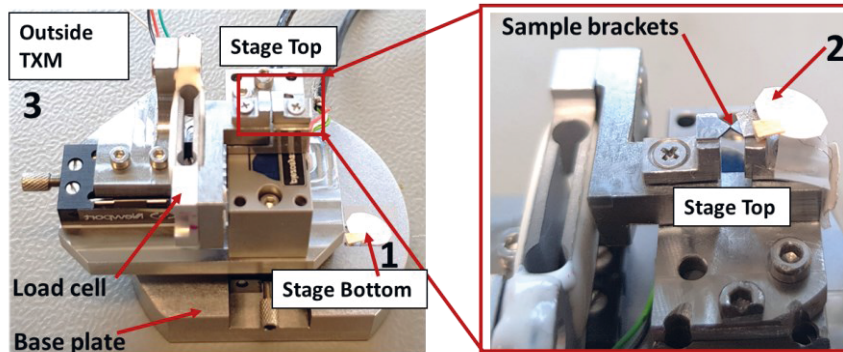


Figure A4. Experimental setup of the micro-DCB 2.0 tester with 3 temperature measurement points: (1) Bottom of stage and (2) top, at brackets position (inside TXM safety box), and (3) temperature outside TXM (room).

Based on the data, shown in Figure A5. the temperature difference between the top and bottom of the micro-DCB 2.0 tester, as well as the thermal drift were identified. The results show that it is important to take into account the temperature stabilization time between the top and bottom of the stage of at least 1 h (red dash-line in the right magnified graph).

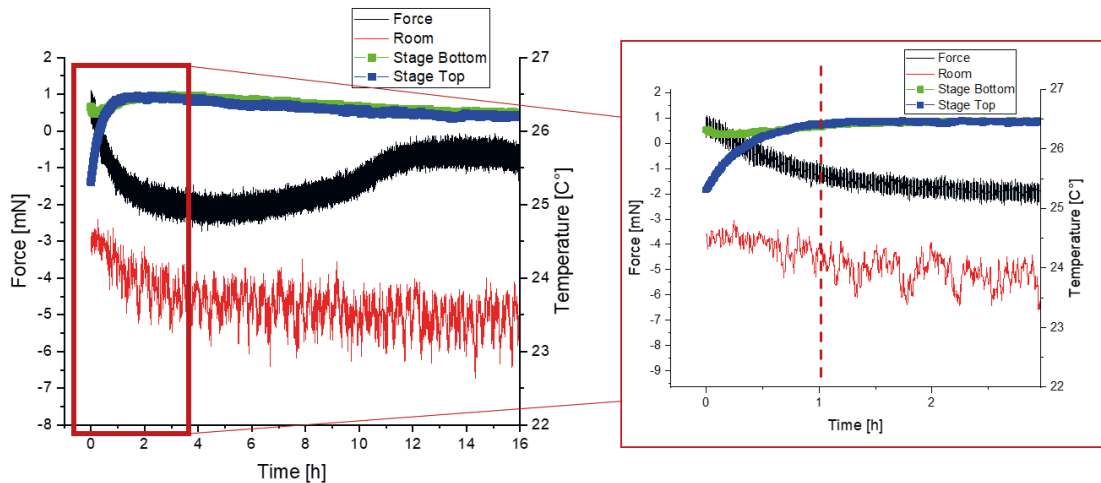


Figure A5. Output temperature and force measurement for sensor #3, that was installed into the micro-DCB 2.0 tester: left whole graph, right is a zoomed region. The mean force value over 16 h is $F = -1.21 \text{ mN} \pm 0.724 \text{ mN}$ (standard deviation).

Displacement calibration

The second part of the system calibration is the displacement calibration, that were done using stiffness or compliance of the system from the measured force–displacement curves. It is important to calibrate the raw output value of the piezo (closed loop) to a real displacement (crack opening), that is measured directly form radiographs. Two cases of force–displacement curves were recorded with following set-ups:

- (1) System “No sample”- empty sample holders (brackets). The force was applied to the sample holders (brackets) that were fixed to each other with super glue [Gorilla Glue, Inc., Cincinnati, OH, USA]. Force was applied until the detachment (fail) of one of the brackets – see Figure A6 (a, b);
- (2) System “With sample”. Sandwich-like sample (2 bonded Si wafer pieces) with cross-section of about $50 \times 50 \mu\text{m}$ was mounted between two brackets in same way as the micro-DCB sample, however without notching the sample. The force was applied to the system until the sample was detached from one of the brackets - see Figure A6 (c, d).

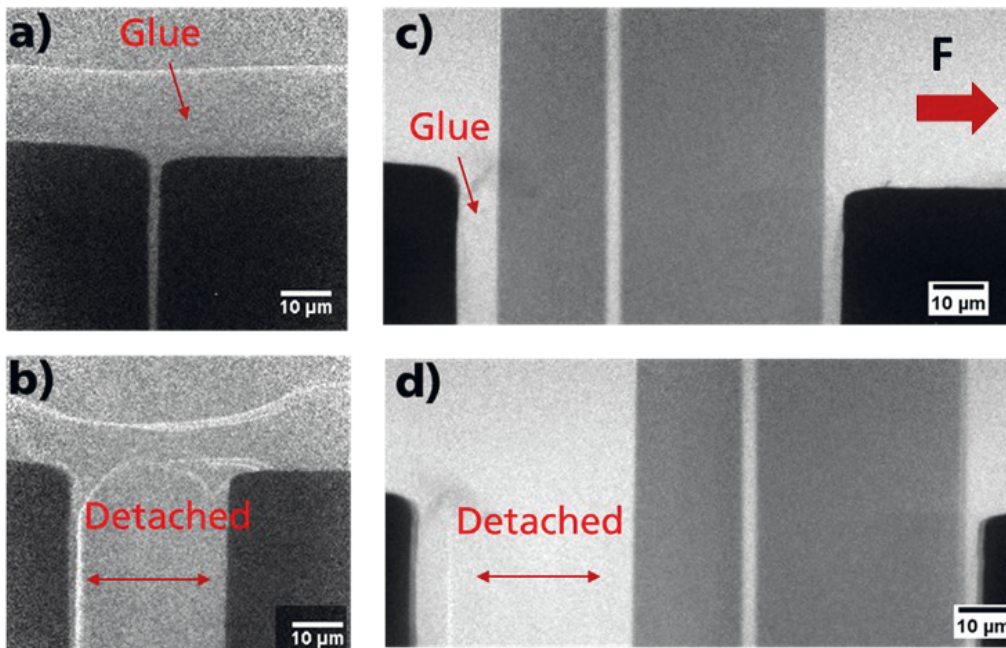


Figure A6. Radiographs (20s exposure time, camera binning 2): “No sample” - only glue between brackets a) before loading and b) after test; “With sample” - sample glued to brackets without notching; c) before and d) after test.

The force-displacement curves of the tested systems are shown in Figure A7. Here the system stiffness is derived from the linear part of the force-displacement curve. It resulted in a slope of 17.25 mN/ μm (linear fit) for the system with “No sample”. For the system with *Si* bar sample (no crack growth), the slope equals to 17.5 mN/ μm . To approximate real experimental conditions, the value of 17.5 mN/ μm achieved in a system including a *Si* bar will be used for the displacement correction in the micro-DCB 2.0 experiments.

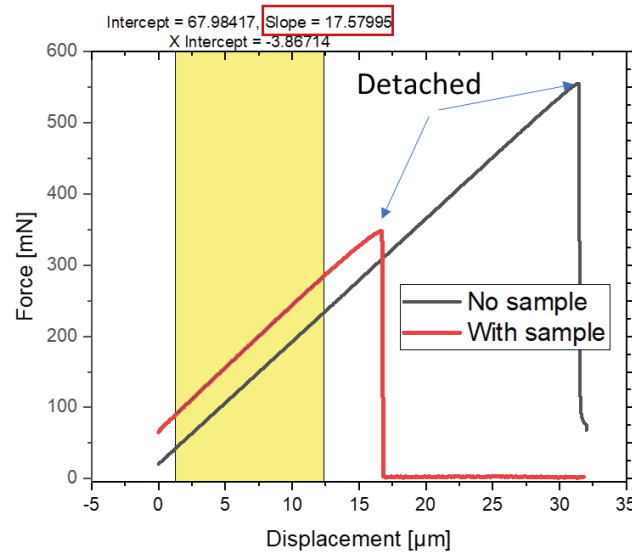


Figure A7. Load-displacement curve for the systems shown in Figure A6. The linear slope fitting (yellow area) indicates the system stiffness with sample.

A3 Error estimation of analytical approaches for G_c

Deviations of equation parameters

To reveal the influence of the equations parameters on the final result for G , the impact of $\pm 10\%$ deviation of the input parameters was investigated based on experimental measurements of micro-DCB and DCB 2.0 on control samples.

For the micro-DCB test system results show that from the all presented parameters in Eq. 3.27, the crack length L , extreme values of geometric parameter A and beam ratio e have a greater influence and indicate the importance of the accuracy of these parameters (Figure A8).

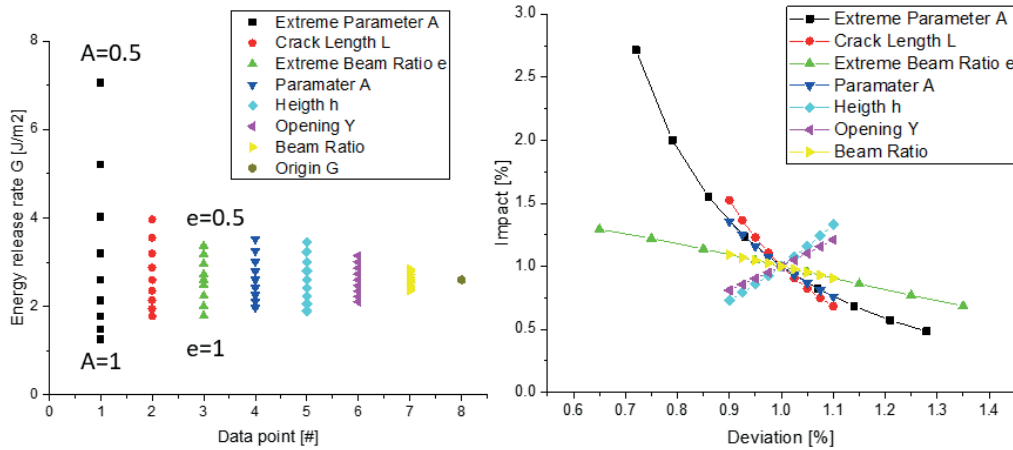


Figure A8: Calculation of G (Eq 3.27) and its deviation due to parameter variation as measured, crack length L , opening Y (sum of deflections), beam width b , beam thickness h , beam ratio e as well as extreme values of ratio $0.5 \leq e \leq 1$.

The parameter deviations of $\pm 10\%$ of F , $u_{y_1}(L)$, L and b on G translate into $\pm 10\%$ changes in G , which is understandable as they are linearly combined in Equation (3.29), compare to micro-DCB as shown in Figure A9. The crack length impact in comparison to Figure A8 is in the range of 8 % to 4.5 %. In both cases, the high impact of the variation of the beam ratio e to its extremes (0.5 ... 1) indicates the possibility of using this parameter for the adjustment of the fracture mode mixity.

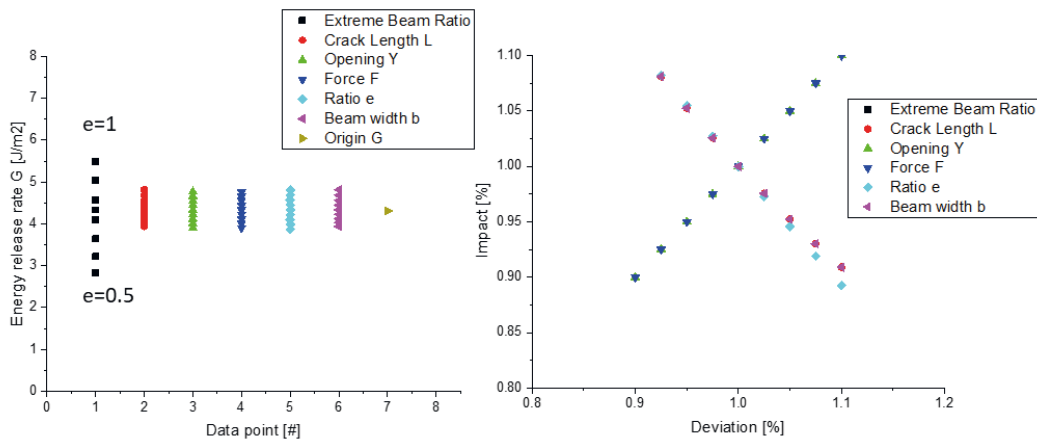


Figure A9: Calculation of G (Eq. 3.29) for one simple-beam system only ($n=1$) and its deviation due to a 10% input parameter variation in the measured force F , crack length L , displacement $u_{y_1}(L)$, beam width b , beam ratio e as well as extreme values of beam ratio for one beam corresponds to $0.5 \leq e \leq 1$.

Crack length measurements

In both cases, the crack length L is of high importance. The methodology for determining the crack length for micro-DCB and micro-DCB 2.0 is based on a semi-automatic approach that involves the image (resolution) and the human eye (assumption based on the contrast). In the micro-DCB test, compare to standard DCB test, it is hard to defined location of applied force due to the rigid joints and sample mounting. Based on the Euler-Bernoulli fitting approach (3.2.2) and the boundary conditions in Figure 3.5, the location of the force is assumed to be $\frac{1}{4}$ of the bracket length (zero slope). Therefore, the place where is sample attached at $\frac{1}{4}$ of bracket length is taken as a starting point of crack growth (Figure A10a). At a certain loading state, the crack tip is determined by human eye from radiographs (Figure A10b) based on a sufficient contrast between ILD layers, silicon, adhesive and air (crack). The final crack length is defined in micrometers as the distance between two points: $\frac{1}{4}$ of the brackets length and assumed crack tip. Based on the human observation, a categorization was performed. In Figure A10 b, the radiograph with a FOV (SR) of approx. $65 \mu\text{m}$ was categorized as “clearly a crack”, “possibly a crack”, and “clearly no crack” (each red box is about $21 \mu\text{m}$). These $21 \mu\text{m}$ are taken as an extreme value of measurement error that can be localized in radiograph by the human eye.

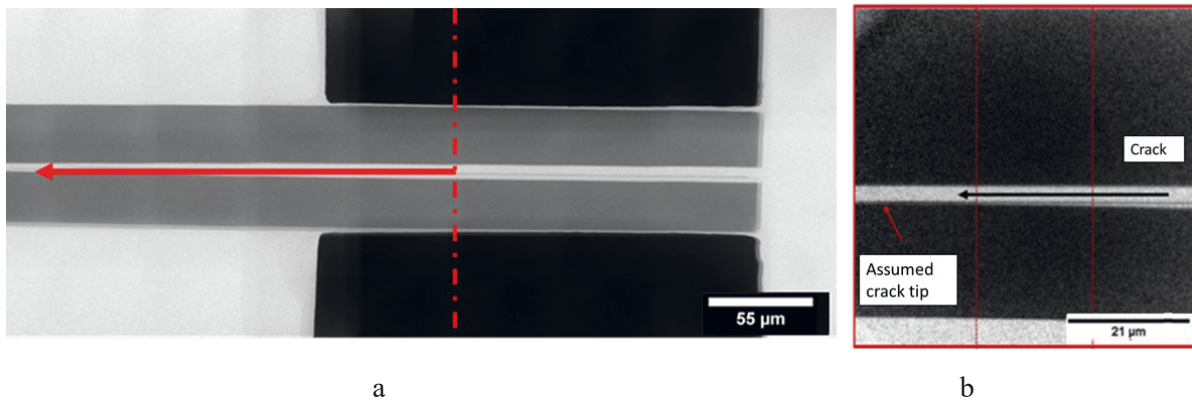


Figure A10: Radiograph showing the direction of the crack path from left to right (black) (a) and the proposed crack tip (red), determined by the human eye (b). Crack propagation from the right to the left.

Ideally, the G -value should be constant as the crack grows “Ideal”, as shown in Figure A11b for micro-DCB (Eq. 3.27) and Figure A11b for micro-DCB 2.0 (Eq.3.29). If we take “Ideal” curve as a reference, we can calculate G according to a maximum error of $\frac{1}{3}$ of the FOV as stated above. The resulting G value over the crack length is shown on the same

graphs. In case of micro-DCB test in Figure A11 a, “L1” (ideal -21 μm) yields to a deviation of G values from 14.5% to 55.8% and “L2” (ideal +21 μm) yields to a deviation from 12.33% to 33%. Depending on the specimen geometry and specimen design (e.g guard ring location), the measured crack lengths are in the range of 300 μm to 450 μm , which results in an error in the range of 15% to 26%.

The resulting G value for micro-DCB 2.0 in Figure A11 b, for “L1” (ideal -21 μm) yields to a deviation from 21% to 3.8% and “L2” (ideal +21 μm) yields to a deviation from 14.7% to 3.5%. Based on the specimen geometry and specimen design (e.g guard ring location), the measured crack lengths are in the range of 300 μm to 450 μm , which results in an error in the range of 8 % to 4.5 %. However, in reality this error is assumed to be much lower, as the accuracy of determining the crack tip by human eye is mostly more accurate than 1/3 image width.

These results show that parameters such as crack length L , extreme values of geometric parameter A and beam ratio e have a larger influence than other parameters (beam width b , force F , displacement $u_{\overline{y}_1}(L)$) and indicate the importance of the accuracy of these parameters.

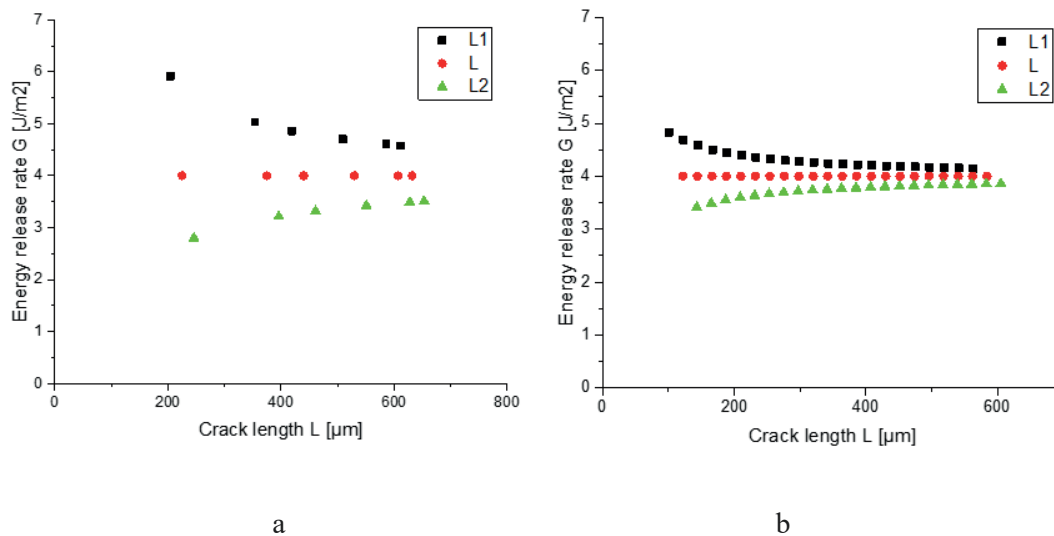
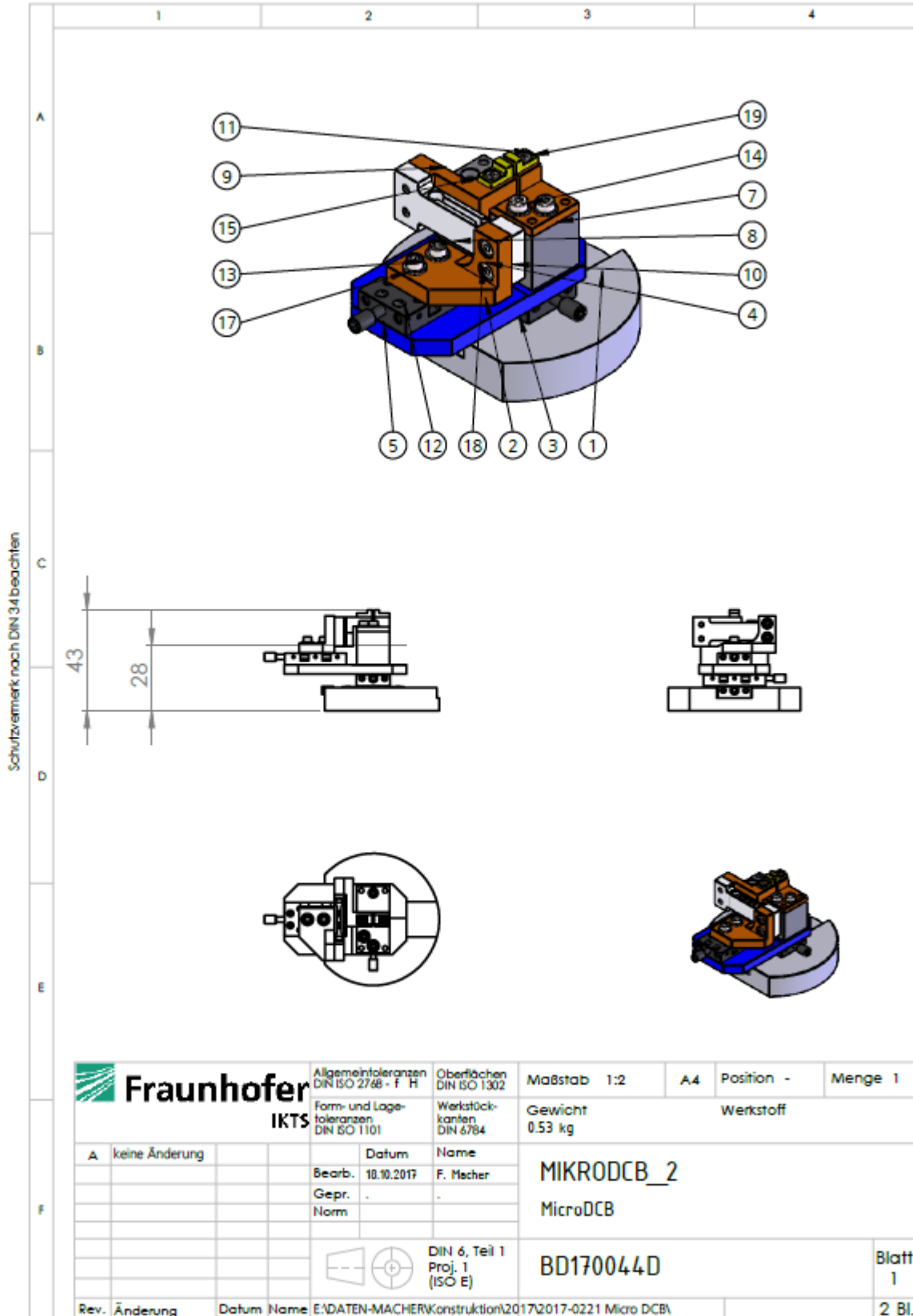


Figure A11: (a) Calculated G (equation 3.27) along the crack length L , where the constant G value is taken from the reference data of unpatented structures ($G = 4 \text{ J/m}^2$), beam ratio $e = 1$ ($h1=h2$), sample width $b = 50 \mu\text{m}$: b) Calculated G (Eq.3.29) along the crack length L , where the constant G value is taken from the reference data of unpatterned structures ($G = 4 \text{ J/m}^2$), beam ratio $e = 1$ ($h1 = h2$), sample width $b = 50 \mu\text{m}$.

B. Tester drawings and interface

B1 Drawings micro-DCB 2.0



B2 Graphical user interface of micro-DCB 2.0

For the data measurements, synchronization and recoding, a Graphical User Interface (GUI) based on the Laboratory Virtual Instrument Engineering Workbench (LabVIEW) software has been designed and created (visual programming language from National Instruments), developed at Fraunhofer IKTS.

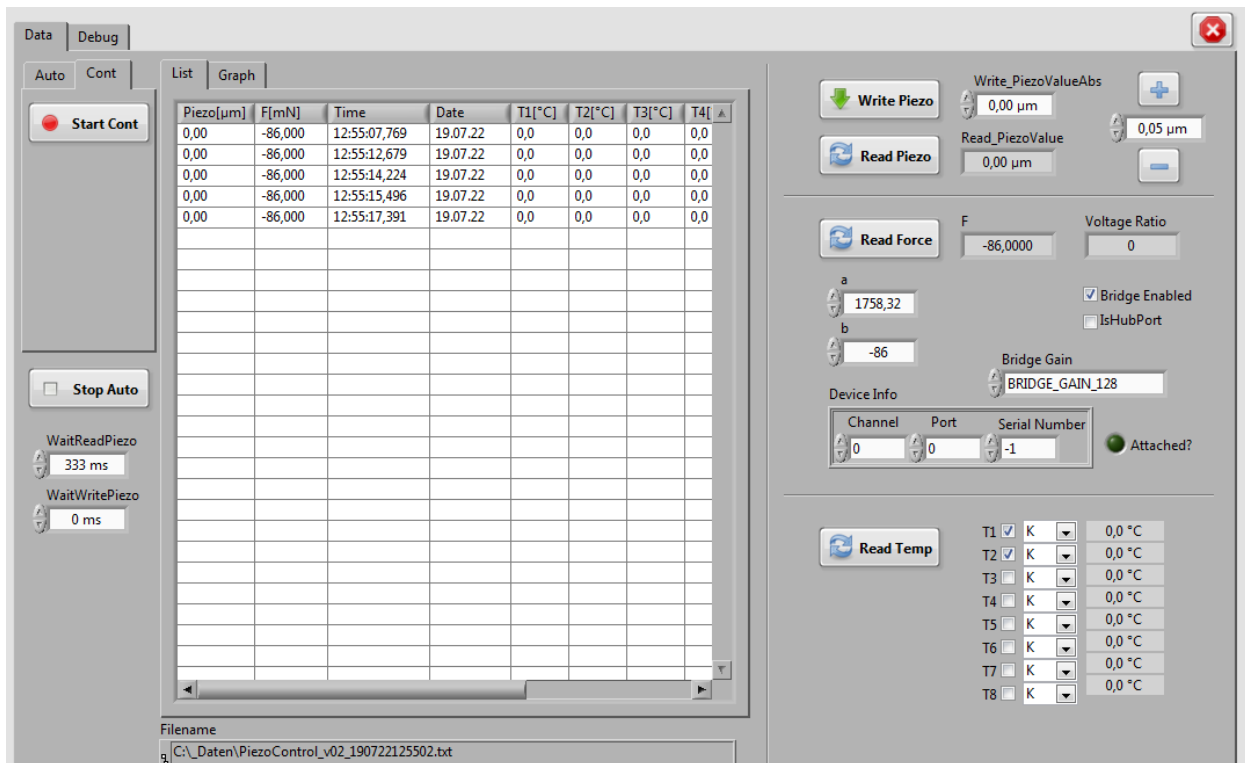


Figure B1: Main frame of the graphical user interface (GUI)

The framework allows to set test parameters for manual or semi-automated operation modes. For example, *Continuous mode* allows to operate with piezo displacement by sending the desired step size manually at random time intervals with simultaneous data recording to the text file. In *Automated mode* all parameters are fixed: step size, time interval and maximum displacement. The amount of records in the data file corresponds to the amount of steps. The automated mode helps to drive a crack much faster to the region of interest (ROI) with less operator efforts. Continuous mode is used to examine the guard ring with finer steps under required imaging settings (exposure time at ROI).

The calibration data and linear offset for the load cell can be directly applied to the right side of the framework. The calibration procedure is given by the manufacturer of the electrical signal amplifier - PhidgetBridge 4-Input (Phidgets Inc, Canada) and suitable for our system as well.

For better visualization of the process during the Micro-DCB experiment, the output data of force, displacement and temperature over time are shown as a graph in Figure B2.

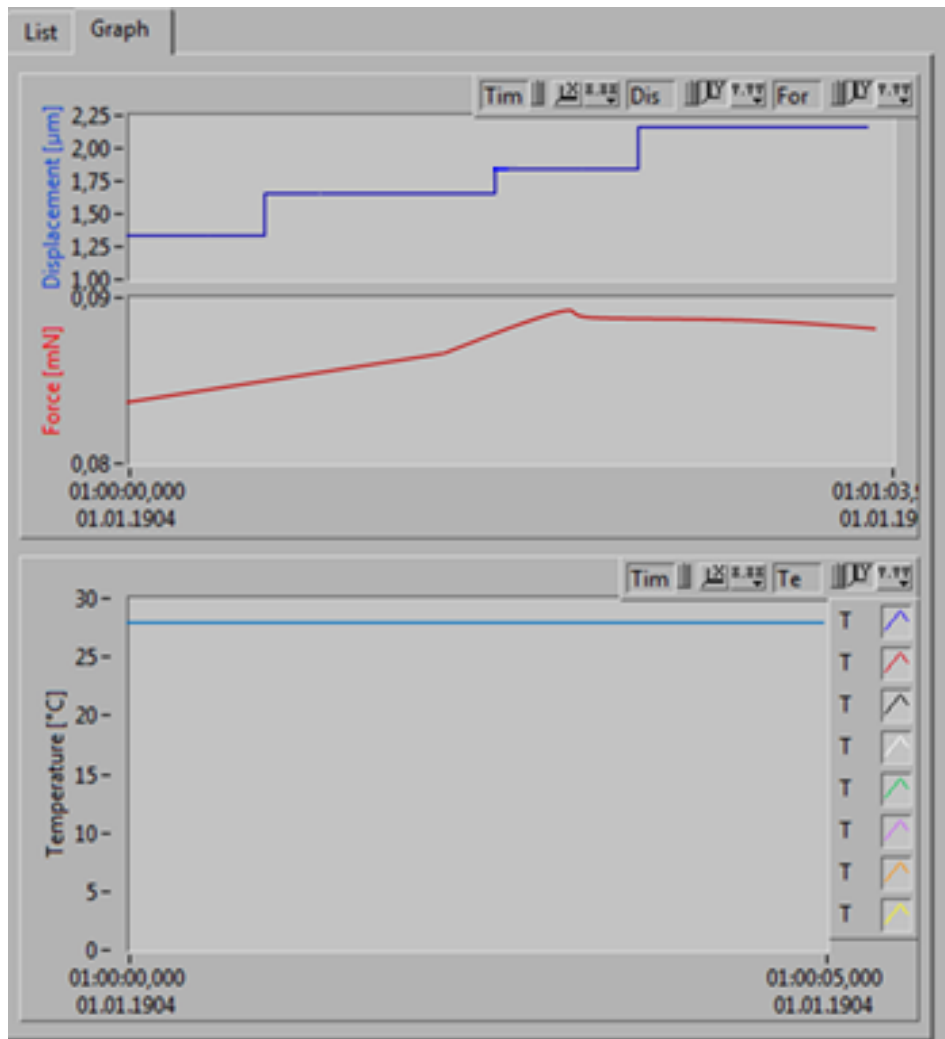


Figure B2: Second frame of the graphical user interface visualizing the logged data.

C Source code

The subsequent plugin can be run in ImageJ. It analyzes a virtual stack of the BEOl data set (in particular GR) to map a height of the crack above silicon substrate (J. Gluch, Fraunhofer IKTS, 2016).

```

run("Select None");
run("Duplicate...", "duplicate");
rawdata=getImageID();
getVoxelSize(width, height, depth, unit);
getLocationAndSize(lx, ly, lw, lh);

print(height);

newImage("CrackDepth5", "32-bit black", getWidth(), nSlices(), 1);
run("16 colors");
setVoxelSize(width, depth, depth, unit);
setLocation(lx, ly+lh+10);
resultimg=getImageID();

selectImage(rawdata);
run("Remove Overlay");
setLineWidth(1);

setTool("rectangle");
waitForUser("select box that includes the crack,\n bottom=surface of wafer");
//makeRectangle(1, 98, 490, 46);
getBoundingRect(sx, sy, sw, sh);

for (ty=1; ty<=nSlices(); ty++) {
    setSlice(ty);
    setBatchMode(true);
    for (tx=2; tx<=getWidth()-2; tx++) {
        selectImage(rawdata);
        makeLine(tx, sy+sh, tx, sy);
        profile = getProfile();
        Array.getStatistics(profile, min);
        depth = indexOfArray(profile, min);

        makeOval(tx, sy+sh-depth[0], 1, 1);
        run("Add Selection...");
        Overlay.setPosition(ty);

        Overlay.show;
        //print(tx, depth[0], min);

        selectImage(resultimg);
        setPixel(tx, ty, depth[0]);
    }
}

```

```

        selectImage(rawdata);
    }
    setBatchMode(false);
    selectImage(resultimg);
    resetMinAndMax();
    selectImage(rawdata);
}
selectImage(resultimg);
run("Multiply...", "value="+height);
run("Despeckle");
setMinAndMax(0, 6);
run("Canvas Size...", "width="+getWidth()+80+" height="+getHeight()+"
position=Center-Left");
makeRectangle(getWidth()-80, 0, getWidth(), getHeight());
run("Set...", "value=6");
run("Scale Bar...", "width=5 height=3 font=16 color=Black background=None
location=[Lower Right]");
run("Calibration Bar...", "location=[Upper Right] fill=White label=Black number=5
decimal=0 font=14 zoom=2 overlay");
print("Ende");

function indexOfArray(array, value) {
    count=0;
    for (i=0; i<lengthOf(array); i++) {
        if (array[i]==value) {
            count++;
        }
    }
    if (count>0) {
        indices=newArray(count);
        count=0;
        for (i=0; i<lengthOf(array); i++) {
            if (array[i]==value) {
                indices[count]=i;
                count++;
            }
        }
    }
    return indices;
}

```

List of publications

Papers in peer-reviewed journals– First author

- K. Kutukova, P. Guttman, Z. Liao, S. Werner, Y. Standke, J. Gluch, G. Schneider, E. Zschech
„In-situ X-ray Microscopy of Crack-Propagation to Study Fracture Mechanics of On-Chip Interconnect Structures“
MRS Adv. 3(39), 2305 – 2310 (2018)
DOI: 10.1557/adv.2018.410
- K. Kutukova, S. Niese, J. Gelb, R. Dauskardt, E. Zschech
„A Novel Micro-Double Cantilever Beam (micro-DCB) Test in an X-ray Microscope to Study Crack Propagation in Materials and Structures “
Mater. Today Commun. 16, 293–299 (2018)
DOI: 10.1016/j.mtcomm.2018.07.006
- K. Kutukova, S. Niese, C. Sander, Y. Standke, J. Gluch, M. Gall, E. Zschech
„A Laboratory X-ray Microscopy Study of Cracks in on-chip Interconnect Stacks of Integrated Circuits “
Appl. Phys. Lett. 113, 091901 (2018)
DOI: 10.1063/1.5031204
- K. Kutukova, Z. Liao, S. Werner, P. Guttman, Y. Standke, J. Gluch, G. Schneider, E. Zschech
„Combination of Soft X-Ray Microscopy with In-Situ Mechanical Testing to Image Crack Propagation in Microchips “
Microscopy and Microanalysis 24(S2):438-439 (2018)
DOI: 10.1017/S1431927618014447
- K. Kutukova, J. Gluch, M. Kraatz, A. Clausner, E. Zschech
“In-situ X-ray tomographic imaging and controlled steering of microcracks in 3D nanopatterned structures”
Materials & Design 221 (2022) 110946
DOI: 10.1016/j.matdes.2022.110946

Papers in peer-reviewed journals –Co-author

- Zschech, M. Loeffler, P. Krueger, J. Gluch, K. Kutukova, I. Zglobicka, J. Silomon, R. Rosenkranz, Y. Standke, E. Topal,
„Laboratory Computed X-ray Tomography – A Nondestructive Technique for 3D Microstructure Analysis of Materials “
Pract. Metallogr. 55, 539–555 (2018)

- I. Zglobicka, A. Chmielewska, E. Topal, K. Kutukova, J. Gluch, P. Krüger, C. Kilroy, W. Swieszkowski, K. Kurzydłowski, E. Zschech
“3D Diatom–Designed and Selective Laser Melting (SLM) Manufactured Metallic Structures”
Sci Rep 9, 19777 (2019)
DOI: 10.1038/s41598-019-56434-7
- M. Strąg, Ł. Maj, M. Bieda, P. Petrzak, A. Jarzębska, J. Gluch, E. Topal, K. Kutukova, A. Clausner, W. Heyn, K. Berent, K. Nalepka, E. Zschech, A. G. Checa, K. Sztwiertnia,
„Anisotropy of Mechanical Properties of Pinctada Margaritifera Mollusk Shell “,
Nanomaterials 10(4) 634 (2020)
DOI: 10.3390/nano10040634
- K. Bulatov, M. Chukalina, K. Kutukova, V. Kohan, A. Ingacheva, A. Buzmakov, VV.Arlazarov, E. Zschech
“Monitored Tomographic Reconstruction—An Advanced Tool to Study the 3D Morphology of Nanomaterials”
Nanomaterials. 2021; 11(10):2524
DOI: 10.3390/nano11102524
- J. Milewski, K. Kutukova, J. Gluch, K. Futyma, E. Zschech
“Investigation of the filling of a porous ceramic matrix by molten salts using nano X-ray tomography”
Energy Reports, Vol. 8, pp. 1440-1449 (2022)
doi.org/10.1016/j.egyr.2022.07.102.
- Q. Yue, K. Kutukova, A. Li, J. Čejka, E. Zschech, M. Opanasenko
“Controllable Zeolite AST Crystallization: Between Classical and Reversed Crystal Growth”
Chemistry - A European Journal 28(35) (2022)
DOI: 10.1002/chem.202201467
- E. Zschech, E. Topal, K. Kutukova, J. Gluch, M. Löffler, S. Werner, P. Guttmann, G. Schneider, Z. Liao, J. Timoshenko,
„Multi-scale microscopy study of 3D morphology and structure of MoNi₄/MoO₂@Ni electrocatalytic systems for fast water dissociation “
Micron, Vol. 158, 103262 (2022)
DOI: 10.1016/j.micron.2022.103262.
- V. Shapovalov, K. Kutukova, S. Maletti, C. Heubner, V. Butova, I. Shukaev, A. Guda, A. Soldatov, E. Zschech
“Laboratory X-ray Microscopy Study of Microcrack Evolution in a Novel Sodium Iron Titanate-Based Cathode Material for Li-Ion Batteries”
Crystals. 2022; 12(1):3
DOI: 10.3390/cryst12010003

Invited talks at conferences

- K. Kutukova, Z. Liao, S. Werner, P. Guttman, Y. Standke, J. Gluch, G. Schneider, E. Zschech
„In-situ X-ray Microscopy of Crack-Propagation to Study Fracture Mechanics of On-Chip Interconnect Structures “
MRS Spring Meeting, Phoenix/AZ 2018
- K. Kutukova, J. Gluch, I. Zgłobicka, C. Sander, A. Clausner, E. Zschech
„In-situ Nano X-ray Tomography for High-Resolution Imaging of Cracks in Composites and Integrated Circuits during Mechanical Loading “
MRS Spring Meeting, Phoenix/AZ 2019
- K. Kutukova, J. Gluch, C. Sander, A. Clausner, E. Zschech,
“In-situ micro-DCB study of crack propagation in Cu/Low-k BEoL structures”
TECHCON 2019, Austin/Texas, September 2019
- K. Kutukova, J. Gluch, A. Clausner, E. Zschech
“Mechanical Set-Ups in Laboratory X-Ray Microscopy to Study In Situ Crack Propagation at Patterned Structures”
MRS Spring, Virtual, April 2021
- K. Kutukova, J. Gluch, A. Clausner, E. Zschech
“In-situ laboratory X-ray microscopy to image crack propagation with high resolution”
EUROMAT 2021, Virtual, September 2022
- K. Kutukova, J. Gluch, M. Kraatz, A. Clausner, E. Zschech
“In-situ nano- XCT study of the mechanical robustness of BEoL stacks”
MAM2022, Leuven/Belgium, March 2022
- K. Kutukova, J. Gluch, M. Kraatz, A. Clausner, E. Zschech
“In-situ Micro-DCB / Nano-XCT Test to Ensure the Robustness of Leading-edge Cu/ULK BEoL Stacks”
FCMN 2022, Monterey/CA, June 2022
- K. Kutukova, V. Schapovalov,, E. Zschech
“Operando laboratory X-ray absorption spectroscopy and X-ray computed tomography studies of novel cathode materials for batteries”
NANO 2022, Sevilla, Spain, June 2022
- K. Kutukova, V. Schapovalov,, E. Zschech
“Customized nano-XCT solutions for operando studies of electrochemical processes”
Nanomat2022, Bratislava, Slovakia, September 2022

Poster Presentations:

- K. Kutukova, H. Li, J. Gluch, Z Ma, R. Rosenkranz, Y. Standke1, C. Sander, S. Niese, E. Zschech, “Crack path localization in Cu/low-k stacks during micro DCB tests using nano - XCT“, IRSP Conf., Bad Schandau/Germany, (2016) (*1st place poster award*)
- K. Kutukova, J. Gluch, Y. Standke, E. Zschech, “Crack evolution in Cu/Low-k stacks and crack stop evaluation using in-situ micro-DCB in a nano-XCT tool”, International FCMN conference, March 2017, Monterey/CA (2017)
- K. Kutukova, Z. Liao, S. Werner, P. Guttman, Y. Standke, J. Gluch, G. Schneider, E. Zschech, “Combination of soft X-ray microscopy with in-situ mechanical testing to image crack propagation in microchips”, 6th Dresden nano-analysis symposium, Dresden/Germany, (2018) (*2nd place poster award*)
- K. Kutukova, J. Gluch, E. Zschech, “In-situ X-ray microscopy imaging of cracks in Cu/OSG stacks in integrated circuits”, The XXII Physical Metallurgy and Material Science Conference (AMT 2019), Bukowina Tatrzańska/Poland, (2019) (*distinction poster award*)
- K. Kutukova, S. Werner, P. Guttman, G. Schneider, E. Zschech, „High-resolution Spectromicroscopy of silicon compounds in integrated circuits“, 18th International Conference on X-Ray Absorption Fine Structure Hybrid (XAFS 2022), Sidney/Australia, 2022

Acknowledgment

First of all, I would like to express my sincere gratitude to my supervisor Prof. Dr. Ehrenfried Zschech who made this thesis possible. His guidance and advice carried me through all the stages of this project. I appreciate all his great ideas and time. I could not have been imagined a better supervisor for my PhD thesis.

I would like to thank my colleagues at Fraunhofer IKTS Dresden, I had the pleasure to work with and who supported me in performing challenging experimental task and in data analysis, particularly Dr. Jürgen Gluch, Dr. Andre Clausner, Dr. Martin Gall, Yvonne Standke, Dr. Zhongquan Liao, Dr. Matthias Kraatz, Dipl.-Ing. Christoph Sander, Dr. Emre Topal, Dr. Peter Krüger and Dr. Sven Niese.

My gratitude goes to Dr. Markus Kuhn and Dr. Han Li at Intel, Hillsboro/OR, US, who provided deep insight into the mechanical robustness requirements of leading-edge microchips and for a very valuable regular scientific and technical exchange.

I would like to thank Prof. Dr. Gerd Schneider and Dr. Stephan Werner at Helmholtz Center Berlin, Germany, as well as Dr. Oden Warren and Dr. Douglas Stauffer at Bruker, Minneapolis/MN, USA, for supporting and enabling my exciting in-situ X-ray microscopy experiments at BESSY II Berlin.

My further gratitude goes to Prof. Dr. Dieter Schmeißer and Dr. Karsten Henkel at Brandenburg University of Technology Cottbus-Senftenberg for helping me to keep the contact to my alma mater and for scientific discussions, particularly during Winter and Summer Schools for Young Scientists.

Finally, I would like to thank my family, closest friends, and my beloved for their endless support and trust in me.